Eindhoven University of Technology

MASTER

Antenna pattern diversity for GSM handhelds

Mattheijssen, P.

Award date:
2000

Eindhoven University of Technology
Faculty of Electrical Engineering
Division of Telecommunications Technology and
Electromagenetics

Antenna pattern diversity for GSM handhelds

P. Mattheijssen
Graduation Thesis
(Confidential)

Performed at	: Philips Research Laboratory Eindhoven
Period	: September 1999 – June 2000
Graduation Professor	: Prof. dr. ir. G. Brussaard (TUE)
Supervisors	: Dr. ir. M. H. A. J. Herben (TUE)
	: Ir. L. Leyten (PRLE)

Abstract

Antenna diversity techniques are often used in present day to improve the overall performance of a radio system. Since the physical dimensions of the present day applications e.g. as handhelds become smaller and smaller these diversity techniques do not work properly. These diversity techniques works very well if the mutual coupling is negligible. In order to cope with small physical dimensions of the applications a new diversity concept is introduced. This is called antenna pattern diversity in which switched parasitic elements are used.

The objective of this report is to explore if antenna pattern diversity is possible and if it is possible to examine the performance of a prototype. MATrix LABoratory (MATLAB) and Numerical Eletromagnetics Code (NEC) provide the basis for the simulations. The performance of the prototype is measured. These measurements were performed at Philips Research Laboratory Eindhoven.

In order to apply antenna pattern diversity successfully the angles of arrival of the radiowaves play a prominent part. Two methods which are based on Fourier Transform and MUltiple SIgnal Identification and Classification (MUSIC) were explored. The latter was applied to measured data since it has the best spatial resolution at short aperture lengths. Measurements show that the angle of arrival is strongly correlated over the GSM frequency band.

A theoretical model based on two closely spaced dipoles is derived in order to make different far field radiation patterns. The same antenna configuration of the theoretical model was also implemented in a numerical simulation tool. Simulations show that antenna pattern diversity using switched parasitic elements works very well. Futhermore it was shown that a low correlation coefficient ramains almost fixed over the entire GSM frequency band. But on the other hand the return loss (RL) is very bad over the GSM frequency band. So a compromise was made between a low correlation and a acceptable return loss. Finally this concept was built and its performance was analyzed by means of measurements. These measurements show that a diversity gain of 6 dB at a coverage level of 99% and at a bit error rate of 10^{-3} *can be achieved.*

Contents

Appendices

Chapter 1

Introduction

1.1 General introduction

Within the memory of men still living, they communicate with one an other. First with simple sounds, later on with words and full sentences. This manner of communication is only used at short distance. To meet the demand for long distance communication smoke-signals were introduced. But the connectability is still insufficient. After electricity had been invented, long distances were no problem any more, e.g. the telegraph was used to send messages in morse code. Shortly after this period the telephone came up to communicate with voices. The telephone is still the most important means of communication in the present-day. In most houses one or more telephones are available. This kind of telephone network is called a fixed network and means that the place from which the subscriber can make his call is fixed. The mobility is restricted by the length of the wire connecting the mouthpiece of the telephone and the telephone itself. As technology progresses the telephone will become smaller and smaller. At the same time RF designs improves as well in order to make mobile communication possible. First the pagers were introduced which represent only a simplex radio traffic. This means that the subscriber can only send short messages. After the pagers had been introduced the mobile phone was invented. In the course of the early years these phones were very big and you had to carry a big sized batteries on your back.

Since the number of subscribers increase rapidly another system architecture was needed to cope with mass communication. For this purpose the multi cellular radio communication concept was introduced. The GSM[1] is a mobile telecommunication system which uses this concept. For this purpose the area is subdivided into hexagons which use a predetermined frequency set. The adjacent areas are also subdivided into hexagons and use other frequency sets. This will be repeated till the entire area is covered (see Figure 1.1). When using this concept the capacity in terms of the number of subscribers increases substantially. The frequency re-use factor depends on the distance r and the carrier-to-interference ratio C/I. Since the subscribers are not restricted to a fixed place the radio channel will become a function of place and time. So it might be possible that sometimes the signal strength is poor resulting in a signal drown by noise. In the worst case the call will be lost. These so called fadings are caused by destructive interference the opposite

---

[1] GSM:Groupe Spe'cial Mobile, recently GSM has changed its name to the Global System for Mobile communication for marketing reason

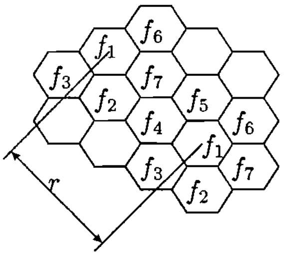

Figure 1.1: *Multi cellular radio communication concept.*

is called constructive interference. In order to improve the overall performance the base stations are equipped with multiple antennas to provide antenna diversity.
The optimalization at the base stations side can also be done at the handset side but this is not a matter of course since the physical dimension of the handset is much smaller than compared with the dimension of the base station. In this case we have to deal with the mutual coupling between these antennas. Moreover the internal space of the handset restricts us to put additional electronic circuits inside it. So other solutions have to be explored which make use of the mutual coupling.
This report explores the antenna pattern diversity using two closely spaced antennas where the mutual coupling is taken into account. All the simulations are performed in the GSM bandwidth. A study is done about the angle of arrival in order to investigate if the angle of arrival is correlated over the GSM frequency bandwidth. After these studies a prototype is built and its performance is analyzed.

1.2 Outline of report

This report is arranged as follows:

- Chapter 2 briefly describes the measurement set-up and a correction method for correcting the data for mismatches between the antennas and the cables. Furthermore the antenna pattern diversity principle is explained. First a correlation based on powers is performed which gives us information about frequency diversity and space diversity.
- Chapter 3 the Fourier transform is described and its features such as the effect of changing the signal-to-noise ratio and enlarging the aperture length on the spatial resolution.
- Chapter 4 describes the MUSIC algorithm which is an algorithm based on the eigenstructure of the covariance matrix. In order to cope with highly correlated sources a preprocessing scheme called spatial smoothing is introduced. Likewise the signal-to-noise and the aperture length in this case are also varied in order to explore the effects on the spatial resolution.
- Chapter 5 the MUSIC algorithm is applied to the measured data to extract the angle of arrival. A frequency sweep is done in order to explore if the angle of arrival remains constant over a bandwidth. In this case an angle of arrival correlation exercition is done to obtain this information. The same data are used to investigate the angle of arrival distribution.

- Chapter 6 describes a dual antenna system which is used to realize antenna pattern diversity and which consists of two vertically polarized half wavelength dipoles. The analytical results are compared with the numerical results in order to verify if the numerical results are accurate and steady. Next, a correlation formula is derived by judging two far field patterns and trying to find patterns which have a minimum overlap. A switching concept called antenna pattern diversity using switched parasitic elements is described as well.
- In chapter 7 the construction of the dual antenna is discussed and its performance is analyzed. Successively the performance is translated into a diversity gain obtained by measurements.
- In chapter 8 the results are summarized and recommendations are given.

Most figures used in chapter 5 and in chapter 6 are to be found in the appendices, including the derivation of the correlation function used in chapter 5

- Appendix A shows us the figures of the MUSIC spectra for the measurements in the x and y-direction.
- Appendix B the correlation formula is derived which is used in chapter 6.
- Appendix C shows us the figures of the correlation plots and their dependence on the reactance and resistance.
- Appendix D shows us photographs of the measurement set-up and the restaurant of the WAY building.
- Appendix E an overview of the symbols used in this report can be consulted.

1.3 Survey of literature

This survey of literature deals with antenna diversity. Much has been written about multiple antennas mounted on the base station. Currently the antennas of the handhelds or handsets have been improved for maximum performance. The goal of survey of literature is to make an overview of existing models and their characteristics.
The consulted literature sources are INSPEC (mainly), BAS and VUBIS. The first mentioned one is available at Philips Research laboratory Eindhoven (PRLE) and the second and third mentioned ones are available at Eindhoven university of technology (EUT). The research period lasted from 1969 to 2000. Terms that are interesting for this project are mutual coupling, space diversity, correlation (including statistics), prototypes and radiation patterns. The results of the survey of literature are summarized below.
Information about antennas used for diversity techniques are to be found in the following papers [27, 28, 29, 31, 35]. These papers are dealing with space diversity, including mutual coupling and correlation coefficients. Some prototypes have been investigated by means of measurements.

The following papers are dealing with the research of switched parasitic elements for antenna diversity [13, 14, 15, 30, 32, 33, 26], including a primitive prototype to evaluate patterns for antenna diversity. Commonly used antenna models are those who consist of two closely spaced vertically polarized dipoles where one dipole is fed and the other one is left open or shorted.

More general information about diversity techniques and its performance can be found in the following papers [21, 22, 23, 24, 25, 34]. These papers are mainly based on measurements for the indoor as well as the outdoor environment.

1.4 MATLAB

The post-processing of the data described in this report are performed with MATLAB[2]. The abbreviation MATLAB stands for MATrix LABoratory. MATLAB is a high- performance language for technical computing. It integrates computation, visualisation, and programming in an environment where problems and solutions are expressed in familiar mathematical notation such as:

- Math and computation
- Algorithm development
- Modelling, simulation, and prototyping
- Data analysis, exploration, and visualisation
- Scientific and engineering graphics
- Application development, including Graphical User Interface building

MATLAB is an interactive system the basic data element of which is an array that does not require dimensioning. MATLAB has evolved over a period of years with input from many users. In university environments, it is the standard instructional tool for introductory and advanced courses in mathematics, engineering, and science. MATLAB features a family of application specific solutions called toolboxes. Toolboxes are comprehensive collections of MATLAB functions (M-files) that extend the MATLAB environment to solve particular classes of problems. Areas in which toolboxes are available include communication systems, signal processing, wavelets, simulation, etc.

MATLAB is created by The MathWorks, Inc. and is available in different versions for the MS Windows, UNIX and Macintosh operating systems. The post-processing of the data in this report is done on a UNIX operating system (HP 11.0), using MATLAB version 5.3.1. MATLAB uses several blocks from the Communications toolbox, version 1.4. More information on MATLAB can be found in their respective reference manuals or at: *http://www.mathworks.com*.

---

[2] MATLAB is registered trademarks of The MathWorks, Inc. Other product or brand names are trademarks or registered trademarks of their respective holders.

Chapter 2

Principle of antenna pattern diversity

2.1 Introduction

In order to optimize the signal-to-noise ratio (ν) diversity techniques can be applied. There are several diversity techniques e.g. space, frequency, antenna pattern, polarization, time and angle diversity. These diversity techniques can also appear as a combination of each (e.g. both space- and frequency diversity). The objective of this graduation project is to explore antenna pattern diversity.
In common mobile radio systems only simplex radio traffic is possible e.g pager. If the listener wants to talk too, a duplex scheme makes this possible. The user can only talk alternately as in the case of a porto phone or walkie-talkie. Unfortunately this duplex traffic principle does not work very well in practice because the subscribers want to talk simultaneously. The full duplex scheme makes this possible, e.g. the GSM system uses a full duplex scheme. In order to realize a full duplex link two frequencies are needed. In a GSM system reception (R_x) happens at a higher frequency band whilst transmission (T_x) happens at a lower frequency band (see Rappaport [1]). Therefore the radio characteristics of these two bands might not be the same. During the reception (from basestation to handset) the optimal diversity parameters are obtained and set; we want these optimal settings also to be used during transmission. If the latter is true then an optimal path is choosen where the most transmitted power arrives at the antennas of the basestation. This implies a better performance of the handset.

Another important reason to apply antenna pattern diversity is to save the battery power of the handset. E.g. if the GSM handset transmits a signal into free space the power is distributed in space. The base station, however, is located at one point in space so a lot of the power will not arrive at the antennas of the base station. With the help of antenna pattern diversity more power will be transmitted in the direction of the antennas of the base station.
We assume that the mobile telephone is in an indoor environment so that there is enough multipath propagation. Since the GSM system consists of two bands our purpose is to explore if the dominant propagation paths are frequency independent. It is desirable that the simulated data can be compared to the measured data in order to verify the results.

At Philips Research Laboratory Eindhoven a measurement set-up is available which is described in section 2.2. After that the principle of antenna pattern diversity is explained. In order to explore antenna pattern diversity a correlation where the frequency and space are variable is done in section 2.3. Finally a conclusion is drawn in section 2.5 with regard to correcting the measured data and antenna pattern diversity.

2.2 Measurement set-up

Although there are many measure set-ups available such as xy-table, robot-arms and rotating arms in a plane, within Philips Research an xy-table is used to scan the horizontal xy-plane. We will see in this section when measuring the radio channel some errors occur in the measured data.

2.2.1 Measurement set-up description

In order to explore antenna pattern diversity it may be obvious that we will have to know the GSM radio channel characteristics. In measuring these characteristics a measurement set-up is available (see Figure 2.1 or see Appendix D for a detailed picture). The measurement set-up consists of a xy-table where a prototype antenna can be mounted. The movable part of the xy-table moves in a horizontal plane with dimension 100 cm into x-direction and 80 cm into y-direction. Furthermore the movement is controlled by a xy-table controller and a PC. While the measurement is in progress the data (in complex form) will be sent from the network analyzer to the PC. After the data have been sent to the PC the measured data are being postprocessed to obtain the desired characteristics or information. For controlling the transmitting antenna as well as the receiving antenna the network anlyzer (HP 8753E) is used. Before the actual data can be processed first we have to correct the data. The reason for correcting the measured data will be discussed in the following subsection.

2.2.2 Correcting the measured data

The measurement set-up in Figure 2.1 can be modelled as shown in Figure 2.2. Cable characteristics (connected between the antennas and the network analyzer) and the low noise amplifier (LNA) are calibrated out so that the systematical errors does not occur in the data any more. Moreover the port extension option should be used to shift the reference planes to the end of the connectors of the cables
Once the network analyzer is calibrated the antenna itself also causes an error in the data. The impedance of the antennas consists of a real part R and a complex part X. The real part of the impedance can be subdivided into a dissipative part and a radiated part, $R = R_d + R_r$. Normally the dissipative part is much smaller than the radiated part, $R_d \ll R_r$ or $R \approx R_r$.

For instance, assume that the length L of the dipole antenna is $\lambda/2$ and the specific conductivity of iron is $\sigma_{Fe} = 6.667 \cdot 10^6\ \Omega^{-1}\ \mathrm{m}^{-1}$ then for a homogeneous wire with radius

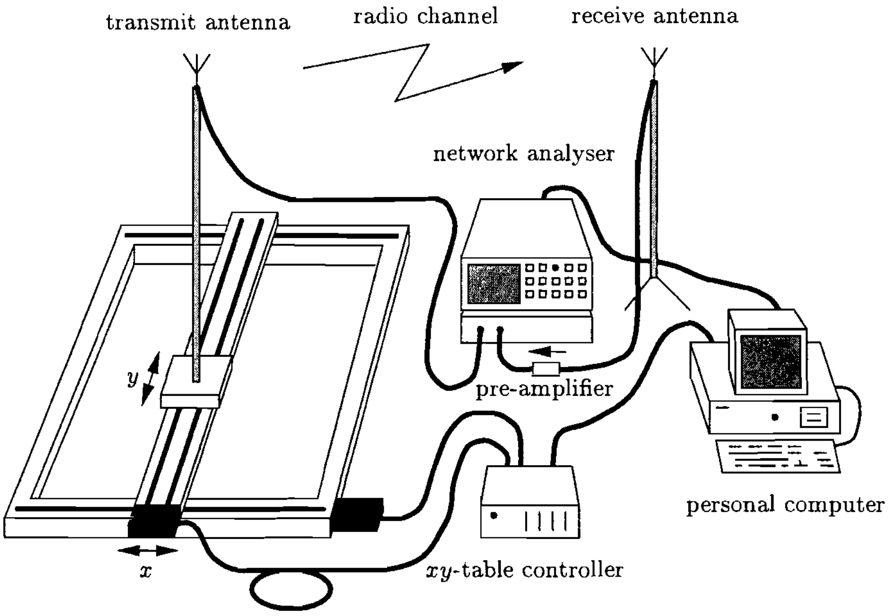

Figure 2.1: *Automated measurement set-up.*

$r_w = 0.25$ mm the skin depth becomes [3]

$$\delta_s = \sqrt{\frac{2}{\omega\mu_0\sigma_{Fe}}} \qquad [\mathrm{m}] \tag{2.1}$$

where $\omega = 18\pi\ 10^8$ radm^{-1}, $\mu_0 = 4\pi\ 10^{-7}$ VsA^{-1}m^{-1}. These values are substituted (2.1) to obtain the skin depth: 6.497 μm.
The AC impedance of a wire per unit of length is given by [3]

$$r = \frac{1}{2\pi r_w \delta_s \sigma_{Fe}} \qquad [\Omega\mathrm{m}^{-1}]. \tag{2.2}$$

Substituting r_w gives for the AC resistance: 14.69 Ωm^{-1}.
Because the current distribution along the wire is not a homegeneous function, the total resistance is not obtained by simply the multiplication of r with the length of the wire. The power loss in the wire is given by

$$P_l = \int_L I^2(z) r\, dz \qquad [\mathrm{W}]. \tag{2.3}$$

The current distribution on the wire is assumed to be a sinus function and are positioned vertically in the z-direction

$$I(z) = I_0 \cos(\frac{2\pi}{\lambda} z) \qquad [\mathrm{A}]. \tag{2.4}$$

This current distribution function is substituted in (2.3). The power loss becomes

$$P_l = \int_L I_0^2 \cos^2(\frac{2\pi}{\lambda} z) r\, dz = I_0^2 r \frac{\lambda}{4} \qquad [\mathrm{W}]. \tag{2.5}$$

The dissipative resistance becomes

$$R_d = \frac{P_l}{I_0^2} = r\frac{\lambda}{4} \approx 1 \qquad [\Omega]. \tag{2.6}$$

Numerical calculations (e.g. NEC) give a total input resistance of 26.36 Ω, so four percent of the total resistance is responsible for heating the wire or 96% of the total resistance consists of radiation resistance. Therefore we can neglect R_d. So in figure 2.2 R_t and R_r denote the radiation resistances.

The signal strength should not be drown by noise. Therefore the source power of the network analyzer is adjusted at 20 dBm. The LNA is used to improve the overall noise figure of the radio network and amplifies the signal with 27 dB within a bandwidth of 10-3000 MHz. We should take care of the maximum input power of the reception port of the network analyzer which is +26 dBm. When examining Figure 2.2 we learn that the *measured data* are S_{21} or S_{12} and do not represent the actual radio channel because the antennas mismatches and the antenna gain functions ($G_{T_x}(\theta,\phi)$, $G_{R_x}(\theta,\phi)$,[4]) are included in these measurements. These mismatches cause reflections at the antenna terminals. Reflection is defined as the part of the transmitted power P_t which will be reflected. The formula would be $P_{reflected} = |S_{11}|^2 \cdot |P_t|$. Correcting the antenna mismatch is possible whereas a correction for the antenna gain functions is not possible. Apparently the radio channel is defined as the actual radio channel plus the antenna radiation patterns.

The measured data obtained from the network analyzer is put in an $M \times F$ matrix form, where M is the number of observation points of the xy-table and F the number of

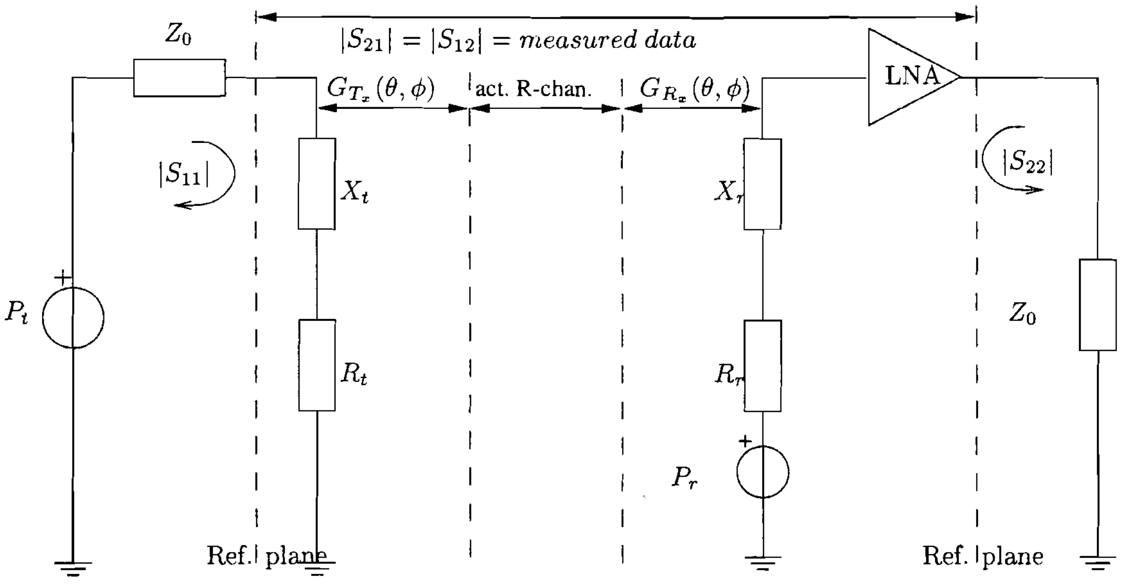

Figure 2.2: *Schematic model of the radio network.*

frequency points. For correction the radio equation of Collin [3] can be used.

$$P_r = (1-|S_{11}|^2)\cdot(1-|S_{22}|^2)\cdot G_{T_x}(\theta,\phi)\cdot G_{R_x}(\theta,\phi)\cdot P_t\cdot\left(\frac{\lambda}{4\pi r}\right)^{\alpha}\cdot p \quad [\mathrm{W}]$$
$$|S_{21}|^2 = \frac{P_r}{P_t} = (1-|S_{11}|^2)\cdot(1-|S_{22}|^2)\cdot G_{T_x}(\theta,\phi)\cdot G_{R_x}(\theta,\phi)\cdot\left(\frac{\lambda}{4\pi r}\right)^{\alpha}\cdot p \tag{2.7}$$

where α is the path loss exponent, from Rappaport [1, p104] the LOS component lies within $1.6 \leq \alpha \leq 1.8$ and p is the polarization loss. According to Rappaport the inbuiling LOS path loss α equals to 1.6 and p will not be used in the correction formula. In equation (2.7) $\frac{P_r}{P_t}$ is in our case equal to $|S_{21}|^2$ the transfer function, measured with the network analyzer, so the corrected transfer function is equal to

$$\frac{|S_{21}|^2}{(1-|S_{11}|^2)\cdot(1-|S_{22}|^2)} = G_{T_x}(\theta,\phi)\cdot G_{R_x}(\theta,\phi)\cdot\left(\frac{\lambda}{4\pi r}\right)^{1.6} \tag{2.8}$$

So the corrected measured data matrix (based on powers) is done as follows. Define a matrix A which consists of uncorrected measured data as

$$\mathbf{A} = \begin{bmatrix} a_{11} & a_{12} & \cdots & a_{1F} \\ a_{21} & a_{22} & \cdots & a_{2F} \\ \vdots & \vdots & \ddots & \vdots \\ a_{M1} & a_{M2} & \cdots & a_{MF} \end{bmatrix}$$

where a_{ij} stands for the measured transfer $|S_{21}|^2$ at the i^{th} point from the xy-table at j^{th} frequency. Define a matrix B which consists of reflection coefficients as

$$\mathbf{B} = \begin{bmatrix} b_{11} & b_{12} & \cdots & b_{1F} \\ b_{21} & b_{22} & \cdots & b_{2F} \\ \vdots & \vdots & \ddots & \vdots \\ b_{M1} & b_{M2} & \cdots & b_{MF} \end{bmatrix}$$

with

$$b_{ij} = \frac{1}{(1-\left|S_{ij}^{11}\right|^2)\cdot(1-\left|S_{ij}^{22}\right|^2)}$$

where b_{ij} stands for the reflection coefficient at the i^{th} point from the xy-table at j^{th} frequency. Finally the corrected measured data is calculated by

$$\mathbf{C} = \mathbf{A} * \mathbf{B} = \begin{bmatrix} a_{11} & a_{12} & \cdots & a_{1F} \\ a_{21} & a_{22} & \cdots & a_{2F} \\ \vdots & \vdots & \ddots & \vdots \\ a_{M1} & a_{M2} & \cdots & a_{MF} \end{bmatrix} * \begin{bmatrix} b_{11} & b_{12} & \cdots & b_{1F} \\ b_{21} & b_{22} & \cdots & b_{2F} \\ \vdots & \vdots & \ddots & \vdots \\ b_{M1} & b_{M2} & \cdots & b_{MF} \end{bmatrix} \tag{2.9}$$

where the mathematical operator * stands for a row multiplying instead of matrix multiplying.

Generally speaking the bandwidth of the dipole is defined as this frequency area where

90% of the power is transmitted (or 10% of the power is reflected). Furthermore the resonant frequency is defined as the frequency where the impedance is purely real (or the imaginary part is zero). If the dipole antennas are properly designed and the bandwidth of the radio channel is not too large the difference between the uncorrected data and the corrected data should be small as illustrated in Figure 2.3. This implies that the correction is not necessary but is optional. Since the difference between the corrected data and the uncorrected data is negligible, the uncorrected data will be used during this report. The reason for this is that the phase information after correction will be lost. Moreover some applications which will be used later on in this report need complex data as input. The complex data are obtained directly from the network analyzer.

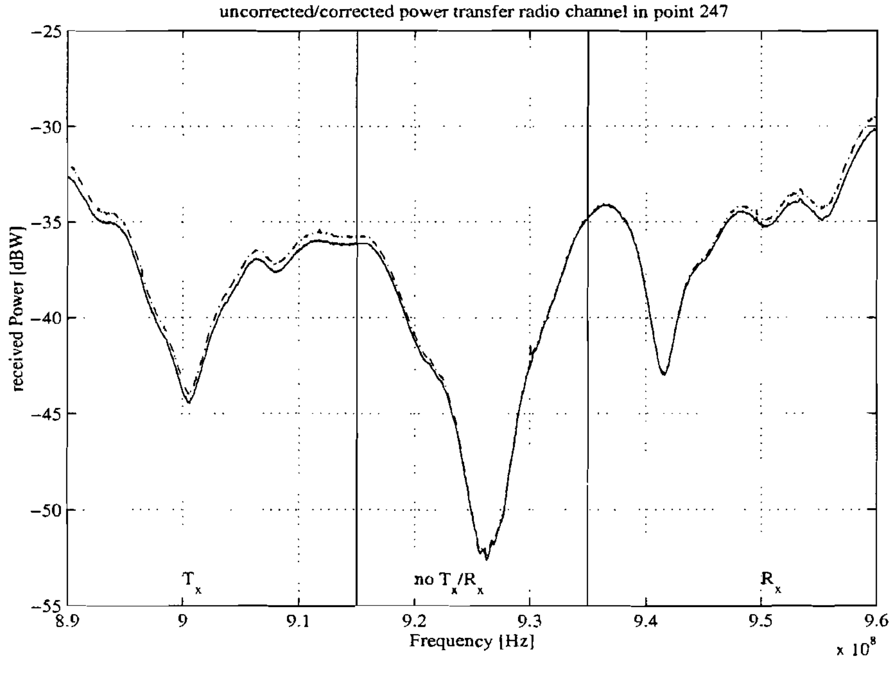

Figure 2.3: *Radio channel of GSM band (Solid:uncorrected; dashed-dot:corrected).*

2.3 Antenna pattern diversity

In indoor or outdoor environment we usually deal with more than one signal path (multipath propagation). Trees, hedges, buildings or other objects cause reflection and attenuation of the transmitted signal. If one antenna is used the received signal at its terminals consists of multiple replicas of the transmitted signal as depicted in Figure 2.4. On one hand the received signal strength may be strong but on the other hand the signal strength may be very weak (read, the signal power lies in the vicinity of the noise power). It depends on the individual phases if the signal strength is strong (constructive interference) or poor (destructive interference). This will be made plausible in the following example. Suppose a line of sight (LOS) does not exist then signal path S_2 will be blocked by an object and S_3 and S_4 are the dominant signal paths (see Figure 2.4). Signal S_1 is assumed to have such a low power that it does not significantly contribute to the received power. If the phase difference between these two signals is 180 degrees then the received signal

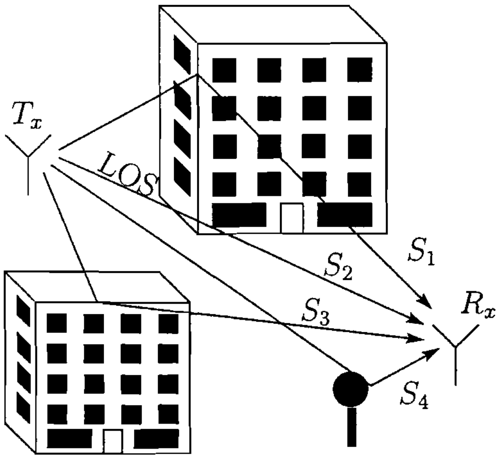

Figure 2.4: *Multipath propagation in an outdoor environment where* S_1, S_2, S_3, S_4 *represents the dominant propagation paths.*

level is very poor that is why it is also called destructive interference. In order to obtain diversity it is desirable that one of these two signals can be muted. So this means that during the reception the zero of the radiation pattern or the smallest lobe of the radiation pattern is adjusted in such a way that signal S_4 will be muted by this zero or smallest lobe. A destructive interference does not occur any more; this is also true for the opposite case (where S_3 is muted). Figure 2.5 shows this graphically and shows the antenna pattern diversity. In state four, both S_3 and S_4 are equivalently received which causes destructive interference. Consequently the detector decides to switch from state four to state one. In this state signal S_4 will be muted due to the antenna's radiation characteristic whilst signal S_3 will not be muted. This will result in a better reception than in state four. In this example state three could also have been used in which case signal S_3 would be muted and signal S_4 not would not be muted . In state two both signal S_3 and signal S_4 will be muted which will result in a poor reception. In this example a fixed frequency has been used and four states are used (this is an arbitrary choice). In the GSM system, however, the reception band and the transmission band are separated in frequency. Moreover the reception and the transmission band have a certain frequency bandwidth. This implies that these four far field patterns must be the same in the transmission band and in the reception band. In addition to that these far field patterns must be the same the dominant waves must also be the same in these bands. E.g. if these dominant waves varies strongly as function of frequency then switching between these far field patterns is useless. So the principle of antenna pattern diversity in general is dealing with AOA. These AOA's have to be frequency independent in the concerning bandwidth. In order to obtain this information a channel correlation has been carried out (see following section).

2.4 Correlation based on powers

The standard or primary GSM 900 band or briefly GSM is subdivided into two subbands. These bands are

- 890-915 MHz : mobile transmit, base receive (Reverse Channel Frequency)

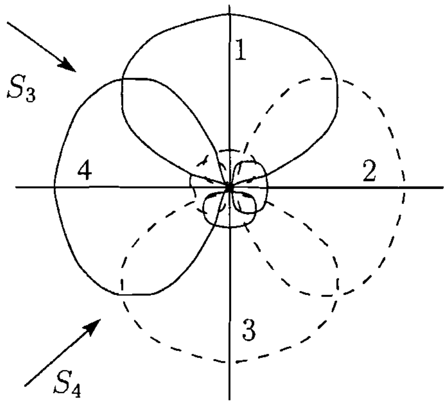

Figure 2.5: *Radiation pattern adjusting using four arbritrary radiation patterns.*

- 935-960 MHz : base transmit, mobile receive (Forward channel Frequency).

The reason for this allocation of the frequencies can be deduced from the fact that the power efficiency of the power amplifier would be less if these higher frequencies would be used. A poor power efficiency would reduce the battery life time. So people would have to recharge their battery of the GSM handset frequently.
The GSM carrier spacing is 200 kHz and is designated by the Absolute Radio Frequency Channel Number (ARFCN). If $F_\ell(n)$ is the frequency value of the ARFCN n in the lower band (R_x), and $F_u(n)$ is the corresponding frequency value in the upper band (T_x), then the channels (frequency are in MHz) are :

$$\begin{aligned} F_\ell(n) &= 890 + 0.2 \cdot n \\ F_u(n) &= F_\ell(n) + 45 \end{aligned} \qquad \{\forall_{n \in \mathcal{N}} | 1 \leq n \leq 124\} \tag{2.10}$$

In (2.10) the number 45 MHz denotes the T_x/R_x separation. Moreover a channel is time shared between as many as eight subscribers using TDMA. Each of the eight subscribers uses the same ARFCN and occupies a unique time slot (TS) per frame. This will result in 8*124=992 subscribers, including guard bands on the edges of the T_x/R_x band (see Figure 2.6). In order to explore antenna pattern diversity the GSM frequency band is measured, this will be done using to the automated measurement set-up (see Figure 2.1). The xy-plane is subdivided into discrete points called the observations points. The number of steps in the x or y-direction is relative with respect to the wavelength. To avoid permanent damage of the xy-table, its physical dimensions should not be exceeded. Therefore the number of wavelengths in the x-direction is set to 3 and for the y-direction to 2 where the

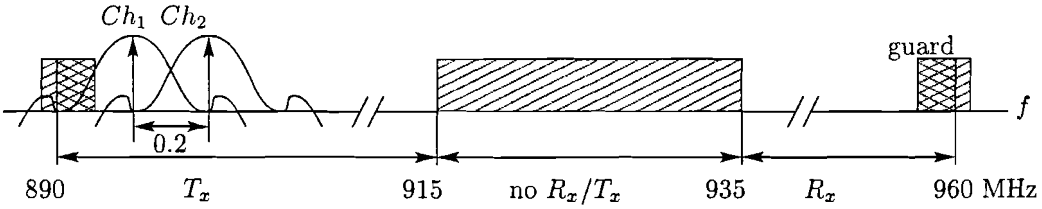

Figure 2.6: *GSM 900 frequency spectrum arrangement.*

wavelength is calculated from the stop frequency which is 960 MHz in our case. Number of steps per wavelength is set to six steps which gives a total of $(3\times 6+1)\cdot(2\times 6+1) = 247$ observation points. Further on, the GSM frequency band is subdivided into subintervals of equal lengths Δf depending on the number of frequency points F. In our case F is equal to1601 which is the maximum number of frequency points allowed. This results in a step frequency or frequency resolution $\Delta f = \frac{70\times 10^6}{1600} = 43.75 \times 10^3$ [Hz].
The data from the network analyzer is formed to an array of a total number of $247\times 1601 = 395447$ elements. After the array has been formed MATLAB reshapes the array in a more readable matrix with dimension $M \times F$ where M is the number of observations points and F is the number of frequency components as mentioned before. This will result in two possibilities to investigate antenna pattern diversity. Namely a correlation matrix where the frequency components are regarded as variable and one where the observation points are used as variable. The former gives information about frequency diversity and the latter gives information about space diversity. The results are discussed in the following two sub-sections.

2.4.1 Frequency diversity

The correlation matrix which has been calculated is based on powers and matrix $\mathbf{C}$ is used as entry for the correlation function. Once the correlation is applied a new matrix is formed with dimension $F \times F$ see (2.11). The coefficients in the correlation matrix should be read as, the i^{th} column correlated with the j^{th} the column of the data matrix $\mathbf{C}$ with $i, j \in F$. Characteristic of this matrix is the symmetry along the main diagonal and the 1's on the diagonal.

$$\rho_{\mathrm{fd}} = \begin{bmatrix} \rho_{11} & \rho_{12} & \cdots & \rho_{1F} \\ \rho_{21} & \rho_{22} & \cdots & \rho_{2F} \\ \vdots & \vdots & \ddots & \vdots \\ \rho_{F1} & \rho_{F2} & \cdots & \rho_{FF} \end{bmatrix} \tag{2.11}$$

In order to obtain a more comprehensive insight in the correlation matrix the distribution is plotted against Δf or the channel spacing (see Figure 2.7). When studying Figure 2.7 we will see that the curve drops very rapidly. Adjacent channels ($|\Delta f| \leq 5$ MHz) have a relative good correlation. Unfortunately the T_x/R_x separation is 45 MHz and gives according to Figure 2.7 a low correlation coefficient of approx. 0.2. This number, however, is not accurate because at the edges of the ρ_{fd} plot the data are not reliable. The reason for this unreliability is that there are too few data points to obtain proper statistics. When the channel spacing is increased the number of coefficient which have these channel spacing will decrease. At a channel spacing of 70 MHz only two points are available (ρ_{1F} and ρ_{F1}). Therefore the valid range lies approximately within $|\Delta f| \leq 35$ MHz. Figure 2.7 makes clear that if we want to apply frequency diversity the best candidate frequency are these frequencies which have a channel spacing bigger than approximately 0.5 MHz. At 0.5 MHz the correlation coefficient is equal to 0.5. We could also use a coefficient of 0.4, as the boundary where correlated signals get decorrelated. It depends on the situation, sometimes a correlation coefficient of 0.4 is necessary and sometimes a correlation coefficient of 0.7 is acceptable. So it may appear that the boundary from correlated signals to decorrelated signals has a more subjective character rather then an analytical character.

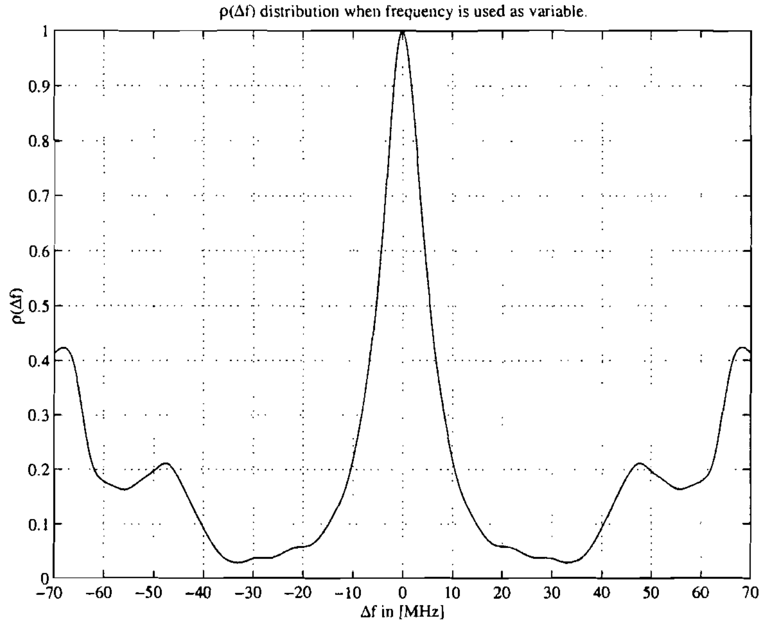

Figure 2.7: $\rho(\Delta f)$ *correlation distribution, when the frequency is used as variable.*

In this report a boundary of 0.7 has been chosen. According to Figure 2.7 the bandwidth (single sided) is equal to 3,543,750.0 Hz or rounded off towards 3.5 MHz. Within this bandwidth the frequencies can be treated as having the same radio channel characteristics. If we refer to frequency diversity the frequencies should have to be chosen outside this bandwidth.

Unfortunately frequency diversity does not give any information about antenna pattern diversity where the AOA is important. It gives indirect information about the interference behaviour. In this sub-section the frequency was used as being a variable. Another variable which can be considered is the observation point which will be discussed in the next sub-section.

2.4.2 Space diversity

In this case the data matrix **C** has to be transposed in order to make the observation point variable. This changes the dimension of the correlation matrix into $M \times M$ (see (2.12)).

$$\rho_{\text{sd}} = \begin{bmatrix} \rho_{11} & \rho_{12} & \cdots & \rho_{1M} \\ \rho_{21} & \rho_{22} & \cdots & \rho_{2M} \\ \vdots & \vdots & \ddots & \vdots \\ \rho_{M1} & \rho_{M2} & \cdots & \rho_{MM} \end{bmatrix} \tag{2.12}$$

The number of observation points equals to $(19 \times 13) = 247$ so we can plot correlation distribution along a axis. Choose for instance the y-axis of the xy-table. When using the y-axis the step-size or the resolution Δy equals to λ divided by the steps per wavelength in the y-direction which is 6. So the step-size equals to 0.0521 meters. Having these settings the total array length is $13 * 0.0521 = 0.6771$ meters. Therefore the correlation

distribution will be plotted as function of $\Delta y/\lambda$ for the x and y-direction. In this case the same statistics limitations as mentioned in section 2.4.1 also hold good.
During a measurement the receiving antenna shifts through the xy-plane as depicted in Figure 2.8.

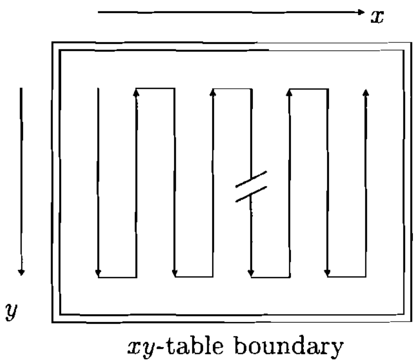

Figure 2.8: *Movement sequence of the xy-table.*

It will start with the y-direction and increment with the x-direction. According to Figure 2.8 the y-direction shifts down and up instead of only up or only down. The data sequence of the even x numbers are read reversely compared to the odd x numbers. This implies that after the data have been read the data sequence has to be corrected for the odd x numbers in order to obtain an unambiguous data sequence. Once the data have been corrected a correlation distribution plots can be made which are shown in Figure 2.9.
In studying Figure 2.9 the measured data behaves like a bessel function of order zero. This behaviour has also been found by Jakes [6, p39]. This means that for space diversity the location of the second antenna (or multiple antennas) should be placed at a distance of 0.25 λ from one other. Spacings closer than 0.25 λ result in small diversity gains because the received signals are highly correlated.
Due to the finite data points the curves in Figure 2.9 have a non-smooth path.

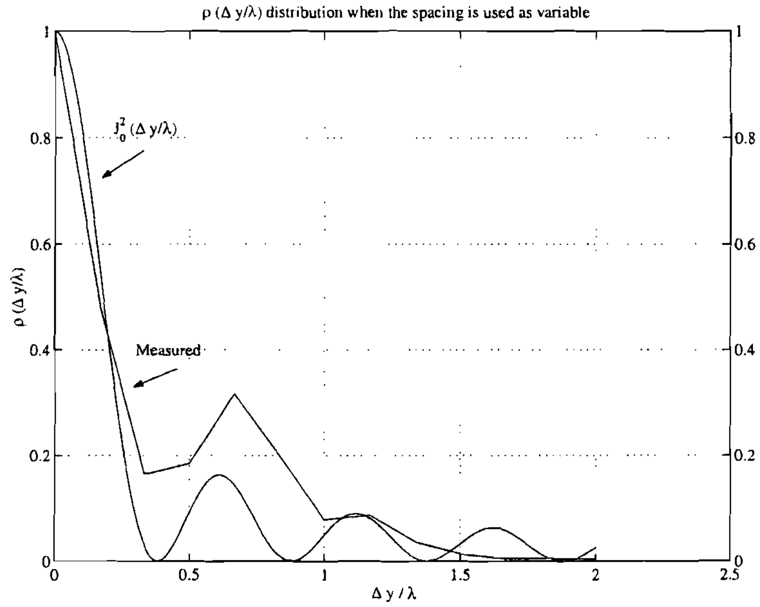

(a) y-direction

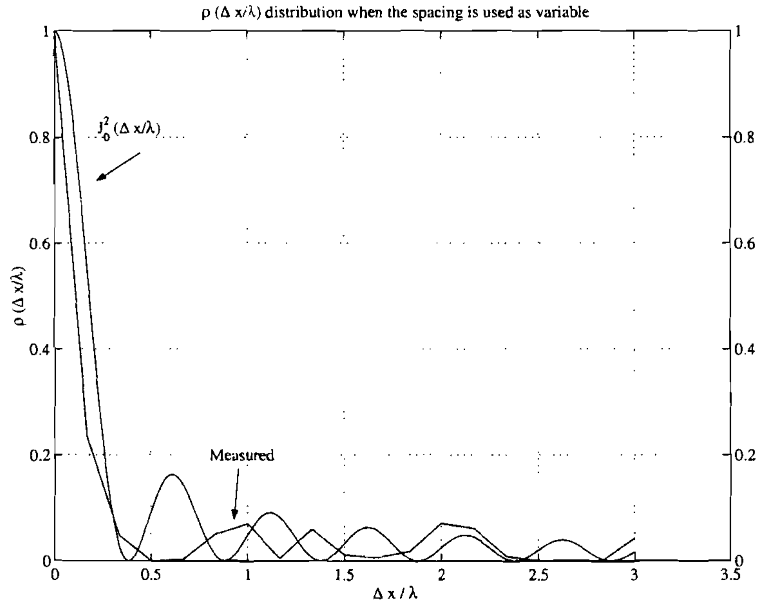

(b) x-direction

Figure 2.9: $\rho(\Delta x)$ *correlation distribution, when the space is used as variable.*

In this case no information about the AOA is obtained for which reason we are forced to use a more sophisticated method dealing directly with AOA's.

2.5 Conclusion

In this chapter it was shown that if the antennas are properly designed a correction for the antenna mismatches is not necessary . Therefore the correction can be omitted and is rather optional. When using the correction we should be aware that the phase information will be lost.

Antenna pattern diversity principle was explained. It was shown that the angle of arrival plays a dominant part in evaluating antenna pattern diversity.

Two attempts were made in order to obtain information about the angle of arrival, one with frequency diversity and the other with space diversity. The correlation plots based on powers where both frequency separation and the antenna separation are used as variables to calculate the correlation distribution. Unfortunately it does not give us the right answers about AOA. For the former if for one particular frequency component the received power is high (little destructive interference) and for another frequency component the received power is low (much destructive interference) this will result in a low correlation coefficient. For the latter observation points close to each other result in high correlation coefficients.

At this point it is clear that the correlation distribution plots do not give us any information about AOA. Therefore a literature survey on AOA was carried out. Several algorithms were found which extract the AOA's. In this report two prominent algorithms are explored namely the Fourier transform (FT) chapter 3 and the eigenstructure based MUSIC algorithm chapter 4. Of course there are some other algorithms to extract AOA such as ESPRIT [20].

Chapter 3

AOA with Fourier transform

3.1 Introduction

There are many applications of the Fourier transform e.g. the conventional time to frequency transformation. In this chapter another application of the Fourier transform will be discussed which is the angle to space transformation. Instead of frequency s^{-1} we should talk about spatial frequency m^{-1}. First formulas for the (Discrete) Fourier transform will be derived in section 3.2, after that the Fourier method will be tested on well defined plane waves data in section 3.3. This is done in order to investigate the influences of the signal-to-noise ratio and aperture length on the spatial resolution. A conclusion is drawn in section 3.4.

3.2 Fourier transform

In using the Fourier transform the assumption is made that the incident waves on the array can be treated as plane waves. So the distance between transmitter and receiver must be large enough to guarantee the plane waves hypothesis (far field or Fraunhofer region). If the aperture length of the uniform linear array (ULA) should become too long then the waves composition along the array might not be fixed. In order to derive the equation for the received field Figure 3.1 is used. When dealing with plane waves the received signal at each antenna element can be expressed in its relative delay with respect to a reference antenna element. This is called a plane wave expansion. Consider the synthetic ULA consisting of $m = 0, 1, \cdots, M-1$ antenna elements. Each element will receive noise

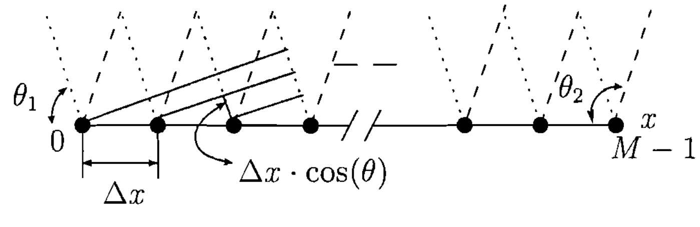

Figure 3.1: *Multiple planes waves incident on (synthetic) ULA which consists of M antenna elements.*

n_m whether sensed along with the signals or noise originating from instruments. The dotted line and the dashed line represent the phase front of the incident field coming from a direction θ_d. Taking the first antenna element at $x = 0$ as reference point then each antenna element will receive with respect to that reference point

$$\begin{aligned} r_m(m\Delta x) &= \sum_{d=0}^{D-1} b(\frac{\cos(\theta_d)}{\lambda}) \cdot e^{j\frac{2\pi}{\lambda}\cdot m\cdot\Delta x\cdot\cos(\theta_d)} + n_m \\ &= \sum_{d=0}^{D-1} b(u_d) \cdot e^{j2\pi\cdot m\cdot\Delta x\cdot u_d} + n_m \end{aligned} \tag{3.1}$$

where $b(u_d)$ is the amplitude of the measured d^{th} signal (including antenna radiation characteristics), D is the number of plane waves incident on the array and $u_d = \frac{\cos(\theta_d)}{\lambda}$ [m^{-1}] is called the spatial frequency. Later on in this report (chapter 4) u_d will be redefined as $u_d = \frac{2\pi\Delta x\cos(\theta_d)}{\lambda}$ [rad]. In case of the Fourier transform, it is for convenience sake to use the former definition of the spatial frequency.

The summation in (3.1) can be interpreted as a Discrete Fourier Transform (DFT). Discretising u_d gives $d\Delta u$ where Δu is the stepsize in the spatial domain. In order to make the distinction between the continue case and the discrete case the parentheses are replaced by square brackets. Thus, $r(m\Delta x)$ and $b(d\Delta u)$ are rewritten as $r[m]$ and $b[d]$ respectively. Equation (3.1) then becomes (for the sake of simplicity noise is neglected)

$$r[m] = \sum_{d=0}^{D-1} b[d]e^{j\frac{2\pi}{M}\cdot m\cdot d} \tag{3.2}$$

where $\Delta x \cdot \Delta u = 1/M$.

In order to obtain AOA or $b[d]$ the Inverse Discrete Fourier Transform (IFTD) must be applied.

$$b[d] = \frac{1}{M}\sum_{m=0}^{M-1} r[m]e^{-j\frac{2\pi}{M}\cdot m\cdot d} \tag{3.3}$$

The factor $\frac{1}{M}$ in front of the summation sign is chosen in such a way that after applying the DFT and the IDFT the function $b[d]$ is actually regained. The discrete Fourier transform as described above is only valid for periodical (discrete) signals. In our case we have a finite number of data points which is not periodical. To overcome this problem the data will be assumed to be periodically continued. In that case a new problem will occur namely due to the fact that the data is finite sidelobs will occur in the transformed signal. This can be explained as follows. Mathematically speaking the Fourier transform will be performed form $-\infty$ to ∞. In the discrete case, we need an infinite number of points. Real data have a finite number of points M. Actually the infinite number of data points have been (virtually) multiplied by a rectangular window. Multiplying in one domain gives a convolution in the other domain. To smooth the finite data sequence a Gaussian window will be used. With the help of windowing some information will be lost called process loss. So a compromise between the side-lobe level and the process loss has to be made. This compromise is investigated by F.J. Harris [17], with the help of his paper a suitable

Gaussian window is applied to the simulated data. Readers who are not familiar with windowing are advised to read digital *"signal processing"* by van den Enden & Verhoeckx [2].

Finally we have the following Fourier transformation pair

$$\begin{aligned} r[m] &= \sum_{d=0}^{D-1} b[d] e^{j\frac{2\pi}{M}\cdot m\cdot d} \qquad & b[d] \xrightarrow{DFT} r[m] \\ b[d] &= \frac{1}{M}\sum_{m=0}^{M-1} r[m] e^{-j\frac{2\pi}{M}\cdot m\cdot d} \qquad & r[m] \xrightarrow{IDFT} b[d] \end{aligned} \tag{3.4}$$

The angle information, which we are interested in, is obtained by taking the inverse discrete Fourier transform. Note that $r[m]$ is actually the windowed version of the real data, in this report there will be no distinction between the actual data and the filtered version of it. Stepsize in the spatial domain is given by $\Delta u = 1/(M \cdot \Delta x)$ which gives us the spatial resolution. $M \cdot \Delta x$ is the total aperture length, the greater the aperture length the better the spatial resolution. When the aperture length is fixed the spatial resolution will become independent on the number of antenna elements. If we want to detect D incident plane waves then the number of antenna elements should be at least equal to D or greater than D .

In the following section the DFT will be put to the test with a well defined set of incident plane waves. Furthermore noise will be added to each signal to emulate the real world.

3.3 Simulated data

In order to verify the Fourier method three well defined plane waves coming from a direction at 70, 80 and 120 degrees are considered. The Fourier method is illustrated in Figure 3.2 where at the same time the aperture length is used as parameter. Noise having a Gaussian normal distribution with a zero mean μ and variance σ^2 is added to each signal. The frequency of the simulated data is set to 960 MHz corresponding to a wavelength of 0.3125 m. Figure 3.2 shows the Fourier spectrum at a signal-to-noise ratio of 46.84 dB. The dashed-dotted vertical lines in Figure 3.2 form the boundaries of the spatial domain. Within this boundary we have valid data. To deduce the boundaries we need the formula of the spatial frequency and is repeated below

$$u_d = \frac{\cos(\theta_d)}{\lambda} \qquad \theta_d \in [0, 180] \tag{3.5}$$

Figure 3.3 shows this relation in a graphical way. It says that the valid spatial boundary lies between $|\lambda^{-1}|$. (3.5) tells us if λ becomes small (corresponding with increasing frequency) then the boundaries increases. As mentioned before the resolution depends on the aperture length (see also Figure 3.2). In our case the largest aperture length is the x-side of the xy-table and equals to one meter. The resolution is obtained by taking the derivative of (3.5)

$$|\Delta\theta_d| = \left|\frac{\lambda \cdot \Delta u_d}{\sin(\theta_d)}\right| \qquad \theta_d \in (0, 180) \tag{3.6}$$

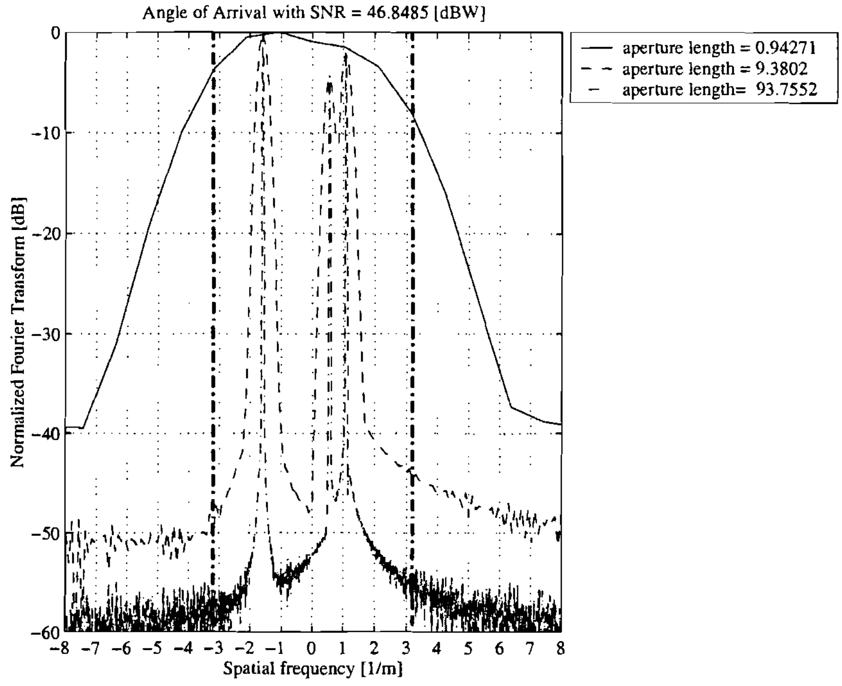

Figure 3.2: *Fourier spectrum with three plane waves incident on ULA at 70, 80 and 120 degrees with aperture length as parameter (length shown in meters).*

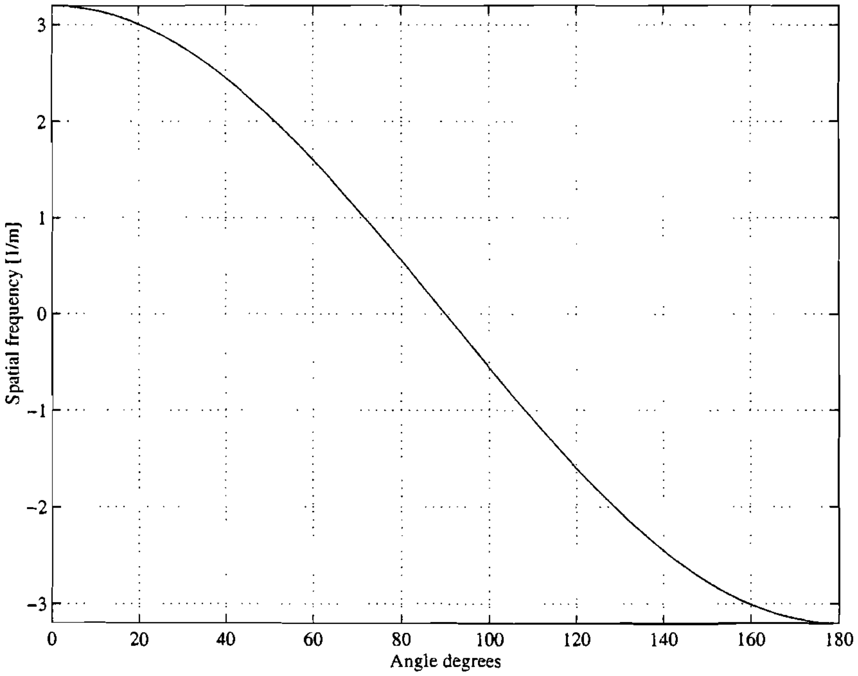

Figure 3.3: *Boundary of spatial frequency vs. angle.*

which is plotted in Figure 3.4. With an aperture length of about one meter we have a bad resolution as can been seen from Figure 3.4 (solid line). Increasing the aperture length improves the spatial resolution (cf. Figure 3.2). Unfortunately the physical dimensions of the xy-table are limited to 1 m x 0.8 m. Therefore improving the spatial resolution cannot be done by means of enlarging the aperture length. An aperture length of 93.75 m is of course of no practical importance and is only used in illustrations. The only parameter that will be left to improve the spatial resolution is the signal-to-noise ratio. If the signal-to-noise ratio is used as parameter the noise floor raises when lowering the signal-to-noise ratio (Figure 3.5 is illustrating this). As we can see the spatial resolution is not affected by increasing the ν. The amplitudes for the incident waves are set to $b_1 = 0.7$ V, $b_2 = 0.4$ V and $b_3 = 1.1$ V. In Table 3.1 the estimated amplitudes are shown including the relative errors. Hats on the characters denote estimations whilst L denotes the aperture length. The relative errors are calculated as follows: $|(b_x - \hat{b}_x)/b_x| \times 100\%$ with $x = 1, 2, 3$. These errors are displayed in the table by means of a Δ. A remarkable perceptibility is that when increasing the aperture length the amplitudes received are not better estimated. A possible explanation for this occurrence is that the Gauss filter causes process losses which cannot be avoided (which has been explored by Harris [17]).

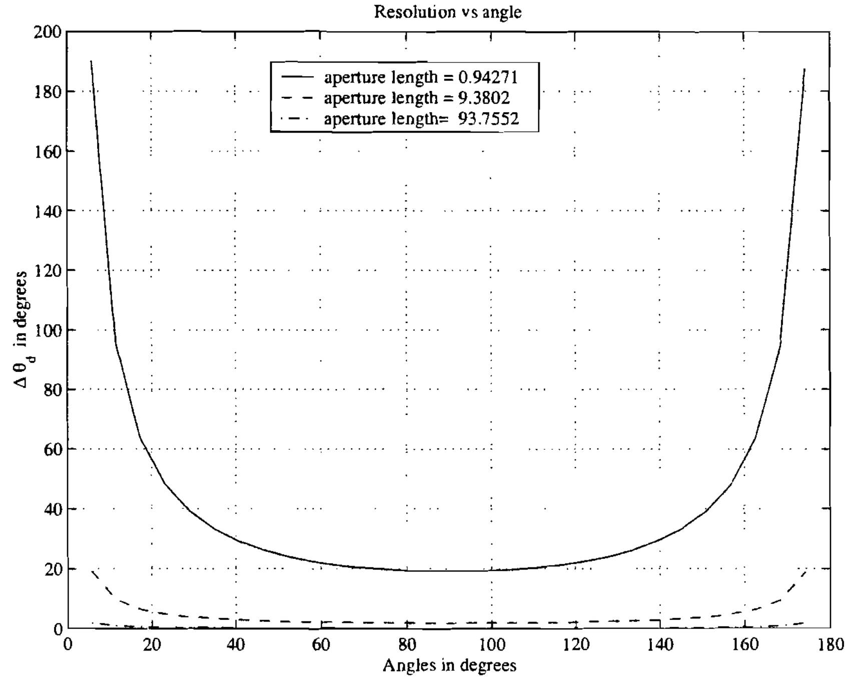

Figure 3.4: *Resolution vs. angle with the aperture length as parameter (length shown in meters).*

	$\hat{b}_1$ / Δ	$\hat{b}_2$ / Δ	$\hat{b}_3$ / Δ
L=0.9427 m	Not Est.	Not Est.	Not Est
L=9.3802 m	0.620 / 11.43%	0.357 / 10.75%	1.000 / 10.00%
L=93.755 m	0.602 / 14.00%	0.362 / 9.50%	1.000 / 10.00%

Table 3.1: Estimated amplitudes and the relative error Δ.

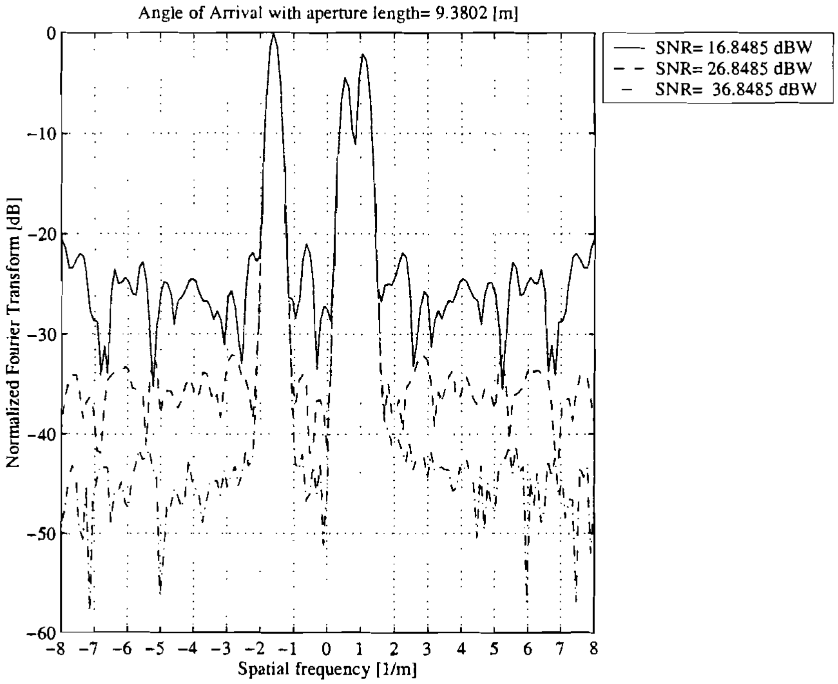

Figure 3.5: *Fourier transform with signal-to-noise-ratio as parameter.*

3.4 Conclusion

When using the Fourier transform we can conclude that the aperture length is the dominant factor whereas the signal-to-noise does not influence the spatial resolution. If we would use the xy-table with the largest side as aperture for our measurements then we could expect a low spatial resolution of approx. 20 degrees (cf. Figure 3.4). Since the xy-table has a fixed dimension a different algorithm has to be found to overcome the poor spatial resolution which this will be discussed in the following chapter.

Chapter 4

AOA with MUSIC algorithm

4.1 Introduction

As the Fourier method failed to obtain a good spatial resolution for a small aperture length we need another algorithm to solve this problem. In literature there are a lot of algorithms based on an eigenstructure technique. This is a totally different approach as compared to the Fourier method. These eigenstructure-based algorithms need a covariance matrix as entry. From the measured data which are put in the form of a vector the covariance matrix will be calculated and afterwards the eigenstructure of this covariance matrix will be computed. The eigenstructure is split up into two subspaces, the signal subspace and the noise subspace. Splitting up the eigenstructure is the heart of the algorithm. MUltiple SIgnal Classification (MUSIC) is an eigenstructure based algorithm and will be described section 4.2. In section 4.3 two spatial preprocessing schemes are described. After that MUSIC is put to the test in section 4.4. Ultimately in section 4.5 the Fourier method and the MUSIC algorithm is compared with one other.

4.2 The MUSIC algorithm

MUSIC is based on the orthogonalism of two subspaces called signal subspace and noise subspace. Though MUSIC also depends on the aperture length it will give a better spatial resolution as will be shown in this chapter. (3.1) can also be written as a matrix equation:

$$\begin{bmatrix} x_1 \\ x_2 \\ \vdots \\ x_M \end{bmatrix} = \begin{bmatrix} \\ \underline{a}(\theta_1) & \underline{a}(\theta_2) & \cdots & \underline{a}(\theta_D) \\ \\ \\ \end{bmatrix} \cdot \begin{bmatrix} b_1 \\ b_2 \\ \vdots \\ b_D \end{bmatrix} + \begin{bmatrix} n_1 \\ n_2 \\ \vdots \\ n_M \end{bmatrix} \tag{4.1}$$

where

$$\underline{a}(\theta_d) = \begin{bmatrix} 1 & e^{j\frac{2\pi}{\lambda}\cdot\Delta x\cdot\cos(\theta_d)} & e^{j\frac{2\pi}{\lambda}\cdot 2\cdot\Delta x\cdot\cos(\theta_d)} & \ldots & e^{j\frac{2\pi}{\lambda}\cdot(M-1)\cdot\Delta x\cdot\cos(\theta_d)} \end{bmatrix}^T$$

called the mode vector.

In order to avoid elaborated mathematical calculations only a short review is given of the algorithm but for the interested reader a thorough study of MUSIC is given in Schmidt [18].

(4.1) can be written in vector notation as $\underline{x} = A\underline{b} + \underline{n}$. Generally speaking the elements of $\underline{x}$ and A are complex. In A the a_{ij} elements are known functions of angle of arrival and the relative element locations from the origin. Schmidt [18] defines The $M \times M$ covariance matrix R of the $\underline{x}$ vector as

$$R \overset{\mathrm{def}}{=} E\left[\underline{x}\,\underline{x}^H\right] = AE\left[\underline{b}\,\underline{b}^H\right]A^H + E\left[\underline{n}\,\underline{n}^H\right] = APA^H + \sigma^2 I \tag{4.2}$$

where E[•] stands for the expectation operator, H denotes the Hermitian transpose and D is the total number of incident plane waves. In (4.2) $P = E[\underline{b}\underline{b}^H]$ denotes the signal covariance matrix, $\sigma^2 I = E[\underline{n}\underline{n}^H]$ denotes the noise covariance matrix. If the incident signals are perfectly decorrelated the covariance matrix P should only be a diagonal matrix. In practice the incident signals are somewhat correlated (especially in indoor environments), therefore the non-diagonal elements are non-zero. Further on matrix P is symmetrical along the diagonal and we can postulate that the incident signals and the noise are *uncorrelated.* Assuming the covariance matrix P to be non-singular, it can be shown that the covariance matrix R has exactly $M - D$ eigenvalues that are equal to σ^2. A set of two orthogonal bases can be defined called subspaces which are:
$S = < \underline{e}_1, \underline{e}_2, \cdots, \underline{e}_D >$ the signal subspace with dimension D and its orthoplement with dimension M-D
$S^\perp = < \underline{e}_{D+1}, \underline{e}_{D+2}, \cdots, \underline{e}_M >$ the noise subspace ($< \cdots >$ denotes a base of independent vectors).
This procedure extracting subspaces from the covariance matrix P is often called eigenvalue decomposition (EVD). An example will be used to clarify the EVD principle. If for example the number (see Figure 4.1) of antenna elements is three (corresponding with an array size of three), the correlation matrix R has a dimension of 3 x 3. Furthermore we have also three eigenvectors $\underline{e}_1, \underline{e}_2, \underline{e}_3$ and three eigenvalues $\gamma_1 > \gamma_2 > \gamma_3$. For sake of simplicity we consider two plane waves incident on the ULA coming from directions θ_1 and θ_2 which corresponds to a mode vector of $\underline{a}(\theta_1)$ and $\underline{a}(\theta_2)$ (see Figure 4.1). The two largest eigenvectors span the signal subspace with dimension two and the third one spans the noise subspace with dimension one.
Take a test mode vector $\underline{a}(\theta)$ and vary theta from 0 to 360 degrees to form a continuum. E_n is defined as $M \times M - D$ matrix whose columns are the $M - D$ noise eigenvectors. The Euclidean distance (squared) from a vector $\underline{Y}$ to the signal subspace is defined as $l^2 = \underline{Y}^H E_n E_n^H \underline{Y}$ (actually this is a dot product). So $1/l^2$ is plotted for points along the $\underline{a}(\theta)$ continuum as function of θ which gives us the MUSIC spectrum.

$$P_{MUSIC}(\theta) = \frac{1}{\underline{a}^H(\theta)E_n E_n^H \underline{a}(\theta)} \tag{4.3}$$

The problem solving of directions of arrival of multiple incident wavefronts consists of locating the intersections of the continuum with the range of A. Some problems may occur if there are two or more plane waves coming from different directions say $a(\theta_1) = a(\theta_2) = \cdots$ with $\theta_1 \neq \theta_2 \neq \cdots$, an insolvable situation occurs, called a type I ambiguity. This situation may occur when a plane wave incident at $\theta_1 = 30$ degrees and a plane wave coming at $\theta_2 = 330$ degrees. The cosine of 30 degrees or 330 degrees gives the same mode vector. Therefore no distinction can be made between these directions. For this reason the MUSIC will be plotted from 0 degrees to 180 degrees.

EVD is a method to obtain the two subspaces, in literature there are a lot of other methods to *estimate* subspaces see Vaccaro or Marple [8, 9].

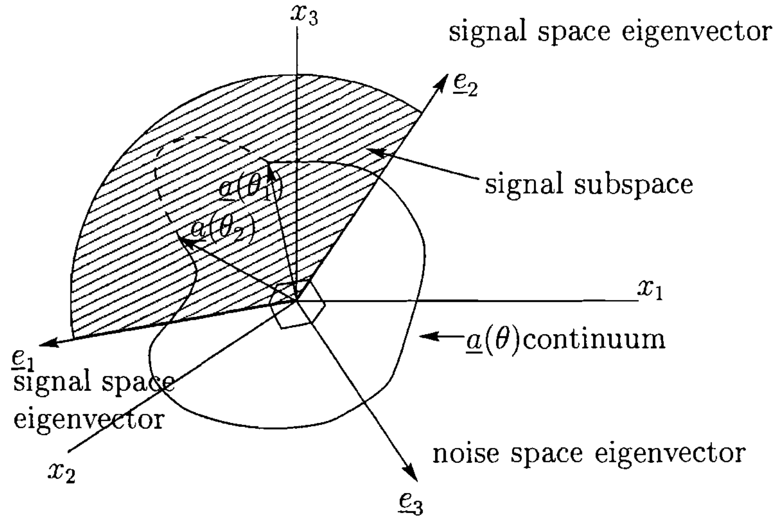

Figure 4.1: *Geometric description for three antennas.*

Once the AOA's of the D incident plane waves have been found, the A matrix becomes available and may be used to calculate the individual signal power of the incident plane waves. The solution for the P matrix is directly available from equation (4.2) as

$$P = \left(A^H A\right)^{-1} A^H (R - \sigma^2 I) A \left(A^H A\right)^{-1}. \tag{4.4}$$

Equation 4.4 can only be carried out if there are no coherent wavefronts w. This is another problem the $a(\theta)$ continuum may intersect the P dimensional signal subspace more than P times, another insolvable situation occurring only in the case of multiple incident waves, called a type II ambiguity. So suppose there are w out of D wavefronts which are coherent. The application of conventional eigenstructure technique will result in an *inconsistency*. When the number of signals detected will be $D - w + 1$ only $D - w$ directions-of-arrival, corresponding to the incoherent wavefronts, will be resolved. So if only one group of coherent signals exists the difference between the number of signals detected and the number of signals solved will be indicative of the size of the coherent group. So there are two ambiguities which have to be taken into account when interpreting the plots. To overcome the problems with coherent sources a technique will be introduced in the next section called spatial smoothing.

4.3 Spatial smoothing preprocessing scheme

The key to successful application of the eigenstructure technique is the non-singularity of the covariance matrix P. In this section a preprocessing scheme called spatial smoothing will be introduced that guarantees this property even when the signals are coherent.

In order to obtain the covariance matrix R we will have to find the probability distribution. Neither the probability distribution function of x nor any a priori knowledge about the second order statistics is assumed to be known. Therefore a large number of sample vectors $\underline{x}(\tau)$ for $\tau = 1, 2, \cdots, N$ (called snapshots) is provided. So an estimation of the correlation matrix R is often obtained by taking the time-average over the sample vectors

$$\hat{R} = A\left[\underline{x} \cdot \underline{x}^H\right] = \frac{1}{N}\sum_{\tau=1}^{N} \underline{x}(\tau)\, \underline{x}(\tau)^H \tag{4.5}$$

where A[•] stands for average[1].

In literature this is called the *forward only approach.* In recent studies the estimation of the correlation matrix as described before has been investigated. This straightforward averaging of the outer product of the snapshots does not to be suitable for coherent environments. If two or more sources are closely spaced MUSIC sees this as one source. We can also say that the signals arriving at the array are highly correlated. There are two approaches that endeavour to solve the singularity of the covariance matrix P which are *forward only smoothing approach (FS)* and *forward-backward smoothing approach (FBS)* see Vaccaro [8, p261]. These approaches will be explained following two sub-sections.

4.3.1 Forward smoothing

The output vector of τ^{th} observation period of L_1 elements can also described as

$$\underline{x}(\tau) = \begin{bmatrix} x_1(\tau) & x_2(\tau) & \cdots & x_{L_1}(\tau) \end{bmatrix}^T$$

. In spatial smoothing the array is subdivided into K smaller sub-arrays containing L_K sensors each with $K = L_1 - L_k + 1$. The output vector of the p^{th} sub-array is denoted by $\underline{x}_p(\tau)$ with the τ^{th} snapshot. The covariance matrix is then averaged to obtain the smoothed estimation R_{fs} (fs = forward smoothing).

$$R_{fs} = \frac{1}{K}\sum_{p=1}^{K} R_p^{fs} \qquad \text{where } R_p^{fs} = E\left[\underline{x}_p(\tau)\, \underline{x}_p^H(\tau)\right] \tag{4.6}$$

An estimation of the smoothed covariance matrix is

$$\hat{R}_{fs} = \frac{1}{K}\sum_{p=1}^{K} \hat{R}_p^{fs} \qquad \text{where } \hat{R}_p^{fs} = \frac{1}{N}\sum_{n=1}^{N} \underline{x}_p(\tau)\, \underline{x}_p^H(\tau) \tag{4.7}$$

or

$$\hat{R}_{fs} = \frac{1}{K}\sum_{p=1}^{K} \frac{1}{N}\sum_{n=1}^{N} \underline{x}_p(\tau)\, \underline{x}_p^H(\tau) \tag{4.8}$$

4.3.2 Forward-backward smoothing

To obtain a much better estimation of the covariance matrix *forward-backward smoothing (FBS)* approach can be used; the general FBS estimate is given by

$$R_{fbs} = \frac{R_{fs} + R_{bs}}{2} \qquad \text{where} \qquad R_{bs} = J \cdot R_{fs}^{*} \cdot J \tag{4.9}$$

---

[1] ∧ is used to denote estimates

An estimation of the forward backward smoothed covariance matrix is

$$\hat{R}_{fbs} = \frac{\hat{R}_{fs} + \hat{R}_{bs}}{2} \qquad \text{where} \qquad \hat{R}_{bs} = J \cdot \hat{R}^{*}_{fs} \cdot J \tag{4.10}$$

with

$$J = \begin{bmatrix} 0 & & 0 & & 1 \\ \vdots & & \vdots & & \vdots \\ 0 & \cdots & 1 & \cdots & 0 \\ \vdots & & \vdots & & \vdots \\ 1 & & 0 & & 0 \end{bmatrix}$$

called the reverse permutation matrix and $\hat{R}_{fs}$ as defined in (4.8).

4.3.3 Optimal sub-array size

With spatial smoothing we introduce a new parameter namely L_k the sub-array size. The sub-array size is not an arbitrary value as shown by Serebryakov [19]. There exists an optimal sub-array length L_{opt} described by Serebryakov as a trade off between decorrelating signals and the spatial resolution Δu which is formulated as follows

$$(\Delta u_{min})^6 = \frac{955.65}{L_k^5\, \nu\, (L_1 - L_K + 1)^2} \tag{4.11}$$

where $\Delta u = (2\pi \Delta x/\lambda)(cos(\theta_1) - cos(\theta_2))$ is the spatial resolution and ν is the signal to noise ratio. Minimising Δu, taking the derivative with L_k as variable, then the optimal sub-array size is given by

$$L_{opt} = \frac{5\,(L_1 + 1)}{7} \approx \frac{5L_1}{7} \tag{4.12}$$

Serebryakov suggested that if $L_k > L_{opt}$ we will have a good resolution (Δu is small) but a poor decorrelation of the signals and if $L_k < L_{opt}$ it will give a good decorrelation of the signals but a poor resolution. As a consequence the number of detectable waves D ($D = L_{opt} - 1$) will be less than in case the conventional eigenstructure is used ($D = M - 1$). Dimension of D is one less than L_{opt} if not there would be no noise subspace and MUSIC cannot be applied. So the number of detectable coherent wavefronts with spatial smoothing is equal to $D = L_{opt} - 1$. In the following section this spatial smoothing scheme will be illustrated by means of simulated data.

4.4 Simulated data

In order to check the MUSIC algorithm three plane waves incident on the ULA at 70, 80 and 120 degrees are considered as before. Noise is added in a random fashion with a Gaussian normal distribution having zero expectation μ and variance σ^2 (noise power). The number of antenna elements is 181 with an interspacing of 0.0052 m which gives a total aperture length of 0.94 m. Spatial smoothing which was discussed in the previous paragraph results in an optimal sub-array length L_k of 129 elements. Total number of sub-arrays K is equal to 53. For a good estimation of the covariance matrix R the number of snapshots is set to ten. Furthermore the amplitudes of the plane waves are set to 0.8, 1 and 1 V. The noise power σ^2 is 0.01 Watt which gives a signal-to-noise-ratio ν of 28.9432 dB. Running MUSIC with forward only smoothing and forward-backward smoothing methods give Figure 4.2. As we can see forward-backward smoothing gives a better estimation of the covariance matrix R which in turn gives steeper peaks in the MUSIC spectrum.

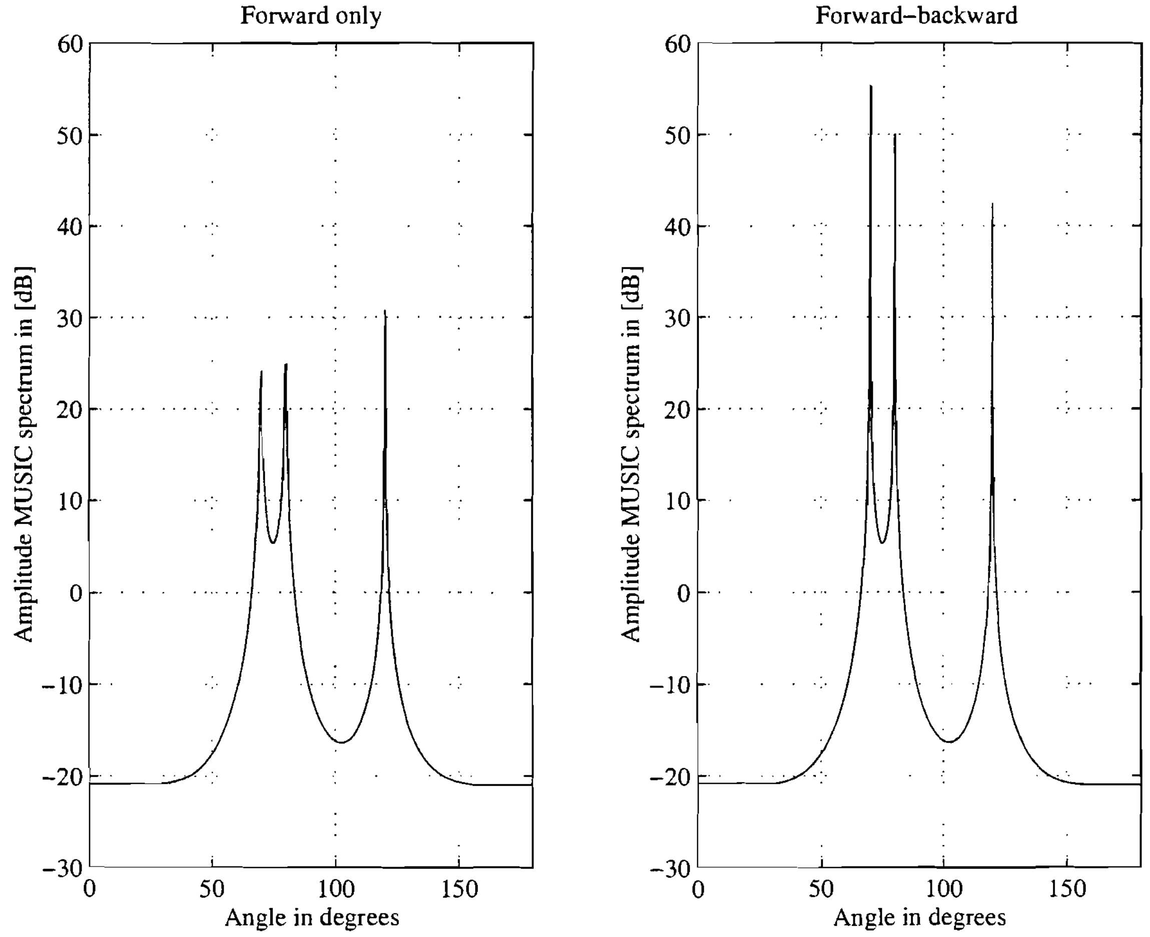

Figure 4.2: *MUSIC spectra with three plane waves incident on ULA at 70, 80 and 120 degrees using forward only smoothing and forward-backward smoothing approach (Number of snapshots is 10, ν = 27.2346 dB).*

In order to improve the MUSIC spectrum we have two parameters (ν and the number of snapshots) that can be varied. If the signal-to-noise-ratio is improved the volume of the noise subspace should become smaller and consequently the peaks in MUSIC become steeper which is depicted in (Figure 4.3). Another improvement can be effected when the number of snapshots is increased. Increasing the number of snapshots will give a better estimation of the covariance matrix R which in succession will give a better estimation of the signal subspace. In practice, however, the measure time is increased too, so a realistic number of snapshots has to be chosen in oder to reduce the measurement time. Figure 4.4

shows the results when the number of snapshots is increased. Once the MUSIC spectrum

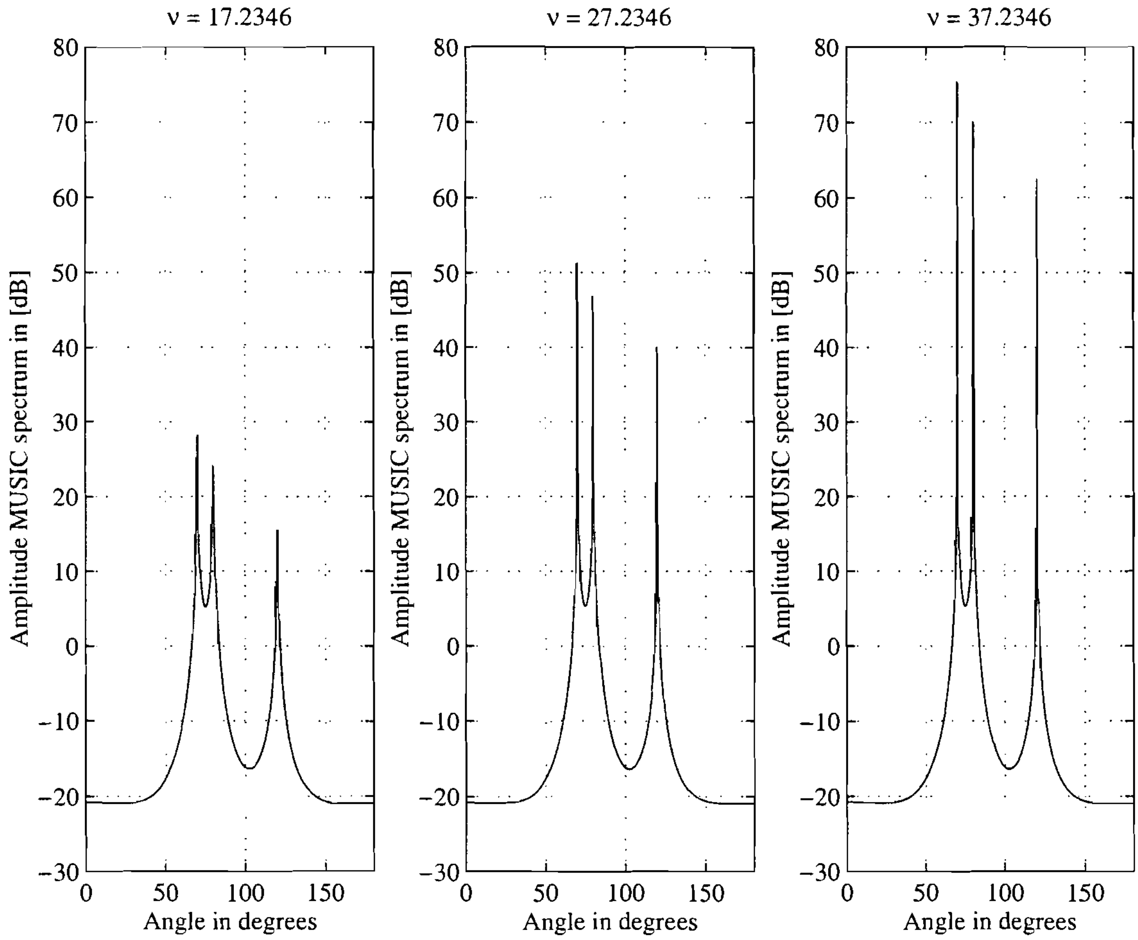

Figure 4.3: *MUSIC spectra for three incident plane waves with ν as parameter (ν showed in dB).*

becomes available (this is when the angles of arrival are also known) the signal covariance matrix P comes available too. The remaining part of the procedure is calculating the signal powers. To obtain the exact signal power is almost impossible because the noise power is not (always) available. Therefore (4.4) will be estimated which is done by means of neglecting the noise. If the signal-to-noise ratio becomes larger a better estimation of the matrix P should be obtained. So the signal covariance matrix P is estimated by

$$\hat{P} = \left(A^H A\right)^{-1} A\hat{R}A^H \left(A^H A\right)^{-1}. \tag{4.13}$$

In that case the estimation of the estimated covariance $\hat{R}$ is obtained by

$$\tilde{R} = A\hat{P}A^H \tag{4.14}$$

where $\sim$ denotes an estimation of an estimation.
The diagonals of $\hat{R}$ and $\tilde{R}$ represent the power received by each antenna element. If the estimated covariance matrix $\hat{R}$ and the estimation of the estimated covariance matrix $\tilde{R}$

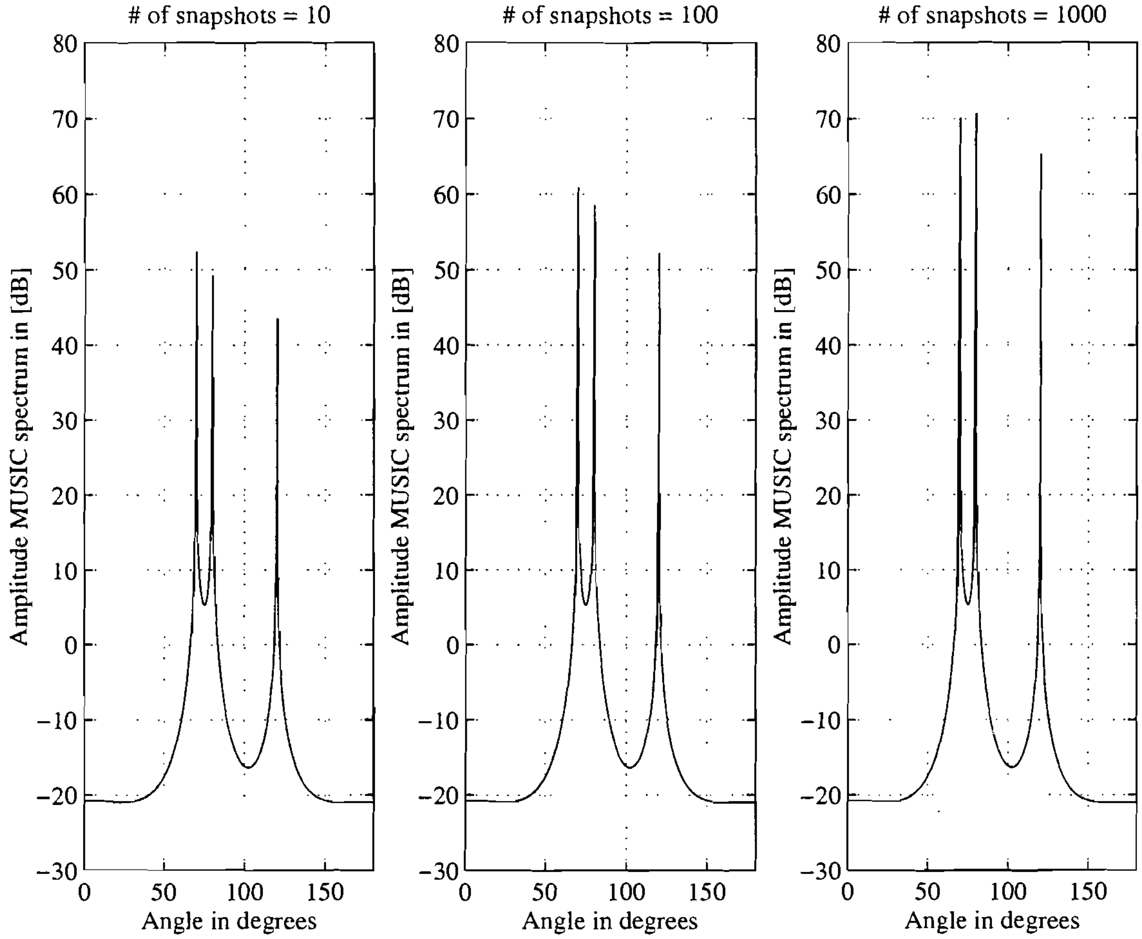

Figure 4.4: *MUSIC spectra for three incident plane waves with number of snap shots N as parameter.*

differ too much then the number of incident plane waves should have to be increased. This will give us a formal procedure to estimate the number of incident plane waves. First estimate the number of D plane waves on the ULA. Then perform MUSIC and compare the powers of $\hat{R}$ and $\tilde{R}$. If the power does not match start over again till the power will match. This procedure will be demonstrated in the following example with likewise three well defined plane waves.

In this example the same three plane waves which are mentioned before in the succeeding chapter on AOA with Fourier transform are considered i.e. plane waves coming from a direction at 70, 80 and 120 degrees. Suppose the amplitudes of the three incident plane waves are equal to $b_1 = 0.8$ V, $b_2 = 1.0$ V and $b_3 = 0.5$ V. If the number of estimated incident waves D is underestimated $(D < 3)$, we should expect an incorrect estimation of the amplitudes on the other hand if the number of estimated incident waves D is overestimated $(D > 3)$ the estimated amplitudes of the false responses $4, 5, \cdots, D$ should be very small. If D is exactly three the estimated amplitudes should be close to $b_1 = 0.8$ V, $b_2 = 1.0$ V and $b_3 = 0.5$ V. In Table 4.1 the estimated amplitudes are printed with their relative deviation. The following conclusions can be drawn: if real measured data are used

	$\hat{b}_1$ / Δ	$\hat{b}_2$ / Δ	$\hat{b}_3$ / Δ	$\hat{b}_4$ / Δ	$\hat{b}_5$ / Δ
D=2	1.1184 / 39.80%	0.4629 / 53.71%	D.n.a.	D.n.a.	D.n.a.
D=3	0.8002 / 00.25‰	1.0001 / 00.10‰	0.4998 / 00.40‰	D.n.a.	D.n.a.
D=4	0.8000 / 00.00‰	1.0000 / 00.00‰	0.5000 / 00.00‰	0.0006 / -	D.n.a.
D=5	0.8003 / 00.38‰	0.9999 / 00.10‰	0.4999 / 00.20‰	0.0008 / -	0.0000 / -

Table 4.1: *Estimated amplitudes and the relative error* Δ.

the best way to estimate the number of incident plane waves is an overestimation since the residual amplitudes are very small. Moreover if an overestimation is done the relative deviations become smaller than in the case when the exact number of plane waves D is chosen. When using these powers it is possible to reconstruct the signal power along the array (see Figure 4.5).

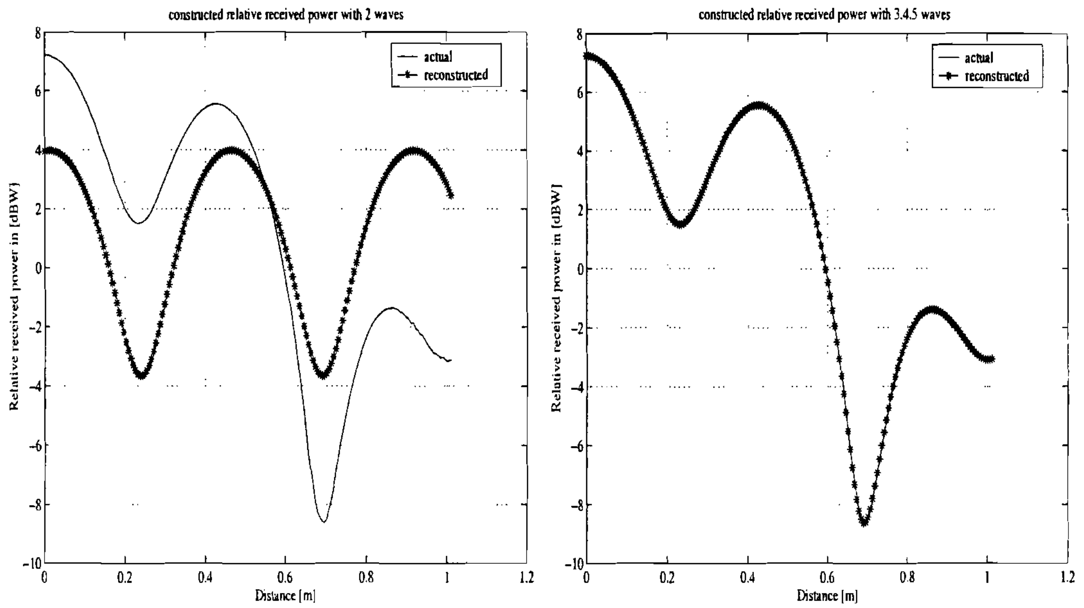

(a) estimated waves D=2

(b) estimated waves D=3,4,5

Figure 4.5: *Reconstructed received power from three incident waves at 70, 80 and 120 degrees.*

The main reason why we are applying MUSIC is to obtain a better spatial resolution in comparison with Fourier transform. (4.11) gives us the resolution in terms of spatial frequency. If we want to know the resolution as function of theta we have to differentiate $u_d = \frac{2\pi\Delta x\cos(\theta_d)}{\lambda}$ with respect to θ_d, this results in

$$|\Delta\theta_d| = \left|\frac{\Delta u_{d,min}}{\frac{2\pi\Delta x}{\lambda}\cdot\sin(\theta_d)}\right| \qquad \theta \in (0, 180). \tag{4.15}$$

According to (4.11) the spatial resolution is also dependent on the signal-to-noise ratio. In Figure 4.6 the spatial resolution is drawn for three signal-to-noise values

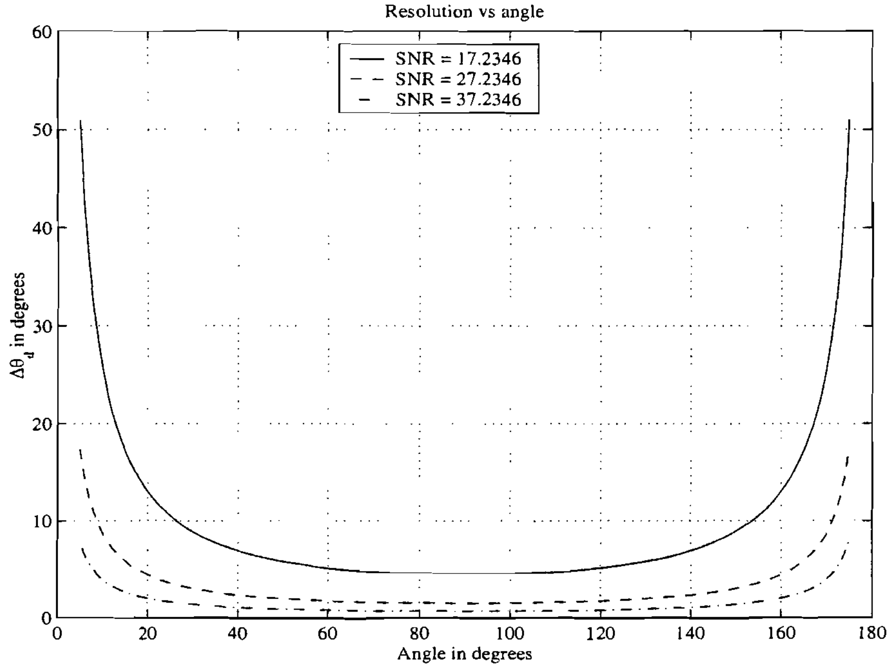

Figure 4.6: *Resolution of MUSIC vs. angle with ν as parameter (ν shown in dB).*

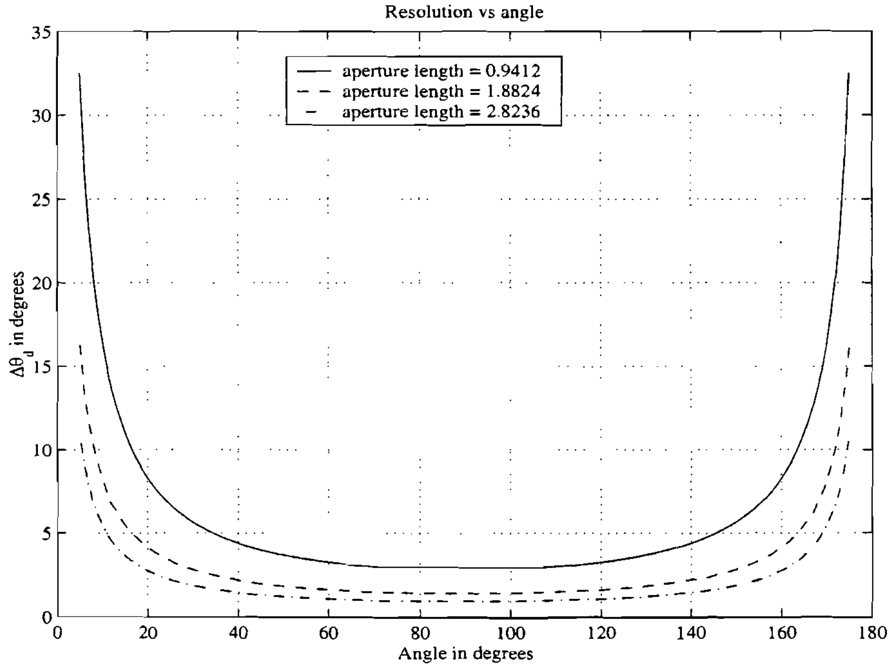

Figure 4.7: *Resolution vs. angle with aperture length as parameter (length showed in meters).*

with Δu fixed the resolution decreases if theta is getting near to 0° or 180°. An explanation for the reduction of the resolution near 0° and 180° is that the effective array size collapses.

At 90 degrees which is in our case perpendicular at the array axis the total array size is available, at 45 (or 135) degrees the effective array size is $\frac{1}{2}\sqrt{2}$ times the total array size. At 0 (or 180) degrees the effective array size becomes zero. So the detection of two plane waves at 5 and 10 degrees is not hardly possible. MUSIC will give a peak somewhere between 0 to 20 degrees. The figure 4.6 shows us if we want a high spatial resolution the signal-to-noise ratio should be as high as possible.
A different way of improving the resolution is enlarging the aperture length as illustrated in Figure 4.7. We will have to pay attention to the aperture length for if the length is too great the assumption about fixed plane wave composition along the array might not be satisfied. So extremely long aperture lengths have to be avoided. The latter is also true for the Fourier method.

4.5 Comparison of FT and MUSIC

In the preceding chapter and sections the performance of the Fourier method and MUSIC with respect to the AOA, ν and the aperture length were studied. In this section both methods will be compared with one another. With the Fourier transform and the MUSIC method information about direction-of-arrival is obtained. Both methods starts from the plane waves hypothesis.
The Fourier method depends strongly on the aperture length. In case of using a short aperture length the spatial resolution is very poor. This cannot be solved in varying the ν. Furthermore the estimated amplitudes deviate a lot from the actual amplitudes. A better estimation of the amplitudes cannot be done by means of enlarging the aperture length. Before we can apply the Fourier transform a windowing preprocessing scheme is needed. The Fourier transform is easy to implement in MATLAB.
Whereas the Fourier method depends strongly on the aperture length MUSIC depends very much on the non-singularity of the signal matrix P and it is less sensitive to the aperture length. If the signal matrix should become singular which means that coherent sources exist a preprocessing scheme called spatial smoothing will have to used to solve that problem. Using spatial smoothing a new variable is introduced: the optimal sub-array size. This optimal sub-array size is a trade off between the spatial resolution on the one hand and maximum decorrelation of the coherent signals on the other hand. The spatial resolution also depends on the aperture length which is 2.5 degrees in this case. Furthermore the ν affects the spatial resolution and should be as large as possible. The amplitudes are better estimated than when using the Fourier transform. A drawback of the MUSIC algorithm is the number of snapshots. If the number of snapshots is increased the duration of the measure time will increase too.

Our objective mentioned in the preceding chapter last section can now be achieved. The improvement of the spatial resolution has been effected. Compare Figures 3.4 and 4.7 then the improvement factor at $\theta = 90^\circ = \frac{20^\circ}{2.5^\circ} = 8$ which is at the same the maximum achievable spatial resolution. This is only valid when the signal-to-noise ratio ν is the same in both methods. Since MUSIC has a better performance for short aperture lengths compared with the Fourier method it will therefore be used as the tool in the following chapter on AOA spectrum measurements.

Chapter 5

Angle of arrival measurements

5.1 Introduction

In this chapter the MUSIC algorithm will be applied to measured data. As explained in chapter 2, frequency and space diversity correlation plots (based on powers) do not give us the desired information about the correlation the angle of arrival in the GSM bandwidth. Before MUSIC can be successfully applied several preconditions have to be fulfilled. Briefly these preconditions are: plane waves hypothesis, fixed plane wave composition along the aperture length and an acceptable signal-to-noise ratio ν. With the help of the MUSIC algorithm the AOA will be explored in order to draw a conclusion about antenna pattern diversity. Due to practical reasons the signal-to-noise ratio was estimated because the network analyzer gives only the signal power. The signal power is adjustable in a range of $[0, 30]$ dBm. We have to be aware of the fact that the transmitted power must not cause a power overflow at the receiving port of the network analyzer. This will result in permanent damage on the receiving port. The estimation of ν is done in section 5.2. A measurement description is given in section 5.3. The results of the measurements are discussed in section 5.4. In section 5.5 an antenna correlation is done in order to obtain the AOA correlation within a bandwidth. Furthermore in section 5.6 the distribution of the AOA in space is discussed. Section 5.7 discusses the considerations about the measurement set-up. Finally a conclusion is drawn in section 5.8.

5.2 Determination of the signal-to-noise-ratio

It was shown that the signal-to-noise ratio influences the spatial resolution of the MUSIC spectrum. For this reason ν should be as high as possible. The ν is estimated as follows. Consider the radio equation derived by Collin [3] once again which is

$$P_r = (1 - |S_{11}|^2) \cdot (1 - |S_{22}|^2) \cdot G_{T_x}(\theta, \phi) \cdot G_{R_x}(\theta, \phi) \cdot P_t \cdot \left(\frac{\lambda}{4\pi r}\right)^2 \qquad [\mathrm{W}]. \tag{5.1}$$

This equation can be rewritten where power is expressed in dBW as

$$P_r = P_t + G_{T_x} + G_{R_x} - L_{a,T_x} - L_{a,R_x} - L_{bf} \qquad [\mathrm{dBW}] \tag{5.2}$$

where $L_{a,T_x} = (1-|S_{11}|^2)$ and $L_{a,R_x} = (1-|S_{22}|^2)$ and $G_{T_x} = \max\{G_{T_x}(\vartheta,\varphi)\}$ respectively $G_{T_x} = \max\{G_{R_x}(\vartheta,\varphi)\}$ is called the antenna gain. L_{bf} stands for the free-space basic transmission loss and is defined as

$$L_{bf} = 20\log\left(\frac{4\pi r}{\lambda}\right) \qquad [\text{dB}]. \tag{5.3}$$

Moreover we can extend Equation (5.2) with medium losses $L_{m_{air}}$ and $L_{m_{cables}}$. In this case the air loss is negligible but the cable losses are certainly not. The SUCOFLEX 104PEA cables which are 9 meters long are used. They have an insertion loss (IL) of 2.3 dB at 900 MHz. Since we use two SUCOFLEX 104PEA cables our medium loss equals to $L_{m_{cables}} = 4.6$ dB. When using half wavelength dipoles the maximum gain is equal to 1.64 or 2.15 dB. Moreover the antennas are properly designed that the reflection losses can be negligible. Adjusting the source power to 25 dBm the received power at the receiving port of the network analyzer will be

$$\begin{aligned} P_r &= P_t + G_{T_x} + G_{R_x} - L_{a,T_x} - L_{a,R_x} - L_{m_{cables}} - L_{bf} \\ &= -5.0 + 2.15 + 2.15 - 0.0 - 0.0 - 4.6 - 49.59 \\ &= -54.89 \qquad [\text{dBW}]. \end{aligned} \tag{5.4}$$

What remains is to calculate the ν is the noise power, in the user's manual a typical average noise level of -77 dBm is given with regard to the bandwidth and an IF bandwidth of 3 kHz is used. Finally the signal-to-noise ν can be calculated which equals to

$$\nu = 10 * \log\left(\frac{3.2434 \times 10^{-3}}{10^{-7.7}}\right) \approx 52 \qquad [\text{dB}]. \tag{5.5}$$

Strictly speaking we should also define an overall system loss and subtract it form the 52 dB. In this report we will assume that the system loss is negligible.

5.3 Measurement description

The measurements took place in the restaurant of the building WAY at Philips research laboratory Eindhoven (PRLE), see Figure 5.2 or see Appendix D. Both the transmitting antenna and the receiving antenna are halfwave dipole antennas resonating at a frequency of 900 MHz and they are vertically polarized which results in an omni directional radiating patterns in azimuth direction. The height of the transmitting antenna and the receiving antenna is 2 meters above the concrete floor and they are separated 8 meters from one another. The transmitting antenna and receiving antenna are situated in the restaurant as depicted in Figure 5.2. If a measurement is in progress the location of the transmitting antenna will not change whereas the receiving antenna shifts through the xy-plane.
Two measurements were done in the xy-plane: one of them in the x-direction and the other in the y-direction. In order to cope with plane waves which do not lie in the xy-plane a third measurement was done in the z-direction (perpendicular to the xy-plane). For each measurement the number of snapshots is equal to ten which results in a total measure time of one hour and a quarter. Before the actual measurements were carried out, the GSM frequency band was observed with the help of a spectrum analyzer. It appeared that there was a lot of radio traffic in the GSM band. These man-made signals would disturb our measurements. As a matter of fact we could not turn down the GSM system in the

area of Eindhoven as this would cause a lot of commotion. Therefore the interference problem was solved by means of extending the (measurement) bandwidth to 200 MHz. This implies that the frequency range lies between 800 MHz and 1000 MHz. Once more with the help of a spectrum analyzer the 200 MHz bandwidth was observed. This was done to determine where the frequency spectrum is free from interference. These interjacent free frequency areas are 800 MHz - 890 MHz, 911 MHz - 933 MHz and from 961 MHz - 1000 MHz (see Figure 5.1). Unfortunately a small part of the R_x band is available and no single part of the T_x band is available. For the sake of completeness we are only interested in the correlation of of the AOA in a certain bandwidth. The frequency stepsize Δf equals

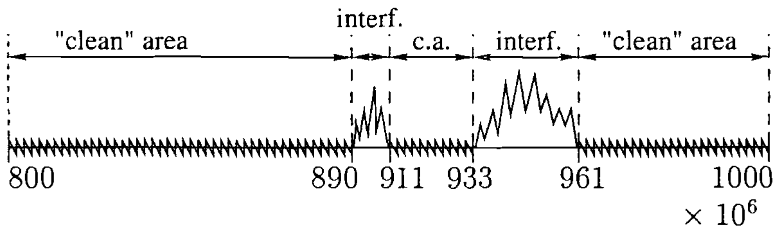

Figure 5.1: *Frequency spectrum of the extended bandwidth (frequency shown in Hz).*

to 125 kHz which corresponds to 1601 frequency components. In order to guarantee an acceptable spatial resolution, the x-side of the xy-table was used because this is the longest side. For the measurement in the y-direction the table was rotated counter-clockwise around its origin. In case of the measurement in the z-direction the table was placed vertically. Parameters for the xy-table were set as follows. The number of wavelengths in the x-direction is three because the total aperture length will exceed the x-dimension of xy-table if we would have used four or greater integers. The number of steps per wavelength is equal to 60 steps. This will result in a total number of $3 \times 60 + 1$ observation points which is at the same time the arraysize (plus one is needed for the 0^{th} step). These settings are a compromise between the peak-currents in the step-motors of the xy-table on the one hand and the spatial resolution on the other hand (see Equation (4.11)). Too small stepsizes in combination with high speed causes intolerable peak-currents through the step-motors. Therefore after a moment when the measurement is in progress the heat protection of the step-motors will be switched on and the measurement will be terminated. 181 observation points at a speed of 500 units (the valid range is 30 to 10,000 units) results in an acceptable resolution without interrupting the measurements. Having an array size of 181 the subarray size needed for the spatial smoothing preprocessing scheme equals to $\lfloor 129.2857 \rfloor$, where $\lfloor \bullet \rfloor$ denotes the largest integer smaller than the argument. Due to the preprocessing scheme the maximum number of detectable plane waves decreases and is equal to $D = 128$ instead of $D = 180$. Minus one is necessary to define a noise subspace with dimension one. If we would have used $D = 129$ then no noise subspace can be defined and the MUSIC algorithm fails. In the following sections the results of the measurements will be discussed.

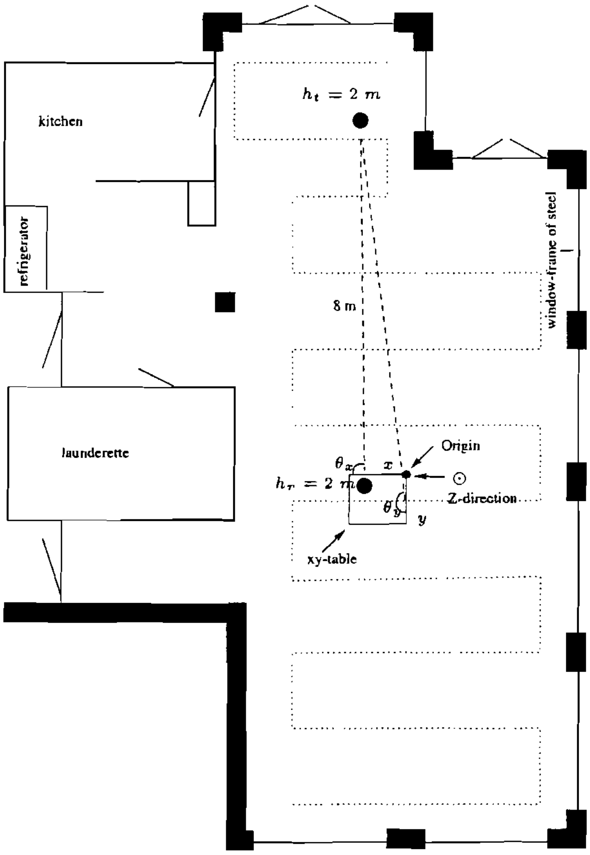

Figure 5.2: *Measurement environment description of the building WAY restaurant (dotted line represents the TL-armatures).*

5.4 Measurement results

5.4.1 X-direction

In the x-direction we can expect a dominant plane wave from approximately $\theta_x = 90$ degrees, corresponding to the line of sight (LOS). In order to judge if the AOA is strongly correlated in a bandwidth four frequency components were taken which were 880 MHz, 912 MHz, 933 MHz and 975 MHz. In order to obtain the AOA with MUSIC an overestimation has been done (see also preceeding chapter) and in this case it is eleven. Figure 5.3 and Figure 5.4 show the MUSIC spectrum at 880 MHz with an estimation of eleven plane waves and the reconstructed power respectively. The vertical bars in Figure 5.3 represent the power received by each individual MUSIC peak. In Appendix A the MUSIC spectra are shown for the frequencies mentioned before.

In order to check the plane wave hypothesis an extraordinary overestimation was done (for instance choose $D = 25$). As an outcome the MUSIC ought to be converged. If this is not the case it might be that spherical waves play a major part. When dealing with spherical waves MUSIC tries to decompose such a wave into plane waves. Theoretically speaking it would take infinite plane waves in order to decompose a spherical wave. In this case the MUSIC spectrum is converged after $D = 6$ was chosen and moreover the MUSIC spectrum had to be converged for all possible values greater than $D = 6$. Though the MUSIC spectrum has been converged when $D = 6$, the MUSIC spectrum will be better estimated when $D = 11$ is chosen. Apparently MUSIC needs more degrees of freedom in order to obtain a better estimation of the received powers. In examining Figure 5.3 and Figure 5.4, there are four plane waves found coming from a direction at 61.3, 80.1, 103.7 and 140.5 degrees. We do not know where these planes have originated (e.g from the floor, ceiling or TL armatures), therefore allocating a particular object from where the plane waves have been reflected is almost impossible. Fortunately we are only interested if the set of plane waves incident on ULA does not differ with increasing frequency. Therefore the individual powers are shown as function of theta for these different frequencies in Figure 5.5. Compare the set of planes waves at 880 MHz with the other sets of plane waves at different frequencies. These power components do not lie along a straight line at a particular angle due to irregularity during the measurements. Therefore the power components are clustered within a valid window of 10 degrees as denoted in Figure 5.5 with dashed lines. A provisional conclusion which can be drawn in the x-direction is that there are three dominant plane waves coming from a direction at ±60, ±,100 and ±140 degrees. The power components that lie below -50 dB are negligible because they have no significant contribution to the reconstructed power. Figure 5.5 shows that the AOA is strongly correlated over these four frequency points.

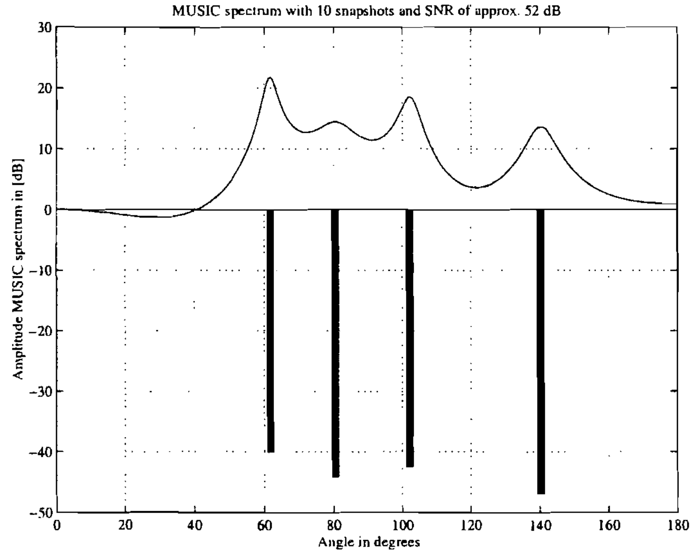

Figure 5.3: *AOA in the x-direction at a frequency of 880 MHz, the vertical bars represent the received power by each individual MUSIC peak in [dBW].*

In the following section the y-direction will be investigated in order to see if waves from this direction will behave likewise.

5.4.2 Y-direction

In the y-direction we can expect more plane waves coming from the right corresponding with $90 \leq \theta_y \leq 180$ degrees. During these measurements some people walked into the restaurant. Probably with their hand set in the stand by mode and therefore (local)

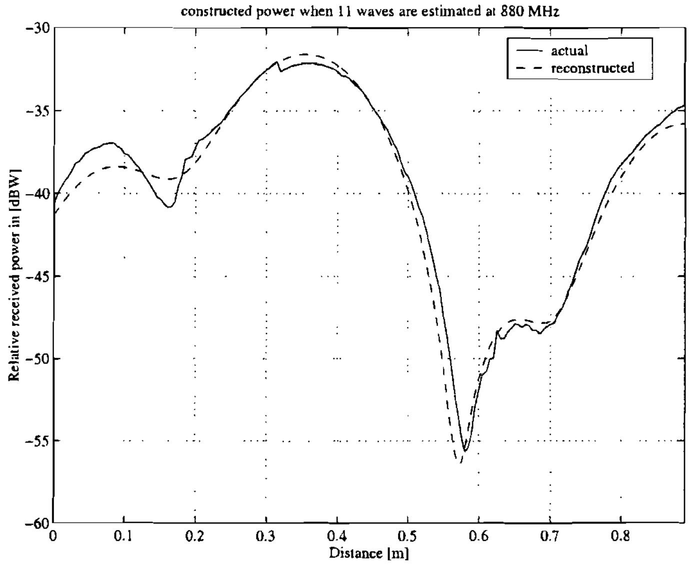

Figure 5.4: *Received power and reconstructed power in the x-direction at 880 MHz.*

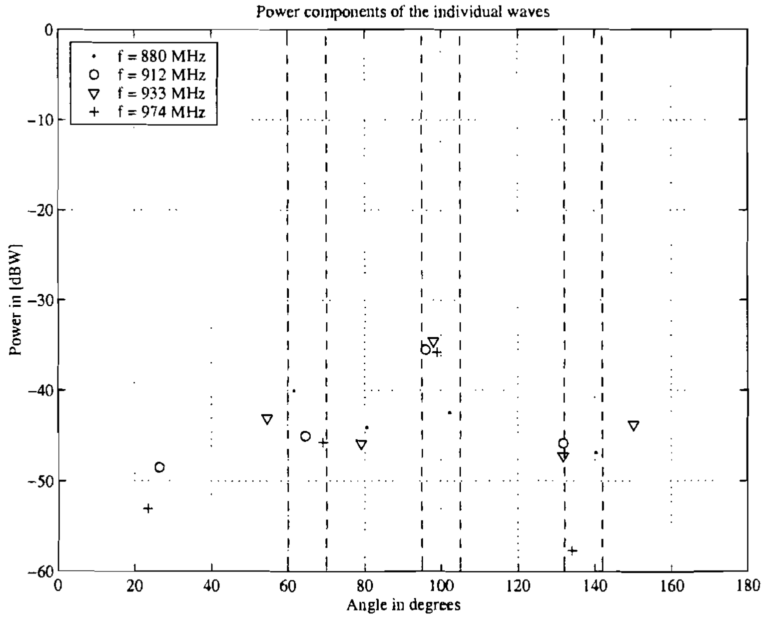

Figure 5.5: Received power for different frequencies.

additional interferences were integrated in the measurements. So in order to find the steady state might be a problem. Once again an extraordinary over-estimation was done to check if the MUSIC algorithm would become converged. At $D = 6$ the MUSIC algorithm has been converged. Also in this case when $D = 11$ the MUSIC spectrum is better estimated. As much as possible the same frequencies were used. Using 933 MHz did not give a converged MUSIC spectrum therefore 932 MHz was used which gave a converged MUSIC spectrum. The MUSIC spectrum of one frequency component is shown in Figure 5.6 and the reconstructed power in Figure 5.7 whereas the MUSIC spectra of the other frequencies are shown in Appendix A. On the right hand side MUSIC produces a greater amplitude estimation which came up to our expectation. In order to make a better comparison the individual received power at different frequencies are depicted in one plot see Figure 5.8 A window of 10 degrees was also used resulting in three dominant plane waves coming form a direction at ±65, ±100 and ±165 degrees. The results in the y-direction show that the AOA is strongly correlated over these four frequency points. Since the y-direction was rotated 90 degrees with respect to the x-direction we can expect a relation between the x-direction and y-direction. unfortunately this relationship is not a matter of course as will be explained in section 5.6.

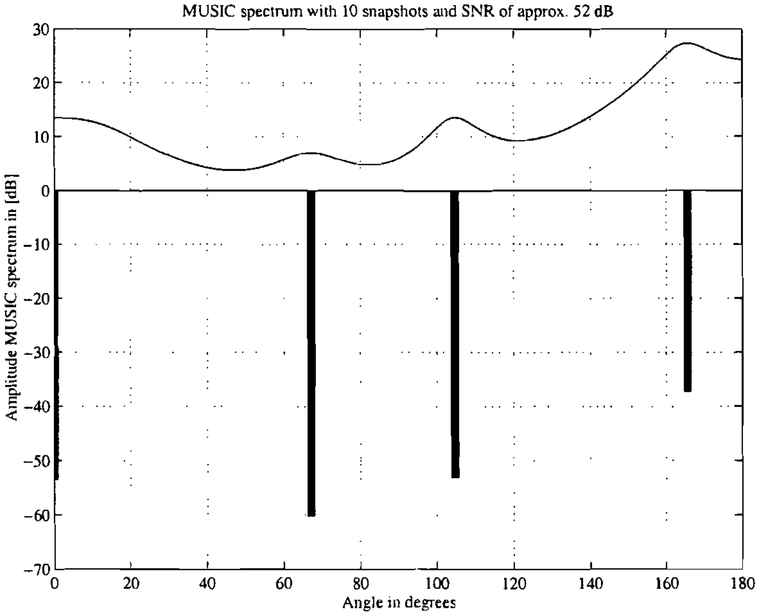

Figure 5.6: *AOA in the y-direction at a frequency of 880 MHz, the vertical bars represent the received power by each individual MUSIC peak in [dBW].*

5.4.3 Z-direction

In the x- and y-direction only plane waves are detected which lie in the xy-plane or horizontal plane. Plane waves travelling in the vertical plane are not detected. In order to detect these plane waves a third measurement will have to be performed. For the z-direction which is perpendicular to the xy-plane there was a problem during the measurement. The torque of the step-motor which controls the movable part of the x-side

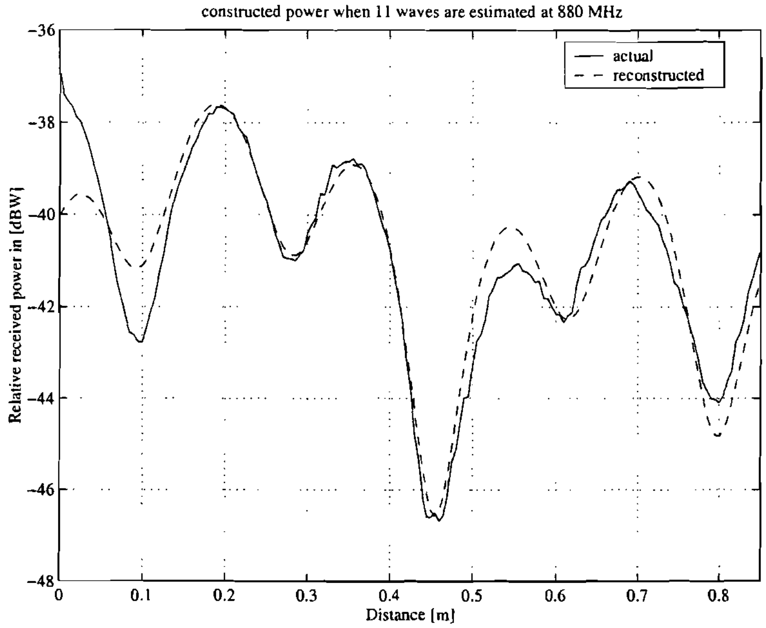

Figure 5.7: *Received power and reconstructed power in the y-direction at 880 MHz.*

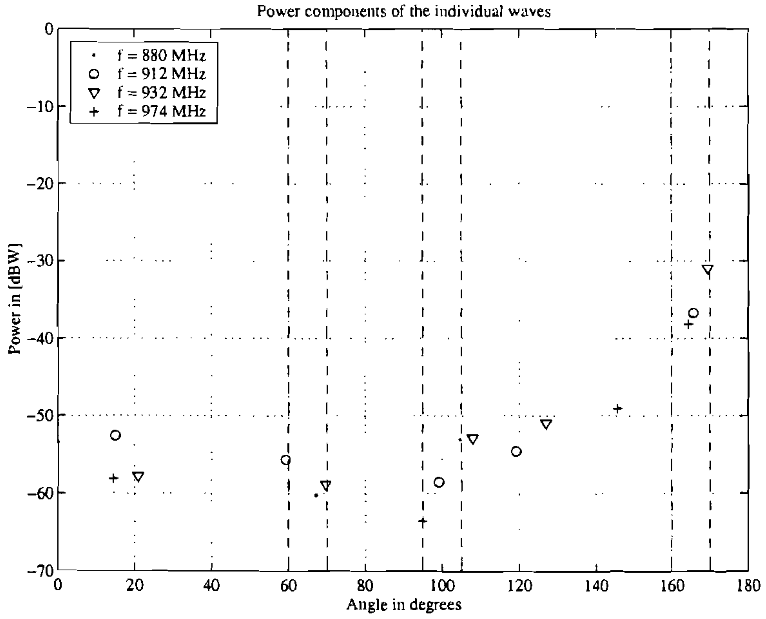

Figure 5.8: Received power for different frequencies.

is too slight to carry its own weight. Therefore the short dimension of the xy-table was used. This movable part of the short dimension is much lighter than the movable part of the longest dimension. Since the other side is shorter the number of wave lengths for this side will have to be smaller than 3 and is therefore equal to 2. This results in a total array size of 121 and a subarray size of 86 (the number of steps per wave length remains the same). Consequently the spatial resolution will be worse with a factor of 1.595 with respect to the spatial resolution in the longest dimension of the xy-table. This factor can be calculated with the help of Equation (4.11) and is

$$\begin{aligned}\frac{(\Delta U_{min_s})}{(\Delta U_{min_l})} &= \frac{L^5_{optm_l}\cdot(L_{1_l}-L_{k_l}+1)^2}{L^5_{optm_s}\cdot(L_{1_s}-L_{k_s}+1)^2}\\ &= \frac{(129)^5\cdot(181-129+1)^2}{(86)^5\cdot(121-86+1)^2}\\ &= \sqrt[6]{16.45} = 1.595\end{aligned} \tag{5.6}$$

where l denotes the longest dimension of the xy-table and s denotes the short dimension of the xy-table.

Equation (5.6) is only valid if the signal-to-noise ratio is the same on both sides. For instance if the spatial resolution in the longest side is approximately 2 [rad] then for the short side it gives a spatial resolution of 1.595 × 2 = 3.190 [rad]. Moreover the maximum of the detectable waves is merely $D = 85$.

After the problem with the xy-table had been solved MUSIC produced the following spectrum see Figure 5.9 and Figure 5.10 shows the reconstructed power. As we can see

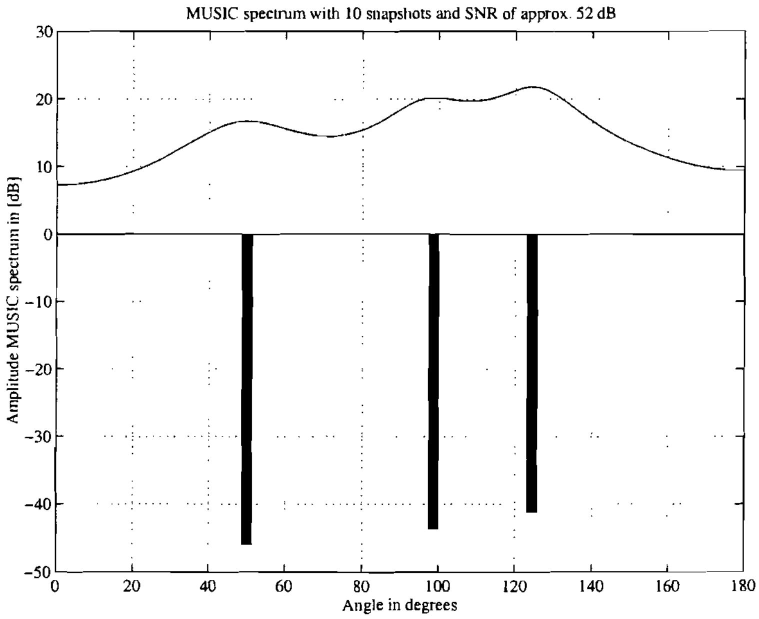

Figure 5.9: *AOA in the z-direction at a frequency of 880 MHz, the vertical bars represent the received power by each individual MUSIC peak in [dBW].*

in these figures the MUSIC spectrum is almost flat and the reconstructed power differs slightly. Comparison with the actual and reconstructed received power shows us that

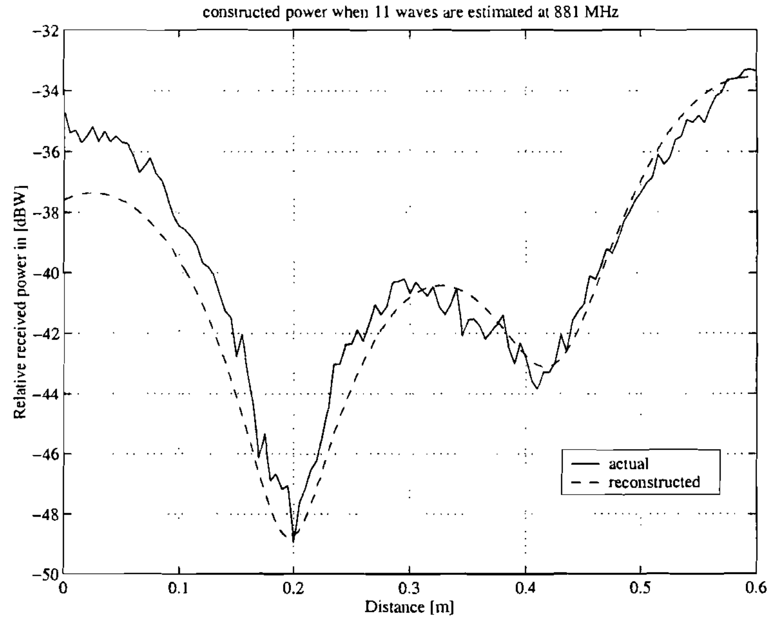

Figure 5.10: *Received power and reconstructed power in the* z*-direction at 881 MHz.*

the actual power contains a lot of fluctuations waves. It is not quite clear where these fluctuations come from. A possible explanation for this peculiarity is a bad connection between the receiving antenna and the network analyzer's receiving port or there might be standing waves between ground, ceilings and antennas.

As was mentioned before in this section we are only interested in the fact if there are plane waves travelling in the vertical plane. The MUSIC spectrum consists of three plane waves and the reconstructed power is partially matched with the actually received power. So there are certain waves travelling in the vertical plane. For the sake of completeness a second MUSIC spectrum at 914 MHz is shown in Figure 5.11 together with the reconstructed power see Figure 5.12.

Also in this case the actual received power exhibits many fluctuations. For this reason the received power plot for different frequency components is omitted. For measurement in the z-direction we can conclude that there are plane waves travelling in the vertical plane. Since the measured data of the z-direction are unreliable the data will not be used for further analysis.

Before a general conclusion will be drawn about the AOA, a more sophisticated exercition will be done in the following section.

5.5 AOA correlation

In order to explore if the AOA is correlated over more than four frequency components the same exercition can be carried out as performed in chapter 2 section 2.4 on correlation based on powers. Whereas the channel correlation plot did not give us the desired information about the AOA bandwidth, correlation plots based on AOA's should give us the right information. For the AOA correlation the data of the x-direction and the y-direction were

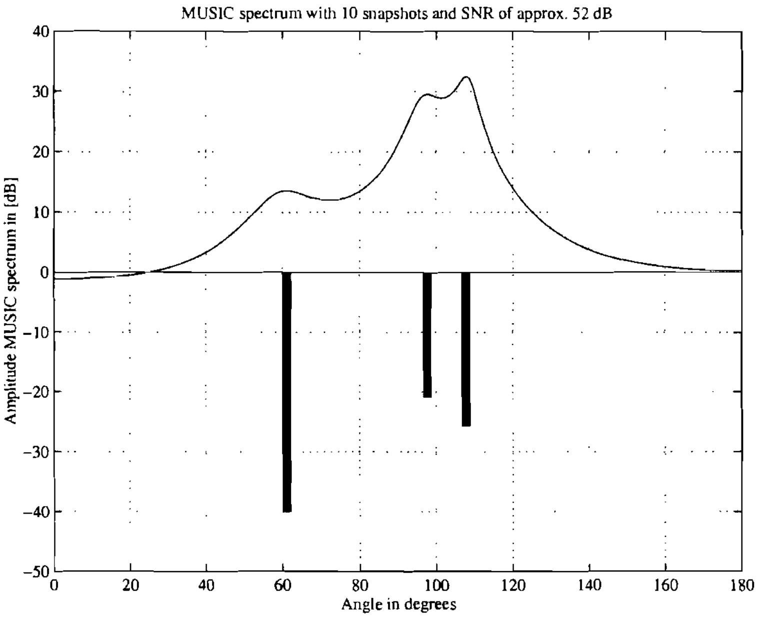

Figure 5.11: *AOA in the z-direction at a frequency of 914 MHz, the vertical bars represent the received power by each individual MUSIC peak in [dBW].*

Figure 5.12: *Received power and reconstructed power in the z-direction at 975 MHz.*

used. Furthermore the frequency range was changed from [800, 1000] MHz to [800, 880] MHz in order to avoid the disturbed frequency areas.
The measured data sequence is put in an $D \times F$ matrix where D is the total number of estimated angles of arrival and F the total number of frequency components. During the determination of the AOA for each frequency component the estimated AOA D remains constant and is equal to 11. Apply the correlation function in order to form the $F \times F$ correlation matrix with the same characteristics as mentioned in section 2.4.

$$\rho = \begin{bmatrix} \rho_{11} & \rho_{12} & \cdots & \rho_{1F} \\ \rho_{21} & \rho_{22} & \cdots & \rho_{2F} \\ \vdots & \vdots & \ddots & \vdots \\ \rho_{F1} & \rho_{F2} & \cdots & \rho_{FF} \end{bmatrix} \tag{5.7}$$

In order to interpret the correlation matrix in a comprehensible way the distribution is plotted against Δf or channel spacing. So ρ_{11} is a channel spacing of zero Hertz and occurs F times. A channel spacing of Δf is the same as ρ_{12} and occurs $2(F-1)$ times etc. etc. till a channel spacing of $(F-1) \cdot \Delta f$ is reached which occurs twice. Multiplication by two is needed because the correlation matrix is symmetrical along the main diagonal. The obtained AOA distribution is shown in Figure 5.13.
Studying this figure shows us that for the entire bandwidth (80 MHz) the distribution plot is flat. This implies that the AOA's are strongly correlated with all the frequencies.

Enlarging Figure 5.13a around 1 gives Figure 5.13b. On the edges of the distribution plot the correlation distribution plot will become less reliable for reasons mentioned in section 2.4. Nevertheless the distribution shows that the AOA is strongly correlated over the observed bandwidth. The same exercition was done for the y-direction which is shown in Figure 5.14. Also in the y-direction the AOA distribution plot shows that AOA has a broad frequency spectrum. If Figure 5.14a is enlarged around one it will result in Figure 5.14b and the correlation distribution will become less reliable on the edges, too.
We may conclude from this work so far that the AOA is strongly correlated over the GSM bandwidth. In this chapter it was not shown how wide the bandwidth of the AOA correlation actually was but for our purpose it was shown that within a bandwidth of 80 MHz the angles of arrival can be treated as independent on frequency.

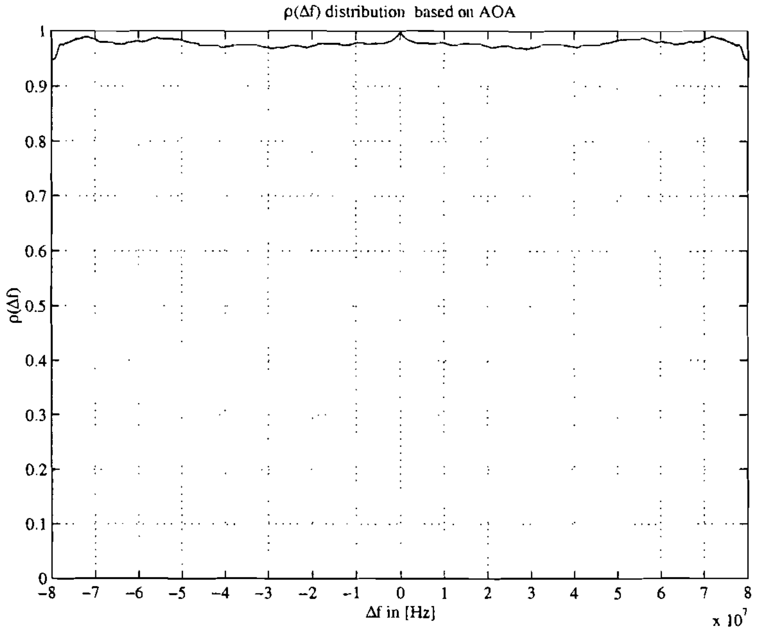

(a) normal view

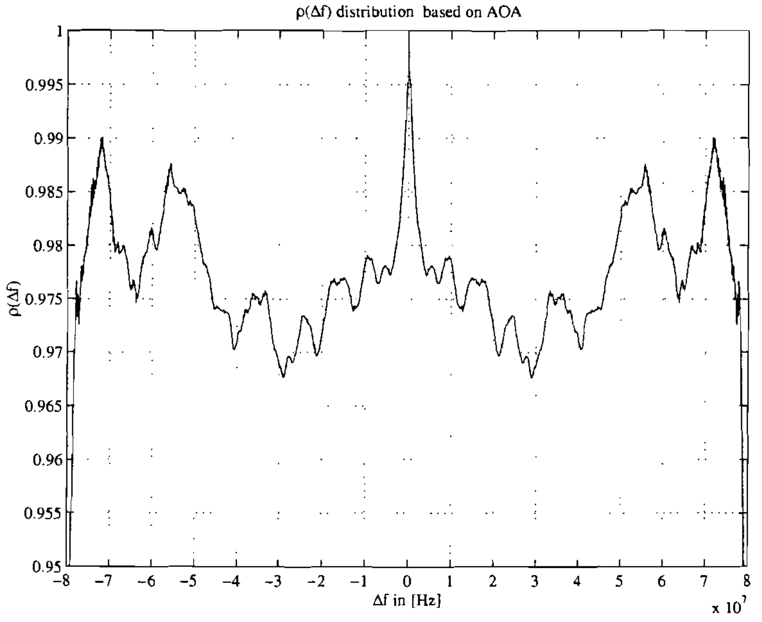

(b) enlarged view

Figure 5.13: $\rho(\Delta f)$ *angle of arrival correlation distribution in the* x*-direction.*

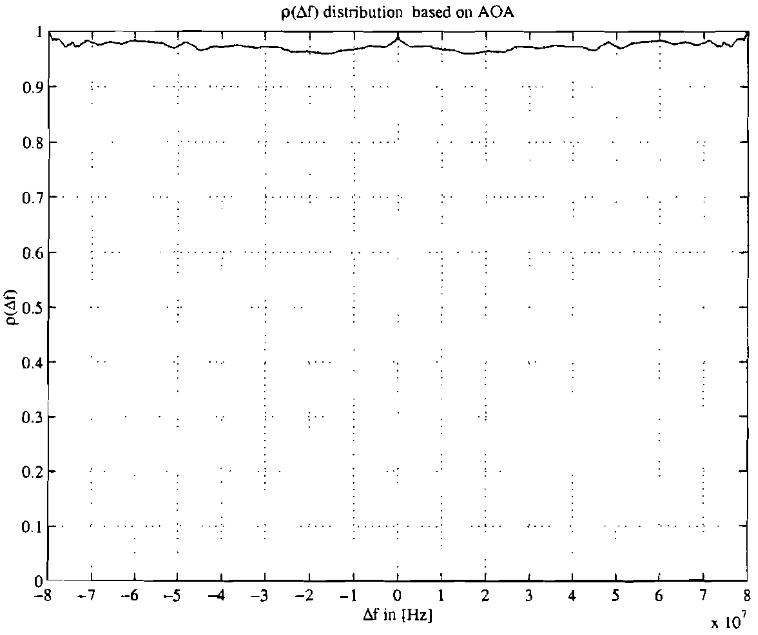

(a) normal view

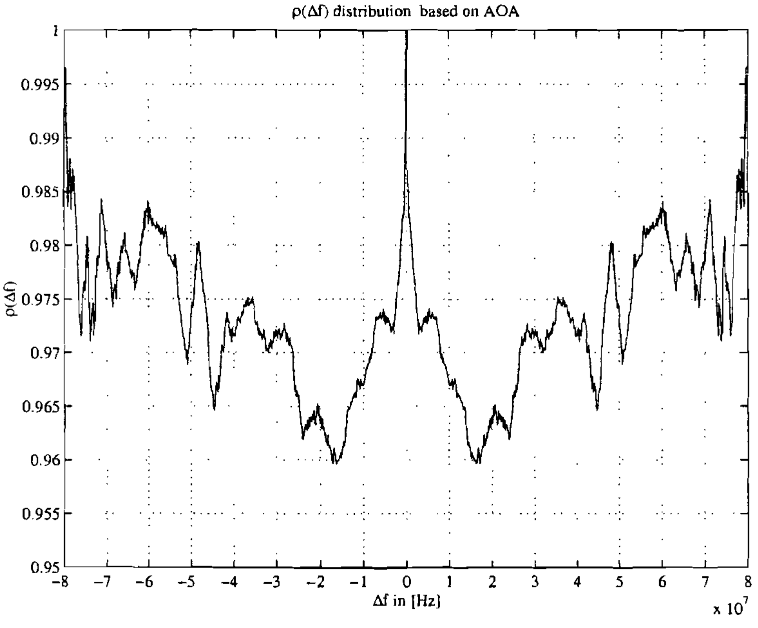

(b) enlarged view

Figure 5.14: $\rho(\Delta f)$ *angle of arrival correlation distribution in the* y*-direction.*

5.6 Distribution of the AOA

Once the AOA's are known we can submit the AOA's to further investigation. The AOA distribution plays an important part in the following chapter on dual antenna system. Before the AOA distribution will be discussed, we will first look how MUSIC builds up its spectrum.

5.6.1 Definition of angles

Consider the 3-dimensional coordinate system and use the spherical coordinates (r, φ, ϑ) to denote a point in space. These angles are called azimuth φ and elevation ϑ respectively (see Figure 5.15). When the ULA is positioned on the x-axis we can define simular angles with respect to the ULA. These angles are denoted by azimuth ϕ and elevation θ as depicted in Figure 5.15. These definition of angles is needed to understand how MUSIC will build up its spectrum.

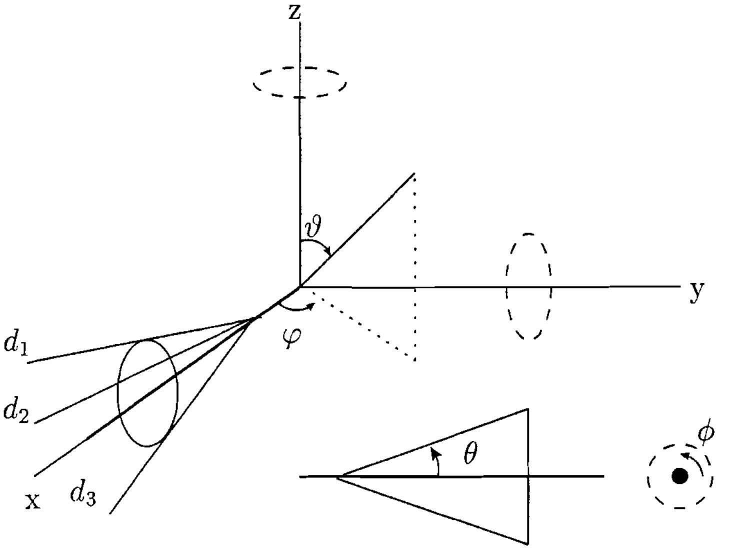

Figure 5.15: Definition of angles and angles which are not detected but have certainly a contribution to the MUSIC spectrum.

5.6.2 Angles mapped into the MUSIC spectrum

With the current implemented MUSIC algorithm only information about elevation angles with respect to the ULA can be obtained. So no explicit information about the azimuth angles with respect to the ULA is obtained. As matter of facts these azimuth angles play a significant part in the MUSIC spectrum. With the help of Figure 5.15 it will be made clear how these azimuth angles will contribute to the MUSIC spectrum. In this example three plane waves coming from a direction having the same elevation θ angles are used but with different azimuth ϕ angles. These plane waves are denoted by d_1, d_2 and d_3. The total energy received by each antenna element consists of the summation of the individual energy of the plane waves. As a consequence MUSIC "interprets" this as *one* plane wave coming from a direction θ whereas actually there are three plane waves incident on the

ULA. So azimuth angles which lie on the cone (see Figure 5.15) cannot be detected. If we also want to have information about the azimuth angles a two dimensional MUSIC algorithm is necessary.
As a matter of fact we are more interested in the azimuth φ and elevation ϑ angles with respect to the origin. This information can indirectly be obtained by studying Figure 5.15 once more. In the x-direction information about the elevation angle is obtained at a fixed azimuth angle $\varphi = 0$ degrees. In case the y-direction is used information about the elevation angle at a fixed azimuth angle $\varphi = 90$ degrees. In the z-direction information about the azimuth angle φ is obtained. Furthermore we could say that the angles found in the x-direction are also found in the y-direction but then rotated 90 degrees. As we read in the preceeding chapter 4 on AOA with MUSIC algorithm the effective arraysize becomes zero at 0 and 180 degrees. Therefore plane waves travelling parallel to the array are not detected. So angles which we have detected in the y-direction need not be detected in the x-direction. The opposite is also true, in the x-direction it is also possible to detect new angles which are not detected in the y-direction. Consequently it is not a matter of course to conclude that the relation between the x-direction and y-direction is merely 90 degrees. In accordance with the MUSIC spectra the AOA distribution is certainly not uniform although the measurements were taking place in an indoor environment. Additional measurements can be carried out in order to obtain a more accurate estimation of the AOA distribution. In the following chapter on dual antenna system AOA distribution will be described in more detail.

5.7 Considerations about the measurement set-up

An important precondition is the plane wave hypothesis which must be fulfilled across the entire xy-table. Since the xy-table is large compared with the physical dimension of the GSM hand-set this plane wave hypothesis counts heavily. Therefore the measurements are done in the restaurant of the WAY building which is large compared to the xy-table. When the room is made smaller and smaller then the plane wave hypothesis will not be fulfilled across the entire xy-table. We will have to bear in mind, however, that the plane wave hypothesis is not fulfilled across the entire xy-table but it will be fulfilled for the mobile handset due to its small size. So for small rooms or small indoor environments the current measurement set-up is not suitable.
The antennas used in the measurement set-up are halfwave dipole antennas. If vertically polarized the radiation patterns are omni-directional and only dependent on ϑ. As mentioned before MUSIC maps all plane waves which arrive at a cone (see Figure 5.15). This is only true when isotropic antennas are used. When using "real" antennas the cone ought to be multiplied by the radiation pattern of the antennas which will result in a deformation of the cone. In this case the halfwave dipoles are used which means plane waves coming from a direction $\pm\theta = 90$ degrees are not detected.

5.8 Conclusions

The first two measurements in the x-direction and in the y-direction give the best results. On the other hand the z-direction measurement is less successful but it is not a matter of course that this measurement is not useful. In the z-direction information about plane waves is obtained which does not lie in the xy-plane. It was also shown the AOA can be considered independent of the frequency within a bandwidth of 80 MHz. The actually correlation bandwidth was not determined since this was not our purpose.

Antenna pattern diversity, as is explained in chapter 2 is the basis from which we started, can therefore be applied. So if during reception several dominant plane waves coming from different directions arrive at the antennas of the handset a radiation pattern will be selected which mutes several destructive interferences. Assuming that destructive interference is present otherwise no action will be taken. After a fixed time interval the handset transmits information into free space with the same radiation pattern causing less or no destructive interference at the basestation antennas. All things considered the transmit power can be less than when no optimal pattern is used. This implies that the battery life time is increased.

Another important conclusion deals with the distribution of the AOA. In the x and y-direction (indirectly) information about the elevation angle is obtained whereas in the z-direction (indirect) information about the azimuth angle is obtained. The exact distribution is not known because the MUSIC algorithm implemented in this form can not be used to extract the elevation and azimuth angles. So the AOA's distribution can only be approximated. Since the measurements took place in an indoor environment we can expect a uniform distribution. According to the MUSIC spectra the uniformity of the AOA does not hold good here. In the next chapter on dual antenna system these AOA distribution plays a prominent part.

Chapter 6

Dual antenna system

6.1 Introduction

In the preceding chapter it was shown that the AOA can be considered constant within frequency bandwidth of 80 MHz. So far we have not discussed about the possibility of altering the far field radiation patterns of the handheld. In this chapter we will describe a dual antenna system which consists of vertically polarized half wavelength dipole antennas having an antenna interspacing of one tenth of a wavelength. Generally speaking more than two antennas can also be used. Since the antennas have to be implemented on or integrated in a GSM handheld the number of antennas is restricted to the physical size of the GSM handheld. In this case the mutual coupling between the closely spaced antennas should be paid more attention to. The coupling with the surrounding environment will not be discussed here because it does not fit in the graduation project.
In literature several diversity techniques are described, mainly dealing with switching between multiple antennas. The antenna interspacing is chosen in such a way that the mutual coupling can be neglected. These diversity techniques which are often used are recapitulated below.

- **Selection**. The output of one antenna is observed. At a given moment the signal level drops below a predetermined threshold. The switcher switches to the output of the other antenna. If both antennas receive poor signal levels the switcher will not switch again to avoid frequent switching between the antennas. Formula form as follows $S_{sel}(t) = \max\{S_1(t), S_2(t)\}$.

- **Maximum ratio combining**. With this technique the signals received from the individual antennas are added in such a way that the addition is at its maximum value. This means that the output of each antenna is weighted by a complex coefficient. A major problem is determining the optimum weighting coefficients. This problem can be avoided by using discrete steps which result in sub-optimum weighting coefficients. Formula form as follows $S_{mrc}(t) = \max\{|S_1'(t) + S_2'(t)|\}$ where the single quote denotes the weighted signal.

- **Equal gain combining.** An equal gain combiner is obtained when unit gains are used in the maximum ratio combiner. For both the equal gain combiner and the maximum ratio combiner the signals must first be co-phased. Implementing such a co-phase circuit in hardware causes problems. Formula form as follows $S_{egc}(t) = \frac{S_1(t)+S_2(t)}{\sqrt{2}}$.

As mentioned before these diversity techniques work very well if the antenna interspacing is large enough in which case the mutual coupling is negligible. If two antennas are closely spaced we might expect that the received signals are quite correlated. Note that the antenna interspacing is expressed in terms of wavelengths. So in case of low frequency corresponding with a large wavelength the antenna interspacing is also large. But speaking in terms of wavelengths, this is still called closely spaced.

In case of two antennas, if one antenna is positioned so close to the other antenna that the diversity techniques which were mentioned before do not work very well. For instance if the selection technique will be used in combination with two closely spaced antennas then switching will not make any sense due to the strong correlation between these received signals.

In order to make use of the mutual coupling a different diversity technique will be used. This technique is called *antenna diversity using switched parasitic elements* and it is based on antenna pattern diversity. When placing a parasitic antenna in the vicinity of the primary antenna the results will be that the far field pattern of the antenna system will alter compared to the far field radiation pattern when a single primary antenna is used. This appears from the fact that due to the mutual coupling a current distribution will be induced along the parasitic antenna. Generally speaking the parasitic antenna behaves like a secondary source. Suppose we would have one primary antenna and two parasitic antennas then there would be 2^2 different antenna configurations which result in different far field radiation patterns. This technique works quite well if the correlation coefficient between these far field patterns is low. Since the physical dimension of the GSM handset is relatively small compared to the wavelength only one parasitic antenna at fixed distance from the primary antenna will be used. In order to obtain decorrelated radiation patterns the parasitic antenna will be terminated with an impedance.

In section 6.2 an analytical approach is derived and a numerical approach is used to generate different radiation patterns. In section 6.3 these radiation patterns are used to obtain an antenna correlation. A conclusion is drawn in section 6.4.

6.2 Derivation of far field radiation patterns

In this section we will start our calculations with an electrical dipole situated in the origin and carrying a current I pointing in the z-direction. After the far field components of the electrical dipole antenna are given, the far field components of two closely spaced dipole antennas will be derived. Also a numerical simulation tool will be used to simulate the same antenna configuration. Ultimately a comparison will be made between the analytical approach and the numerical approach.

In order to derive these field components some assumptions have been made:

- far field approximation $r \gg \frac{2L_a}{\lambda}$(Fraunhofer region [1]), where L_a is the largest physical linear dimension of the antenna.

- cross section wire $d \ll \lambda$ and
- antenna system is placed in free space.

The electrical field components in spherical coordinates can be written as

$$\underline{E}(\underline{r}) = E_r(\underline{r})\underline{e}_r + E_\vartheta(\underline{r})\underline{e}_\vartheta + E_\varphi(\underline{r})\underline{e}_\varphi \tag{6.1}$$

where $(\underline{e}_r, \underline{e}_\vartheta, \underline{e}_\varphi)$ is the orthonormal basis and $\underline{r} = \{r, \vartheta, \varphi\}$.

Each component, such as E_r, is a complex function of the form $E_r = E_{rr} + \jmath E_{ri}$ where E_{rr} is the real part and E_{ri} is the imaginary part. Usually the field is time varying, in this report only sinusoidal time varying fields are used. So the physical electrical field is obtained by multiplying (6.1) by $e^{\jmath\omega t}$ and taking the real part of it, that is

$$\underline{E}(\underline{r}, t) = \Re e\left\{\underline{E}(\underline{r}) \cdot e^{\jmath\omega t}\right\} \tag{6.2}$$

which gives

$$\underline{E}_r(\underline{r}, t) = E_{rr}(\underline{r}) \cdot \cos(\omega t) - E_{ri} \cdot \sin(\omega t) \tag{6.3}$$

for the r component of the physical field. In this report we will deal with complex numbers unless otherwise specified.

Suppose an electrical dipole with element length Δz carrying a current

$$\underline{I} = \delta(x)\delta(y)\left[U(z + \frac{\Delta z}{2}) - U(z - \frac{\Delta z}{2})\right] I\underline{e}_z$$

(I is the current through the wire element) is placed in the origin and parallel with the z-axis. The electrical and magnetic field components are [1].

$$\begin{aligned}
E_r(\underline{r}, t) &= \frac{-\jmath I \Delta z Z_0 \cos(\vartheta)}{2\pi\beta} \cdot \left[\frac{\jmath\beta}{r^2} + \frac{1}{r^3}\right] \cdot e^{\jmath(\omega t - \beta r)} && (6.4)\\
E_\vartheta(\underline{r}, t) &= \frac{\jmath I \Delta z Z_0 \sin(\vartheta)}{4\pi\beta} \cdot \left[\frac{\beta^2}{r} - \frac{\jmath\beta}{r^2} - \frac{1}{r^3}\right] \cdot e^{\jmath(\omega t - \beta r)} && (6.5)\\
E_\varphi(\underline{r}, t) &= 0 && (6.6)\\
H_r(\underline{r}, t) &= 0 && (6.7)\\
H_\vartheta(\underline{r}, t) &= 0 && (6.8)\\
H_\varphi(\underline{r}, t) &= \frac{I \Delta z \sin(\vartheta)}{4\pi} \cdot \left[\frac{\jmath\beta}{r} + \frac{1}{r^2}\right] \cdot e^{\jmath(\omega t - \beta r)} && (6.9)
\end{aligned}$$

Assume there is an observation point in the far field zone the terms with r^{-2} and r^{-3} are very small compared to r^{-1} terms and can therefore be negligible. Then (6.4) to (6.9) reduce to:

$$\begin{aligned}
E_r(\underline{r}, t) &= 0 && (6.10)\\
E_\vartheta(\underline{r}, t) &= \frac{\jmath\beta I \Delta z Z_0 \sin(\vartheta)}{4\pi r} \cdot e^{\jmath(\omega t - \beta r)} && (6.11)\\
E_\varphi(\underline{r}, t) &= 0 && (6.12)\\
H_r(\underline{r}, t) &= 0 && (6.13)\\
H_\vartheta(\underline{r}, t) &= 0 && (6.14)\\
H_\varphi(\underline{r}, t) &= \frac{\jmath\beta I \Delta z \sin(\vartheta)}{4\pi r} \cdot e^{\jmath(\omega t - \beta r)} && (6.15)
\end{aligned}$$

where $\beta = \frac{2\pi}{\lambda}$ [rad m^{-1}] wave number in free space and $Z_0 = 120\pi$ [Ω] free space wave impedance.

6.2.1 Linear antenna

Suppose we have a piece of iron wire having a total length L and its centre being placed in the origin of the coordinate system. This piece of wire represents a linear antenna. The total far field radiation pattern is obtained as follows. Divide the wire into Q segments Δz of equal length. Each segment represents an electrical dipole where the far field components are known. The total far field of Q segments is just an addition of Q electrical dipoles and is

$$E_{\vartheta_{tot}} = \sum_{q=1}^{Q} \frac{j\beta Z_0 I(q\Delta z)\sin(\vartheta)}{4\pi r'_q} \cdot e^{-j\beta r'_q}\Delta z. \tag{6.16}$$

Taking the limit of Δz to zero gives

$$\begin{aligned} E_{\vartheta_{tot}}(\underline{r}') &= \lim_{\Delta z \to 0} \sum_{n=1}^{Q} \frac{j\beta Z_0 I(q\Delta z)\sin(\vartheta)}{4\pi r'_q} \cdot e^{-j\beta r'_q}\Delta z \\ &= \frac{j\beta Z_o \sin(\vartheta)}{4\pi} \cdot \int_L \frac{I(z)}{r'} \cdot e^{-j\beta r'} dz \end{aligned} \tag{6.17}$$

where r' is the distance from the source point to the field point whilst the time dependence is omitted and $I(z)$ the current distribution along the wire.
In figure 6.1 the far field approximation gives $r' \approx r$ but not in the argument of the complex e power because this is an oscillating term. Therefore in the far field approximation phase differences can certainly occur. Applying the far field approximation to (6.17) then we obtain

$$E_{\vartheta_{tot}}(\underline{r}) = \frac{j\beta Z_0 \sin(\vartheta)}{4\pi r} \cdot e^{-j\beta r} \cdot \int_L I(z) \cdot e^{-j\beta z\cos(\vartheta)} dz \tag{6.18}$$

6.2.2 Two closely spaced dipoles

Assume a single linear antenna is placed in the origin of the coordinate system and excitated with a voltage source placed in the centre of the antenna. Due to the voltage source, the current is not uniformly distributed but it is a function of z with $I_1(z = -\frac{L}{2}) = I_1(z = \frac{L}{2}) = 0$. Let us take another linear antenna and place this antenna at a distance d from the first antenna see Figure 6.1. The second antenna can be terminated with an impedance Z_ℓ. For this configuration the total radiated field will differ in comparison with one linear antenna because the mutual coupling will induce a current distribution I_2 along the second antenna which affects the total radiated field. Compare this with a transformer or a coupled circuit. The more antennas are added the more the radiation field will be affected. So the total far field can be calculated by

$$\begin{aligned} E_{\vartheta_{tot}}(\underline{r}_1', \underline{r}_2') = &\frac{j\beta Z_0 \sin(\vartheta)}{4\pi r_1'} \cdot \int_L I_1(z) e^{-j\beta r'_1} dz \\ &+ \frac{j\beta Z_0 \sin(\vartheta)}{4\pi r'_2} \cdot \int_L I_2(z) e^{-j\beta r'_2} dz \end{aligned} \tag{6.19}$$

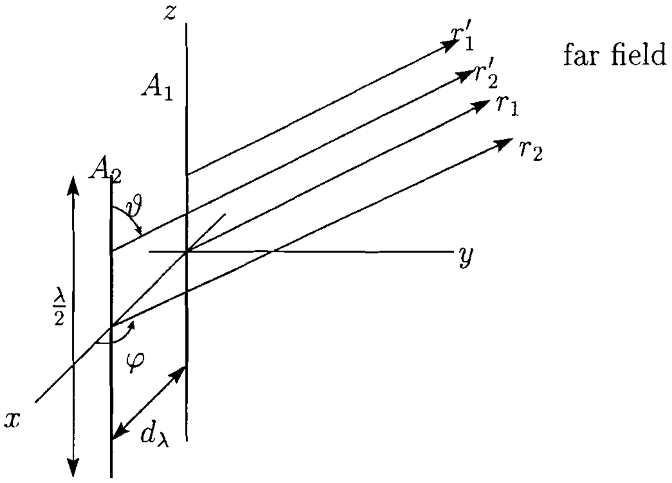

Figure 6.1: *Two closely spaced dipoles (For far field approximation).*

where

$$
\begin{aligned}
\underline{r}' &= \begin{pmatrix} \sin(\vartheta)\cos(\varphi) \\ \sin(\vartheta)\sin(\varphi) \\ \cos(\vartheta) \end{pmatrix} \\
\underline{r}'' &= \begin{pmatrix} \sin(\vartheta)\cos(\pi-\varphi) \\ \sin(\vartheta)\sin(\pi-\varphi) \\ \cos(\vartheta) \end{pmatrix} \\
\underline{d} &= \begin{pmatrix} d_x \\ 0 \\ 0 \end{pmatrix} \\
\underline{z} &= \begin{pmatrix} 0 \\ 0 \\ z \end{pmatrix} \\
(\underline{z},\underline{r}') &= z\cos(\vartheta) \\
(\underline{d},\underline{r}'') &= -d\sin(\vartheta)\cos(\varphi) \\
r_1' &= r_1 - (\underline{z},\underline{r}') \\
r_2' &= r_1 + (\underline{d},\underline{r}'') - (\underline{z},\underline{r}'')
\end{aligned}
\tag{6.20}
$$

where $(\bullet,\bullet)$ stands for the dot product operator of two vectors. Substituting r_1' and r_2' from (6.20) in (6.19) and in the far field $r_1' \approx r_2' \approx r$ gives

$$
\begin{aligned}
E_{\vartheta_{tot}}(\underline{r}) = \frac{j\beta Z_0 \sin(\vartheta)}{4\pi r} . e^{j\beta r} \cdot \Bigg(& \int_L I_1(z) e^{-j\beta z\cos(\vartheta)} dz \\
& + e^{-j\beta d \sin(\vartheta)\cos(\varphi)} \int_L I_2(z) e^{-j\beta z \cos(\vartheta)} dz \Bigg)
\end{aligned}
\tag{6.21}
$$

Consider the two closely spaced dipoles as a two port (see Figure 6.2) where the second antenna can be terminated with an impedance Z_ℓ. Mathematically speaking this is a 2×2 matrix (generally speaking if we had used M antennas we should have had an $M \times M$ matrix or M-port system) as follows:

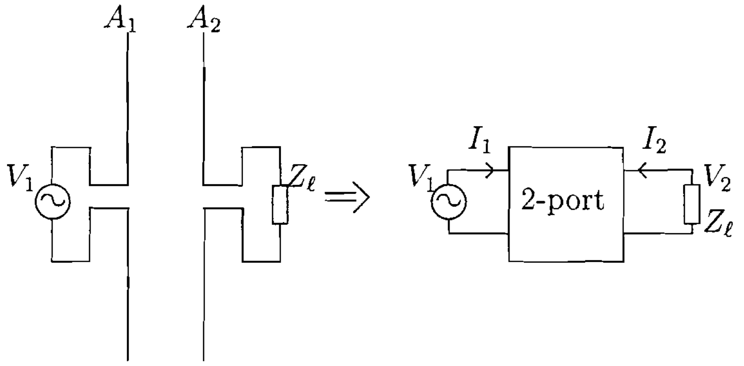

Figure 6.2: *Two port approximation of two closely spaced dipoles.*

$$\begin{bmatrix} V_1 \\ V_2 \end{bmatrix} = \begin{bmatrix} Z_{11} & Z_{12} \\ Z_{21} & Z_{22} \end{bmatrix} \cdot \begin{bmatrix} I_1 \\ I_2 \end{bmatrix} \quad \text{or} \quad \underline{V} = A \cdot \underline{I} \tag{6.22}$$

where Z_{21}, Z_{12} is the mutual impedance and is usually written as Z_m and

$$Z_{11} = \left.\frac{V_1}{I_1}\right|_{I_2=0} \quad \text{and} \quad Z_{22} = \left.\frac{V_2}{I_2}\right|_{I_1=0}$$

is usually written as Z_s, s denoting selfimpedance.
If the two antennas are identical then $Z_{11} = Z_{22} = Z_s$ and $Z_{21} = Z_{12} = Z_m$. (6.22) can be rewritten and will become

$$\begin{aligned} Z_{1_{in}} &= \frac{V_1}{I_1} = Z_s + Z_s\frac{I_2}{I_1} \\ -Z_{2_{in}} &= \frac{V_2}{I_2} = Z_m\frac{I_1}{I_2} + Z_s \end{aligned} \tag{6.23}$$

where $Z_{1_{in}}$ and $Z_{2_{in}}$ are input impedances of the two port. If the port two is terminated with Z_ℓ then current I_2 can be expressed in terms of current I_1.

$$I_2 = \frac{-Z_m}{Z_{22} + Z_\ell} \cdot I_1 = c \cdot I_1 \tag{6.24}$$

Furthermore the current distribution along the antenna A_1 is assumed to be real valued and sinusoidal and the length of the antennas is an odd number of $\frac{\lambda}{2}$ long. Therefore for Z_m and Z_s the formulas from Kraus [4] can be substituted in equation (6.24) and are repeated below.

$$\begin{aligned} Z_s &= 30 \cdot \Big(0.557 + \ln(2\pi n) - Ci(2\pi n) + j \cdot Si(2\pi n)\Big) \\ Z_m &= 30 \cdot \Big(2Ci(\beta d_x) - Ci(\beta(\sqrt{d_x^2 + L^2} + L)) - Ci(\beta(\sqrt{d_x^2 + L^2} - L)) \\ &\quad - j \cdot 2Si(\beta d_x) - Si(\beta(\sqrt{d_x^2 + L^2} + L)) - Si(\beta(\sqrt{d_x^2 + L^2} - L))\Big) \end{aligned} \tag{6.25}$$

where
$n = 1, 3, 5, \ldots,$
Ci, cosine integral,

Si, sine integral and
0.557 Euler's constant.

For the sake of convenience the mutual impedance is drawn in Figure 6.3 and showing us that in proportion as the distance decreases the mutual impedance increases. Since in this case we are dealing with a distance along the d_x which is expressed in terms of wavelengths we can also write d_x as d_λ. In other words the coupling between these antennas becomes stronger and stronger. When the distance between the antennas is one tenth of a wave length the mutual coupling is very strong and certainly not negligible. (6.19) can be simplified in a compact form as follows

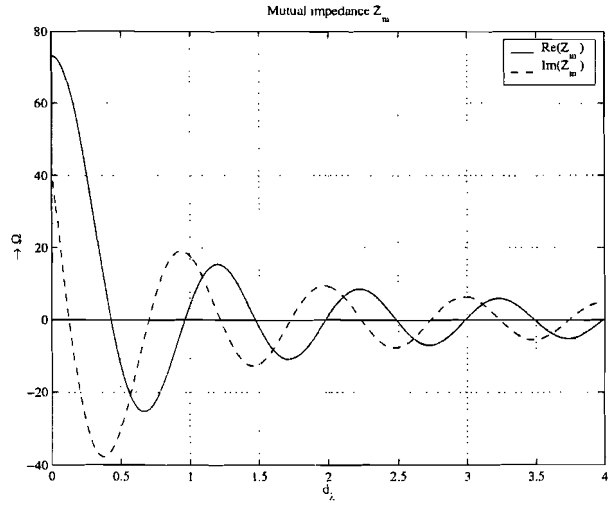

Figure 6.3: *Mutual impedance as function of the distance between the dipole antennas.*

$$E_\vartheta(\underline{r}) = E_0(\underline{r}) \cdot \left(1 + c \cdot e^{-j\beta d \sin(\vartheta)\cos(\varphi)}\right) \tag{6.26}$$

where

$$E_o(\underline{r}) = \frac{j\beta Z_0 \sin(\vartheta)}{4\pi r} \cdot e^{j\beta r} \cdot \int_L I_1(z) \cdot e^{-j\beta z \cos(\vartheta)} dz$$

is called the elementary radiation pattern of one linear dipole.

In Figure 6.4 the E_ϑ component is drawn as function of the solid angle Ω with the antenna interspacing d as parameter and the second antenna terminated with $Z_\ell = 0\,\Omega$. If the impedance from antenna A_2 is changed, the current distribution along this antenna will change and as a result the total far E-field will change too. In this dipole example the current distribution along antenna one is purely real and sinusoidal. In practice, however, these current distributions may not have a sinusoidal shape. Although this is quite a good model to calculate the antenna configuration assuming that the current distribution is known beforehand. We can calculate the current distribution in an analytical way and substitute these values into the previous equations which will result in very complicated equations. Numerical tools such as numerical eletromagnetics code (NEC) can be used to calculate the current distribution and substitute these current values in the previous

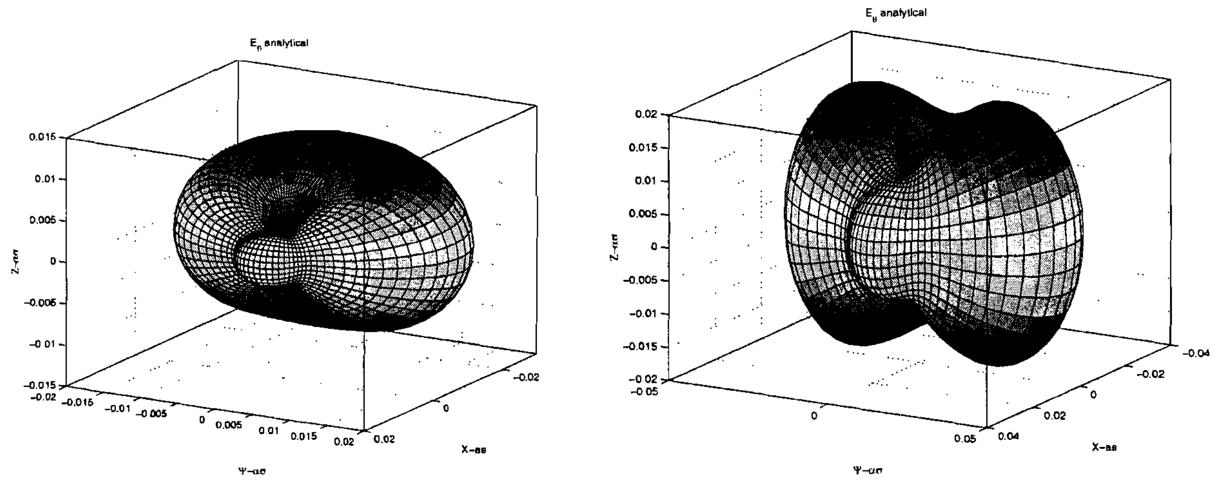

(a) $d_\lambda = 0.1$

(b) $d_\lambda = 0.5$

Figure 6.4: *Far E-field for two distances at a frequency f=900 MHz and* $Z_\ell = 0\ \Omega$.

equations. But if the geometry of the antennas should become more complicated the analytical approach will become unsuitable for this purpose. From this point of view the analytical approach will be exchanged with NEC. In order to verify the NEC results the same antenna configuration is made in NEC. Moreover NEC itself has its own restrictions such as accuracy and oscillations as explained in the following sub-section.

6.2.3 NEC results

When using NEC some preconditions will have to be checked in order to obtain reliable data from NEC simulations. For the sake of convenience the symbolism will be maintained as used in the user's guide of NEC. Beyond this sub-section the symbols lose there meaning. The linear antenna is subdivided into segments of length Δ relative to the wavelength λ and should lie within

$$0.001 \leq \frac{\Delta}{\lambda} \leq 0.1\,.$$

Further on the wire has an finite radius d, also relative to λ and is limited by the approximations used in the kernel of the electric field integral equation. NEC uses two approximations, the thin-wire kernel and the extended thin-wire kernel which is explained in Burke & Poggio [7]. The NEC 'USER'S GUIDE' advises to keep

$$\frac{2\pi d}{\lambda} \ll 1$$

or as suggested in the NEC user's manual

$$0 < d < 0.01\lambda$$

At last the accuracy of the numerical solution depends on $\frac{\Delta}{d}$. Small values of $\frac{\Delta}{d}$ may result in extraneous oscillations in the computed current near free wire ends, voltage sources, or lumped loads. Use of the extended thin-wire approximation will allow a smaller value of $\frac{\Delta}{d}$ than would be permissible with the normal thin-wire kernel. Studies of the computed fields on a segment due to its own current have shown that for an accuracy of less than 1%, that

$$\frac{\Delta}{d} > 8, \quad \text{for thin-wire kernel and}$$

$$\frac{\Delta}{d} > 2, \quad \text{for extended thin-wire kernel.}$$

In the two port model a frequency of 900 MHz is used which corresponds to a wavelength of one third of a meter. The number of segments used to divide the wire(s) is 25 with an antenna length of $\frac{\lambda}{2}$ which gives a segment length Δ of 0.00666 [m]. The wire radius d is 0.00025 [m] (specification from a "real" wire). The data to describe an antenna and its environment and to request computations of antenna characteristics are input by means of "punched cards". The data card for two closely spaced dipoles is shown below (as an illustration).

```
CM 2 closely spaced dipoles, Half wavelength antenna
CM By   :  P.Mattheijssen
CE Date :  10-11-1999
GW  1  25       0.     0.  -0.0833       0.  0.  0.0833  2.5E-04
GW  2  25  0.0333     0.  -0.0833   0.0333  0.  0.0833  2.5E-04
GE  0
LD  4   2      13     13  1.0E-20  1.0E-20
FR  0   1       0      0    900.0       1.
EX  0   1      13     00      1.0
RP  0  37      73   0010       0.       0.  5.      5.
EN
```

The first data-card deck which is read (from the top to the bottom) is the comment card CM to specify the run or simulation, further on the CM cannot be omitted since it must always occur. The third card denotes the comment end card CE and terminates the comments so a CE card must always occur in a data-card deck and may be preceded by as many CM cards as are needed to describe the run. Successively the wire geometry is punched, for a convenient input of structure geometry data, several data-cards options are provided to generate data for groups of segments or patches. In this case the geometry wire GW is used for two closely spaced dipoles. The structure is ended by geometry end GE data card. After the geometry has been read the load structure LD is punched to load the structure. The FR data card specifies the desired frequency which can sweep through a certain frequency band (the number of sweep points is limited). The next data-card is the excitation card EX which can be a voltage source or a current element. Finally the RP card tells NEC to calculated the radiation pattern as function of the solid angle Ω. Ultimately the EN card will be used to indicate to NEC the end of all execution and must always be applied. Two NEC simulations were done to obtain the far field radiation patterns for two different antenna spacings. The results are to be found in Figure 6.5.

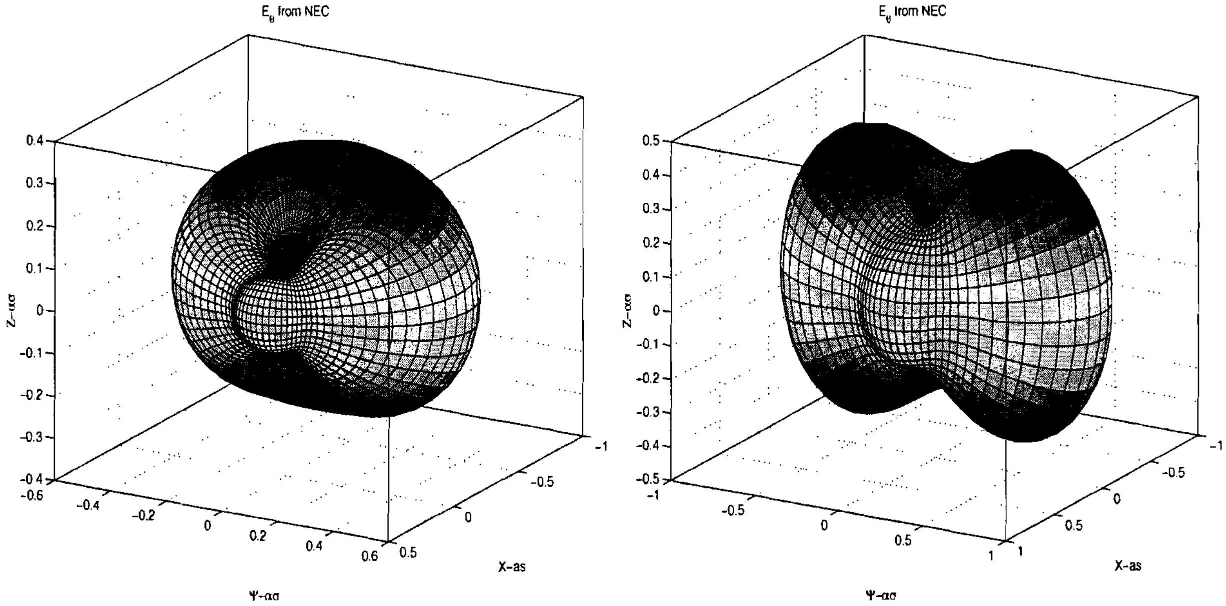

(a) $d_\lambda = 0.1$ (b) $d_\lambda = 0.5$

Figure 6.5: *Far E-field for two distances at a frequency f=900 MHz and* $Z_\ell = 0\,\Omega$ *with NEC.*

6.2.4 Comparison of NEC with the analytical model

Let us compare the NEC far E-fields (Figure 6.5 with the analytical far E-fields (Figure 6.4 and we might conclude that the shapes are the same apart from the scale. This tells us that results from NEC are reliable. In case we want to known the antenna input impedance the current distributions along the wires will have to be known. The following three Figures 6.6, 6.7 and 6.8 depicts the current distributions from NEC for different loads and the following three Figures 6.9, 6.10 and 6.11 are the analytical current distributions. In case $Z_\ell = 10^6\Omega$ this corresponds to an open circuit at the second antenna terminals, the current at the terminals is zero as expected. Whereas NEC produces the good answer the analytical approach fails and even in the two other cases the analytical approach fails. An explanation for this inconsistency is that NEC uses a voltage source as excitation whereas the analytical approach uses impressed currents. Furthermore the self impedance and the mutual impedance are elaborated with purely real valued sinusoidal current distributions. In the analytical model the top values of the current is taken from NEC in order to make the comparison more reliable. A possible solution for this problem is to take the currents from NEC and substitute these currents in the analytical formulas. But doing so the calculation time increases rapidly especially if the correlation coefficients have to be calculated and are therefore omitted. If other (more complex) structures are used the complexity forces us to transfer from analytical to numerical tools. As to the dipoles, the conclusion to be drawn would be as follows: Two closely spaced dipoles where one is used as a parasitic antenna produces an asymmetrical radiation patterns and to calculate these asymmetrical radiation patterns it would be more convenient or preferable to use numerical tools. Terminating the parasitic antenna with different loads would result in different radiation patterns. To explore if these radiations patterns are different from one another the concept of correlation coefficient will be introduced and will be described in the following section. In short NEC produces reliable results and when considering a complex geometry it is more preferable to use numerical tools rather then the analytical approach. A drawback of NEC is that it is difficult to analyse geometries consisting of materials with different dielectric constants.

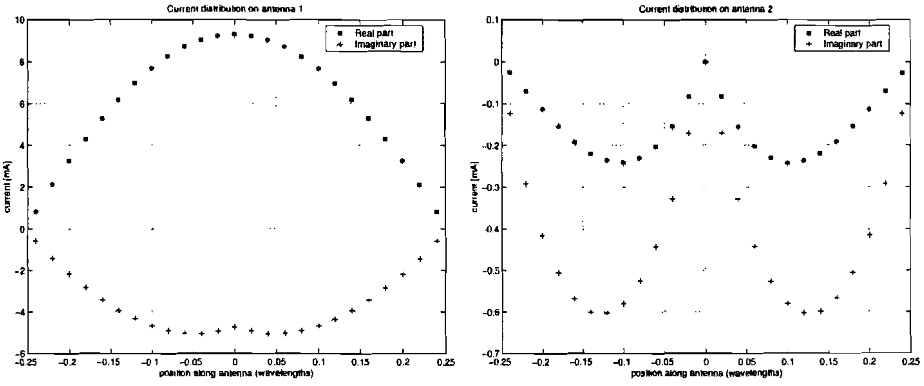

Figure 6.6: *Current distributions along the antennas with* $Z_\ell = 10^6\,\Omega$*, NEC simulations.*

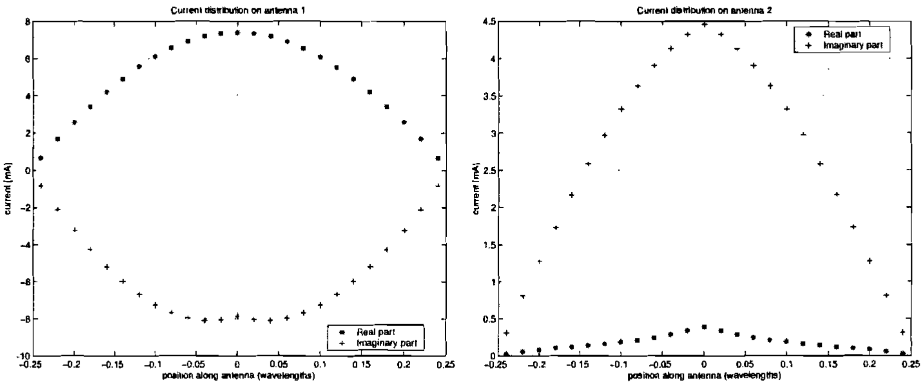

Figure 6.7: *Current distributions along the antennas with* $Z_\ell = 10 + 100j\,\Omega$*, NEC simulations.*

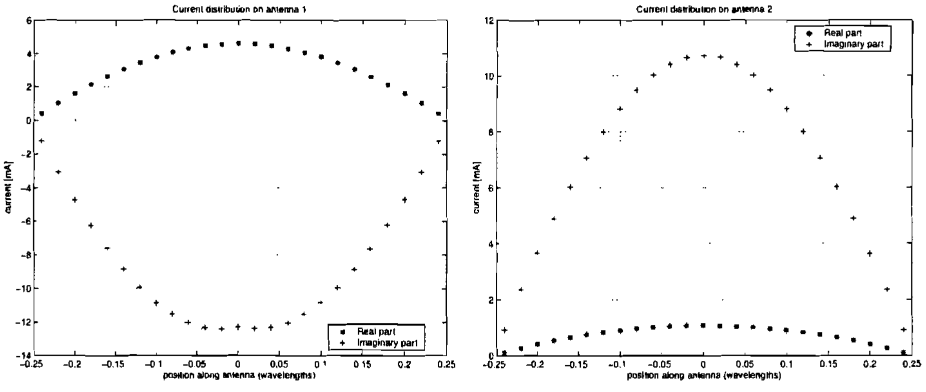

Figure 6.8: *Current distributions along the antennas with* $Z_\ell = 0\,\Omega$*, NEC simulations.*

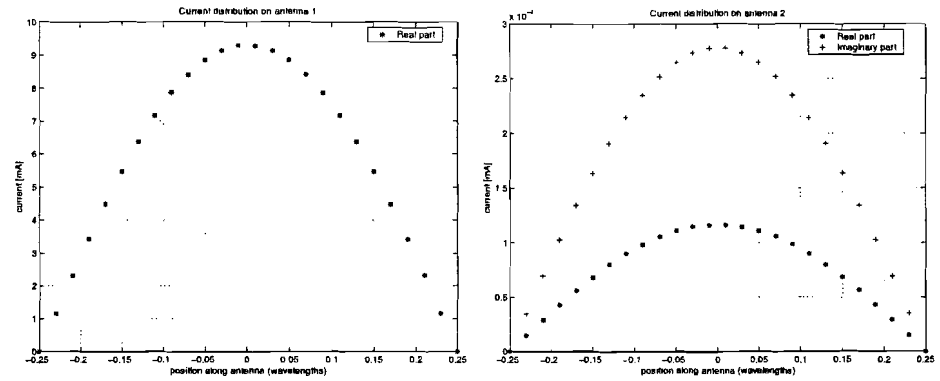

Figure 6.9: *Current distribution along the antennas with* $Z_\ell = 10^6\,\Omega$*, analytical model.*

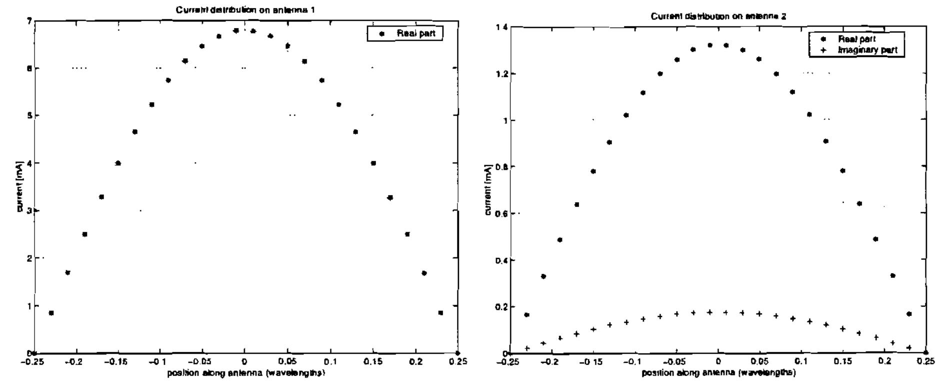

Figure 6.10: *Current distributions along the antennas with* $Z_\ell = 10 + 100j\,\Omega$*, analytical model.*

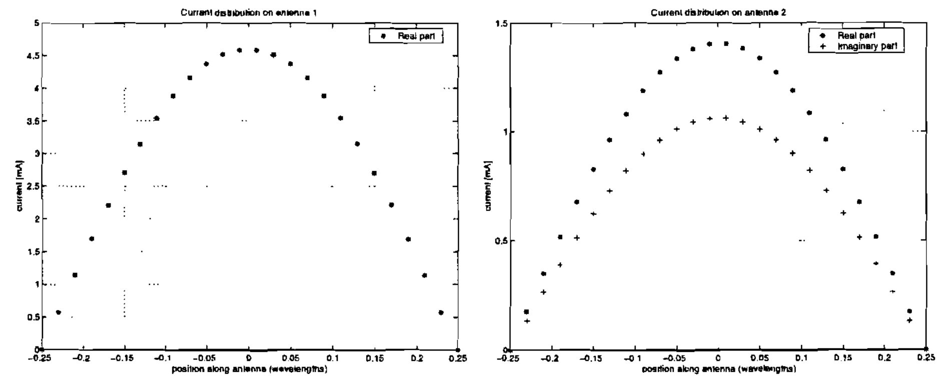

Figure 6.11: *Current distributions along the antennas with* $Z_\ell = 0\,\Omega$*, analytical model.*

6.3 Antenna correlation

As mentioned before the second antenna can be terminated with an impedance Z_ℓ which will influence the current distribution along the wire. The current distribution along the wire will alter the far field radiation pattern of the total antenna system. Switching between different impedances results in different current distributions along the (parasitic) antenna. These different current distributions also give different radiation patterns. We would prefer these radiation patterns to be as different as possible or orthogonal. Two radiation patterns are considered to be orthogonal when their complex dot product obey

$$\int_0^{2\pi} \int_0^{\pi} (\underline{E}_1, \underline{E}_2^*) \sin(\vartheta)\, d\vartheta\, d\varphi = 0 \tag{6.27}$$

A measure to judge the orthogonalism of different radiation patterns is the correlation coefficient ρ. In this case the correlation is based on antenna radiation patterns, so we should talk about antenna correlation ρ_a. A correlation coefficient of zero means totally decorrelated (or these patterns are orthogonal) and the opposite being a correlation coefficient of one meaning the two patterns are totally identical. So a boundary where two patterns are sufficiently decorrelated say ρ_a must lie between [0, 0.4]. Perfect decorrelated (means a correlation coefficient of zero) radiation patterns are hard to realize in practice. To calculate the correlation coefficient the radiation patterns are weighted with a probability density function (PDF) of the angle of arrival. As was shown in the previous chapter on transmit diversity the distributions cannot be approached by a uniform distribution (indoor environment!). In the following sub-section a PDF will be discussed.

6.3.1 AOA probability distribution function

Douglas and Taga [21, 22, 23] use a Gaussian PDF. These PDF's are based on an outdoor (multipath) environment. It is assumed that the mobile antenna moves randomly in a multipath environment. It is assumed then that the amplitude and phase of the elctrical field of the incident wave on the antenna are spatially independent and random. Futhermore non-correlation between the polarizations in the ϑ and φ directions is assumed. Therefore the PDF is split up into polarization components. P_ϑ can be modelled as having uniform distributions in the azimuth φ direction and Gaussian distributions in the elevation ϑ direction. Thus for $0 \leq \vartheta \leq \pi$ the PDF's are

$$P_\vartheta(\varphi, \vartheta) = A_\vartheta e^{\frac{-(\vartheta - [\frac{\pi}{2} - m_v])^2}{2\sigma_v^2}} \tag{6.28}$$

$$P_\varphi(\varphi, \vartheta) = A_\varphi e^{\frac{-(\vartheta - [\frac{\pi}{2} - m_h])^2}{2\sigma_h^2}} \tag{6.29}$$

where m_v and σ_v are the mean and the standard deviation of the incident angle of arrival of the vertically polarized waves and m_h and σ_h have the same meaning for the horizontally polarized waves. Furthermore the constants A_ϑ and A_φ are chosen in such a way to satisfy

$$\int_0^{2\pi} \int_0^{\pi} P_\vartheta(\varphi, \vartheta) \sin(\vartheta)\, d\vartheta\, \varphi = \int_0^{2\pi} \int_0^{\pi} P_\varphi(\varphi, \vartheta) \sin(\vartheta)\, d\vartheta\, \varphi = 1 \tag{6.30}$$

For the urban outdoor environment Taga measured values of $m_v = 19°$, $\sigma_v = 20°$,$m_h = 32°$ and $\sigma_h = 64°$. This means that the objects are seen from relative low elevation angles.

For suburban outdoor environments no published results of typical mean and standard of incident angles have been found. It is clear, however, that the incident waves arrive closer to the horizontal plane than incident waves in urban outdoor environments would do and that the standard deviation of arrival angles will also be smaller. When the objects around the observator come closer and closer to the observer the mean value increases and the standard deviation increases, too. It is possible to extrapolate this to an indoor environment. For this case the room is considered to be a room without a ceiling and having infinite (long) walls and the antenna in the room must not be put on the floor but at a certain height above this floor. This implies that there is finite probability that incident waves having an elevation angle greater than 90° will arrive at the antenna. Values of $m_v = \sigma_v = m_h = \sigma_h = 10^\circ$ are used to model the suburban outdoor environment [21]. For the urban environment values of $m_v = 19^\circ, \sigma_v = 20^\circ, m_h = 32^\circ$ and $\sigma_h = 10^\circ$ [21]. These vaules are obtained from measurements. Suitable values are chosen to model the pseudo indoor environment because we have only one measurement in an indoor enviroment which is insuffucient to obtain relaible statistics. These values of $m_v = \sigma_v = m_h = \sigma_h = 45^\circ$.

Figure 6.12 shows P_ϑ in the elevation plane for the suburban, urban and pseudo indoor environments. As shown in Figure 6.12 the PDF of the pseudo indoor environment can be considered almost uniform. In case of a real room the PDF will converge to a uniform PDF. In the previous chapter on transmit diversity it was shown that in a large room the PDF cannot be approached as a uniform distribution in which case care should be taken because the MUSIC algorithm is not suitable to obtain this information directly. So in this report the AOA PDF are assumed to be uniform and this was made plausible with the help of Figure 6.12. Therefore $P_\varphi(\varphi, \vartheta) = \frac{1}{4\pi}$ and $P_\vartheta(\varphi, \vartheta) = \frac{1}{4\pi}$.

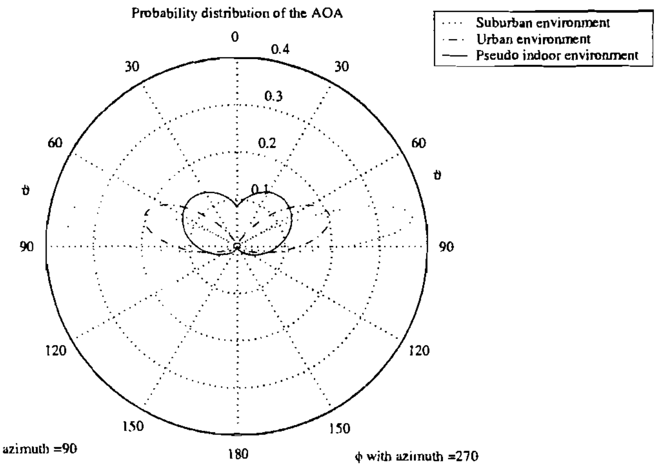

Figure 6.12: *Probability distribution of incident waves on the antenna in the suburban, urban and pseudo indoor environment (for ϑ polarization only). Shown in the elevation plane with $\varphi = 90^\circ$ and 270°.*

6.3.2 Antenna correlation for two closely spaced dipoles

Once the electrical field components and the AOA probability distribution functions are known the antenna correlation can be defined. Before the antenna correlation is defined the variables of electrical field components are changed from $\underline{r}$ into Ω (solid angle) as

$$\begin{aligned} \underline{E}_1(\Omega) &= E_{1\vartheta}(\Omega)\cdot e_\vartheta + E_{1\varphi}(\Omega)\cdot e_\varphi \\ \underline{E}_2(\Omega) &= E_{2\vartheta}(\Omega)\cdot e_\vartheta + E_{2\varphi}(\Omega)\cdot e_\varphi \end{aligned} \tag{6.31}$$

One can define the antenna correlation as (see Appendix B for a thorough elaboration)

$$\rho_a = \frac{\left|\int\int_\Omega E_{1\vartheta}E_{2\vartheta}^* P_\vartheta + E_{1\varphi}E_{2\varphi}^* P_\varphi \, d\Omega\right|}{\sqrt{\int\int_\Omega E_{1\vartheta}E_{1\vartheta}^* P_\vartheta + E_{1\varphi}E_{1\varphi}^* P_\varphi \, d\Omega \cdot \int\int_\Omega E_{2\vartheta}E_{2\vartheta}^* P_\vartheta + E_{2\varphi}E_{2\varphi}^* P_\varphi \, d\Omega}} \tag{6.32}$$

In our case the two closely spaced dipoles are used for which the φ component of the electrical far field is zero because the current is only distributed in the z direction and the cross section of the wire is small compared to the wavelength. Knowing this, (6.32) will reduce to

$$\rho_a = \frac{\left|\int\int_\Omega E_{1\vartheta}E_{2\vartheta}^* \, d\Omega\right|}{\sqrt{\int\int_\Omega E_{1\vartheta}E_{1\vartheta}^* \, d\Omega \cdot \int\int_\Omega E_{2\vartheta}E_{2\vartheta}^* \, d\Omega}}. \tag{6.33}$$

(6.33) is called the antenna correlation for two closely spaced dipoles pointing in the z-direction. The electrical field components are extracted from NEC output file.
What does this correlation coefficient tell us? What are the shapes of the radiation patterns when the correlation is low? In the next sub-section on evaluation of the antenna correlation these questions will be answered.

6.3.3 Evaluation of the antenna correlation

To obtain the correlation plots between two radiation patterns the following concept has been designed (also see Figure 6.13). Dipole A_1 is centre fed with a voltage source whilst the second dipole A_2 called the parasitic antenna will be terminated with an impedance. The antenna interspacing is equal to $d = 0.1\lambda$ or shortly $d_\lambda = 0.1$. For the second antenna, a two state switch is connected between the feeds and the impedances. In state zero a fixed impedance Z is connected giving the theta components $E_{1\vartheta}$. This impedance will be called the steering impedance. In state two a variable impedance $Z_{var}$is connected as shown in Figure 6.13 producing the second field components $E_{2\vartheta}$. Note that these impedances are purely complex numbers to improve the efficiency. Choose for example $Z = -100j$ and for $Z_{var} = -20j$. Perform NEC twice to obtain the two radiation patterns. Substitute these radiation patterns into (6.33) to generate the correlation coefficient which is equal to 0.3885.

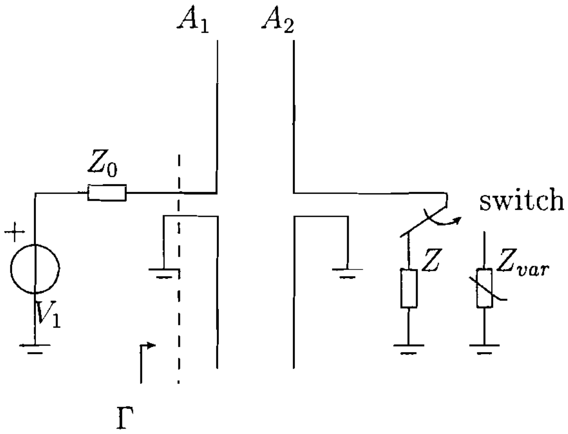

Figure 6.13: *Parasitic switching concept with two dipoles.*

This correlation coefficient is relatively low but what does this mean? In order to judge this relatively low correlation coefficient, the two radiation patterns are visualized in Figure 6.14 and Figure 6.15. As can be observed, these radiation patterns have a minimum overlap. So a low correlation cannot be obtained by means of making one pattern arbitrarily small and the other one arbitrarily large (see (6.33 the denominator is normalization factor). If we should have used one pattern that lies only in a half space pointing to the positive x-direction and a pattern that lies in half plane pointing to the negative x-direction then a correlation coefficient of zero will be the result. Unfortunately such patterns are hardly to realize.

In Figure 6.13 the capital gamma denotes the reflection coefficient at the antenna input. We want the reflection coefficient to stay below 10 dB while both impedances are varied.

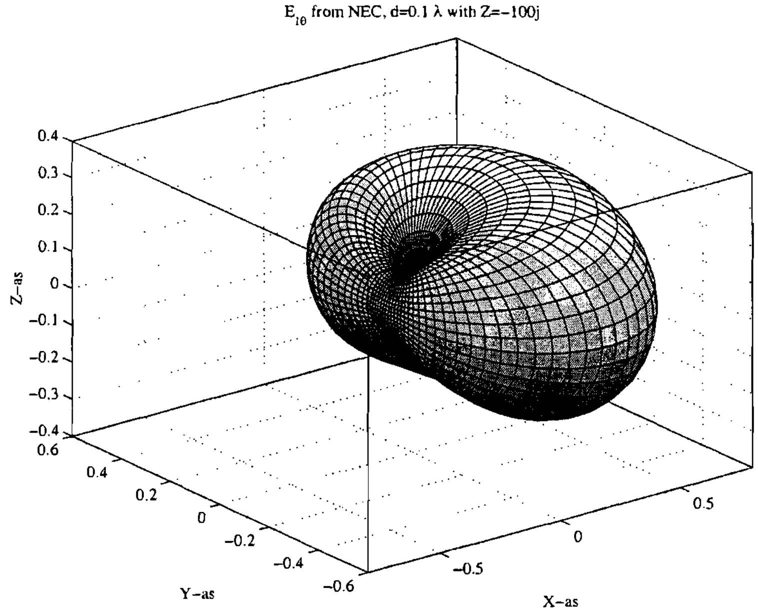

Figure 6.14: *Electrical far-field pattern at* $Z = -100j$.

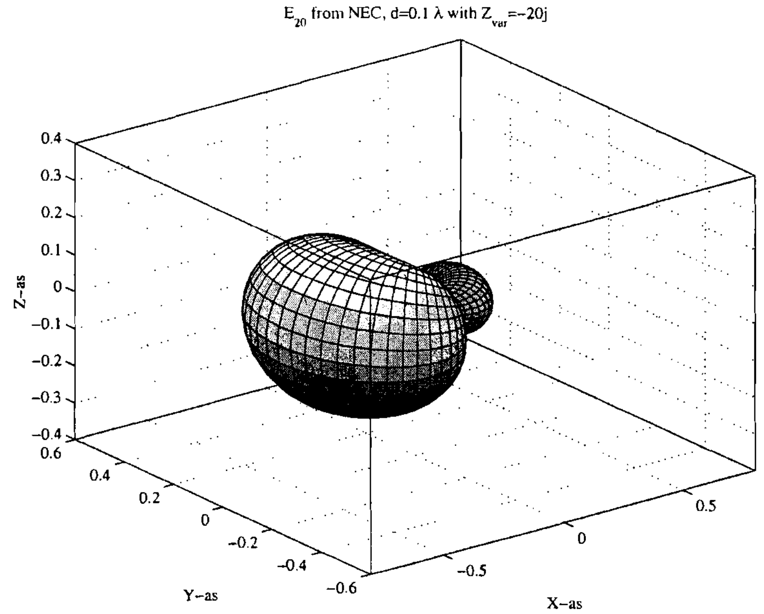

Figure 6.15: *Electrical far-field pattern at* $Z = -20\jmath$.

In order to find the lowest correlation coefficient an impedance sweep was carried out. Therefore the steering impedance Z was varied in six discrete steps as

$$Z = R + \jmath X \qquad \text{where} \qquad \begin{cases} R = 0 \\ X \in [-100, -50, 0, 50, 100, 10^6] \end{cases}$$

producing the $E_{1\vartheta}$ field. Next the variable impedance sweeps as follows

$$Z_{var} = R + \jmath X \qquad \text{where} \qquad \begin{cases} R \in [0, 10, 20, \cdots, 200] \\ X \in [-500, -460, \cdots, 500] \end{cases}$$

producing the second $E_{2\vartheta}$ field. Finally we have six correlation plots and one reflection or return loss (RL) plot where Z_{var} is used as independent variable. In appendix C these plots are shown. In studying these plots it appears that the real part of the varied impedance Z_{var} slightly influences the correlation plot. The best results are obtained for $Z = -100\jmath$ and $Z_{var} = -20\jmath$ since it will give a low correlation coefficient. When studying the return loss plot, we can conclude that the return loss is bad and a matching circuit is needed. This means that at the terminals of the dual antenna a lot of the power will be due to reflections.

Since the real part of Z_{var} has no significant contribution, a 2D cumulative plot is made where only the reactance is used as variable (see Figure 6.16 and Figure 6.17). Figure 6.16 shows that around a short $Z_{var} \approx 0$ the best correlation can be achieved, a best correlation means in this case a low correlation coefficient. Moreover the first three steering impedances gives the best results. But we want a small return loss at these low correlation coefficients. In practice a return loss smaller than or equal to -10 dB is used. Figure 6.17 shows that only for $-160\jmath \leq Z_{var} \leq 100$ a return loss smaller than -10 dB is achieved. Unfortunately for $Z_{var} = -20\jmath$ the return loss is greater than -10 dB and a matching

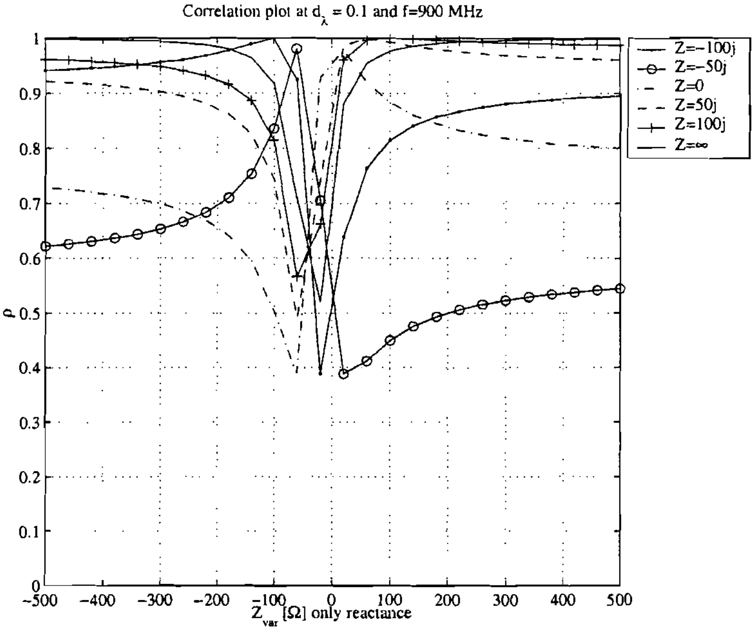

Figure 6.16: *Correlation plot with the reactance as variable and Z as parameter.*

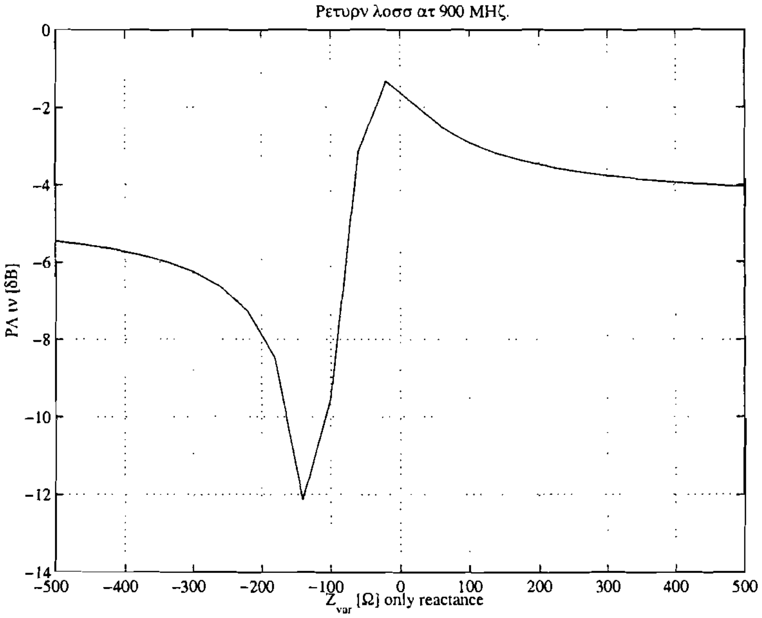

Figure 6.17: *Return loss (RL) plot with the reactance as variable.*

circuit is needed. Since the GSM system has certain frequency bandwidth it is desirable that the low correlation coefficient is somewhat frequency independent. At 900 MHz the lowest correlation coefficient is found by $Z = -100\jmath$ and $Z_{var} = -20\jmath$ corresponding to capacitance of 1.7684 pF and 8.8419 pF respectively. A frequency sweep form 890 MHz to 960 MHz was performed where the impedances Z and Z_{var} are automatically scaled with frequency. Figure 6.18 shows the result of the frequency sweep. The correlation coefficient is relatively steady except on the right hand side of the plot the correlation coefficient deflects from 0.5 to 0.7.

The same frequency sweep was done for the return loss. We already know that the return loss is very poor when the impedances Z_{var} vary. Figure 6.19 shows the result when a frequency sweep is performed. Meaning that the return loss becomes only worse.

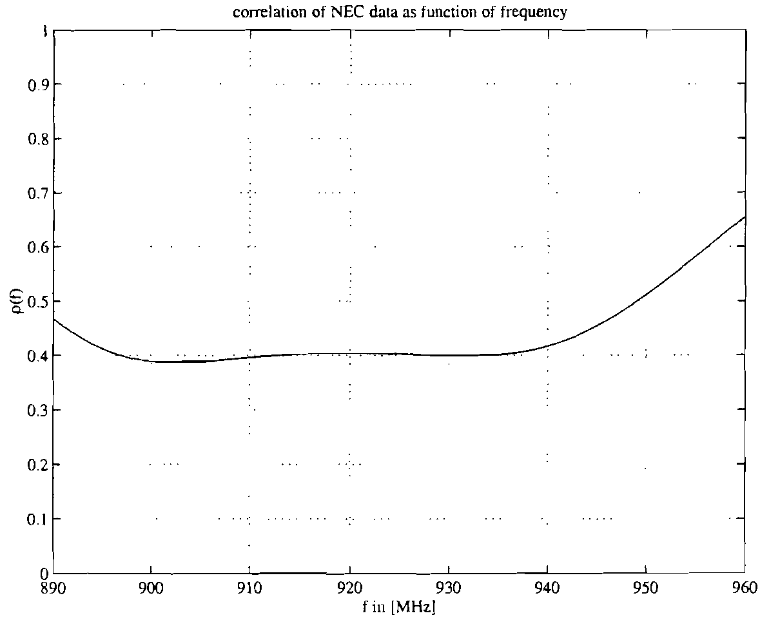

Figure 6.18: *Correlation as a function of the frequency when $Z = -100\jmath$ and $Z_{var} = -20\jmath$ are used (obtained from 900 MHz).*

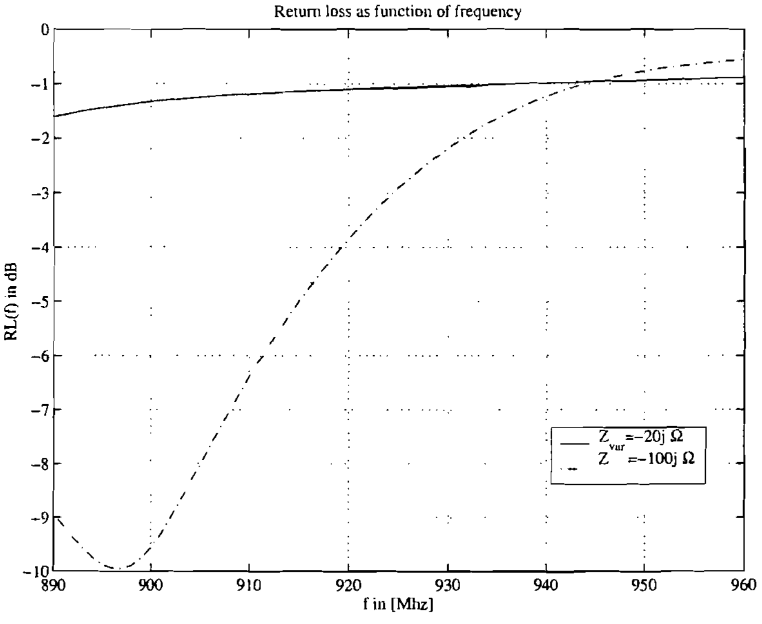

Figure 6.19: *Return loss as a function of the frequency when* $Z = -100\jmath$ *and* $Z_{var} = -20\jmath$ *are used.*

6.4 Conclusions

First an analytical model was derived in order to compare the NEC results. Apparently NEC produces accurate data and converged when the preconditions are fulfilled. Furthermore in this chapter it was shown that the dual antenna system which makes use of the mutual coupling causes the far-field radiation patterns to change when the antenna interspacing varies. At very short antenna interspacings the mutual coupling has a strong influence on the current distributions along the wires. Moreover it was shown that with closely spaced dipole antennas the far field radiation pattern can be modified when terminating the parasitic antenna with a certain impedance. In order to judge the differences between the radiation patterns the correlation coefficient was introduced. With the dual antenna system a correlation coefficient smaller than 0.5 can be achieved.

It is clear that antenna pattern diversity using two closely spaced vertically polarized dipoles works well in theory. In this case one antenna is used as a primary antenna and the other one is used as a parasitic antenna which can be terminated with an impedance.

Since we are dealing with the GSM-system with certain frequency bandwidth we want the correlation coefficient to be smaller than 0.5 within this bandwidth. It has been shown that this was almost the case. This implies that both in the R_x and in the T_x band diversity gain can be achieved without additional switching.

A disadvantage of this concept is that the return loss is very poor even when the frequency is changed. Therefore a matching device is preferable to improve the return loss.

If the impedance connected at the terminals of the parasitic antenna is changed the input impedance of the dual antenna changes too which also causes degradation of the return loss.

Chapter 7

Performance of prototype

7.1 Introduction

In order to verify the low correlation coefficient based on far field radiation patterns we should measure the radiation patterns. Since a measurement set-up to measure the radiation patterns is not available, a different method will have to be consulted. This indirect method is the input impedance at the antenna terminals of the dual antenna system. A certain far field radiation pattern corresponds to a certain current distribution along the wire. Knowing the current at the antenna terminals implies knowing the antenna impedance. Fortunately NEC also gives the antenna impedance so that the simulated impedance and the measured impedance can be compared.

Before the dual antenna will be used for verification we will start with a simple dipole antenna to obtain a suitable measurement set-up. Type network analyzer which has been used for the measurements is the HP 8753E and has a frequency range from 30 kHz to 6 GHz (see Figure 7.1). The HP 8753E is a high performance vector network analyzer for laboratory or production measurements of reflection and transmission parameters. It integrates a high resolution synthesized RF source, an S-parameter test set and a dual channel three-input receiver to measure and display magnitude, phase and group delay responses of active and passive RF networks.

Two independent display channels and a large screen color display show the measured results of one or both channels, in rectangular or polar/Smith chart formats. Moreover the HP 8753E has the additional following features:

- Combined digital signal processing and microprocessor controls to provide easy operation and measurement improvement.
- Automatic sweep time that selects the minimum sweep time for the given IF bandwidth, number of points, averaging mode, frequency range and sweep type.
- Performance improvement and flexibility through trace math, data averaging, trace smoothing, electrical delay and accuracy enhancement.
- Complete reflection and transmission measurements in either 50 or 75 ohm impedance environments.

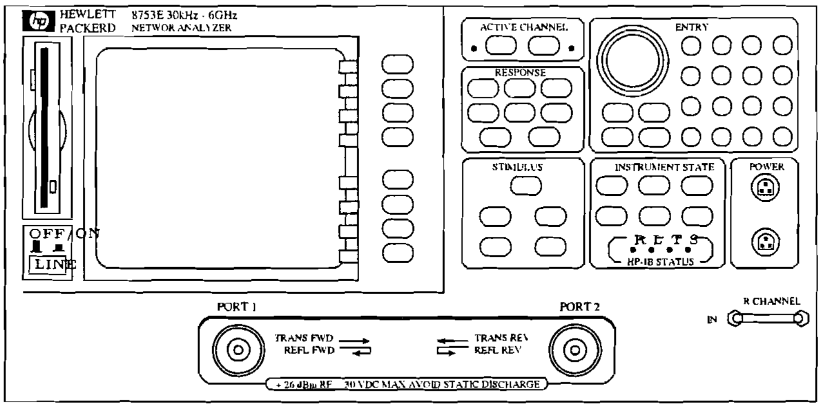

Figure 7.1: *HP 8753E Front Panel.*

At PORT 1 of the network analyzer the vertically polarized dipole antenna is connected by means of cable. PORT 1 is also denoted as the forward port. At PORT 2 also denoted as the reverse port of the network analyzer the dual antenna system is connected. The entire configuration represents a passive RF network. When using the HP 8783E network analyzer we should first calibrate the network analyzer to nullify the systematic errors. The calibration procedure will not be described in this report and the reader is advised to read the user's manual of HP 8753E. In sections 7.2 and 7.3 two measurement methods are discussed to measure the input impedance of the dual antenna system. In section 7.4 the results of the input impedance of the dual antenna system. The for last section 7.5 discusses the performance of the dual antenna system. Finally a conclusion is drawn in section 7.6

7.2 Impedance measurement unbalanced

When a single antenna with a length of $\frac{\lambda}{2}$ is positioned in free space then the theoretical impedance Z_a at the antenna terminals is equal to 73.15 Ω [4]. NEC calculates a value of $Z_a = 84.1644 + 48.2865\jmath\ \Omega$ and is certainly not equal to 73.15 Ω. The reason for this inconsistency is that the length has to be multiplied by a so called shortening factor called K-factor. The K-factor is obtained by running NEC while lowering the antenna length till the resonance length is reached. From the results of NEC the resonance impedance equals to $Z_a = 71.83 - 0.0071\jmath \approx 71.83\ \Omega$. At the resonance frequency the K-factor is equal to 0.95152. This implies that the effective length is shorter than $\frac{\lambda}{2}$. In other words if a half lambda dipole antenna will be used the resonance frequency is lower than 900 MHz. Moreover the calculated impedance with NEC deviates from the theoretical impedance and may be explained as poor numerically conditioned. The reason for this shortening factor is the finite conductance of the wire which results that the vector of Poynting not being perfectly perpendicular at the wire.

Finally the half dipole antenna was built, the thickness of the (iron) wire is equal to 0.5×10^{-3} meters. In order to calibrate the network analyzer a correct calibration kit must be selected which is in this case the 85033D 3.5 mm calibration kit. This calibration kit contains three standards: an open, a short and a load (50 Ohm). When measuring the single dipole antenna only PORT 1 of the network ananlyzer should be calibrated. The total measurement set-up is depicted in Figure 7.2.

At 900 MHz the impedance Z_a is equal to $66.578 + 1.83j\ \Omega$ and fluctuates a lot especially when there are moving objects in the vicinity of the antenna. This type of measurement is called an unbalanced measurement. Unfortunately this method will give us inaccurate results because the environment influences the measured impedance. The reason for this peculiarity is still unknown but it may have something to do with the return current through the outer shielding of the cables. In order to obtain reliable results a balanced measurement will be provided. This balanced measurement method will be described in the following section.

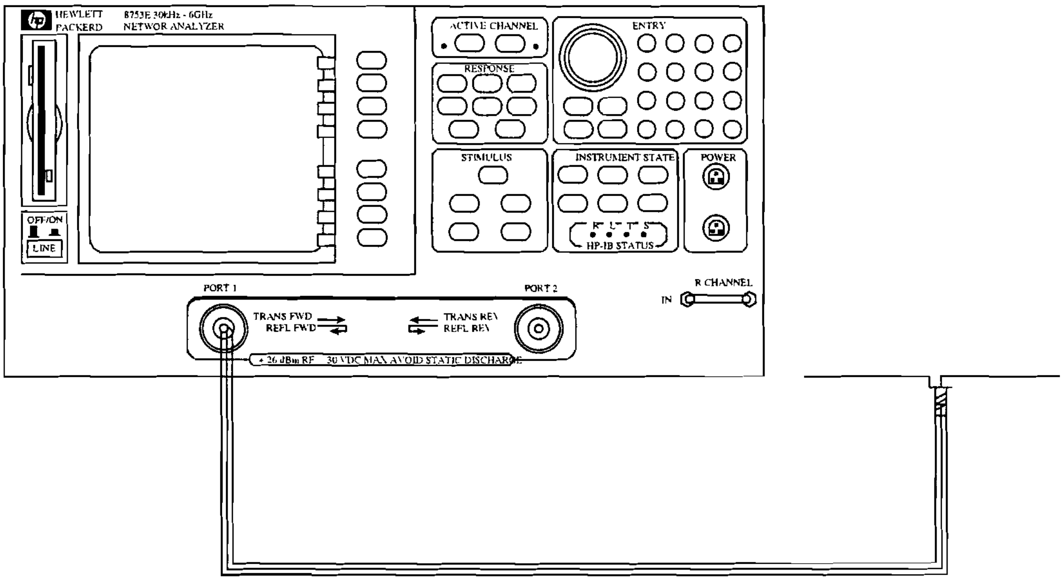

Figure 7.2: *Measurement set-up for the single dipole antenna.*

7.3 Impedance measurement balanced

Before a balanced measurement can be done we need a balance to unbalance transformer device because the network analyzer is only suitable for unbalanced circuits. The balance to unbalance transformer will be abbreviated with balun. In this case we have two cables connected to a single antenna. So the halfwave dipole antenna will be fed in a balanced way. If the antenna is at its resonance frequency the load impedance of the antenna at the balanced terminals equals to 73.15 Ohm. The impedance measured at the PORT1 of the network analyzer (is the unbalanced side) is certainly not equal to 73.15 Ohm. In the following sub-section the balun device will be discussed.

7.3.1 Hybrid used as balun

Consider a ideal hybrid device with four terminals as depicted in Figure 7.3. These four ports are labelled as 1, 2, 3 and 4. When using port 1 and port 4 as combination the transfer function is equal to $e^{-j\pi}$. So from port 1 to port 2 causes in the ideal case only a phase shift of 180 degrees and no attenuation. And when using port 1 and port 3 as combination no phase shift and no attenuation is done. As a consequence the two terminals at the end of the cables which are connected at port 3 and 4 behave like balanced transmission line with a characteristic impedance of 100 Ohm. The calibration procedure needs in this case

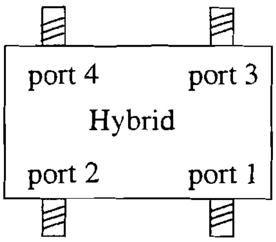

	port 4	port 3		
port 1	180	0	ISOL	/
port 2	0	0	/	ISOL
port 3	ISOL	/	0	0
port 4	/	ISOL	0	180
			port 2	port 1

Figure 7.3: *Hybrid device used as balun and on the right-hand side the transfer functions (ISOL stands for isolated).*

2 × 3 calibration standards of the same type. After the calibration procedure the port extension option should be used to shift the reference plane at the end of the connector. The connectors can be considered to be approximated with a short transmission line. In this case the calibration procedure is not accurate because the compensation for the self-made antenna connectors failed (compensation is likewise using the port extension). It is still unclear why the compensation cannot be done correctly. In order to obtain an antenna with two terminals, two SMA connectors were soldered together as shown in Figure 7.4. This also changes the measurement set-up, the balun is placed between the network analyzer and the two-terminal antenna as outlined in Figure 7.5. A thorough analysis of how a non-ideal balun device works can be read in [12].

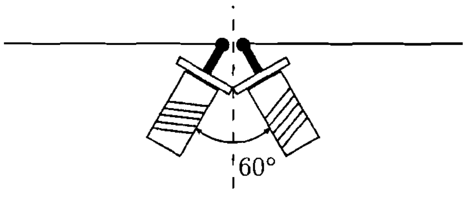

Figure 7.4: *Two-terminal halvewave dipole antenna using the SMA-50-0-1 connector.*

7.3.2 Impedance measurements

The two-terminal antenna input impedance can be modelled as an antenna impedance and the parasitic impedance (see Figure 7.6). So the measured input impedance is not the actual antenna impedance but the total impedance at the antenna terminals which consists of the desired antenna impedance and the impedance caused by the parasitic capacities. In order to obtain value of the parasitic capacity a single dipole is used. Suppose that the dipole antenna will operate at its resonance frequency then the antenna impedance only consists of a real part R_a but the measured input impedance Z_m has a certainly an imaginary part. This imaginary part is mainly due to the parasitic capacities. Therefore it is possible to correct the measured input impedance for these parasitic capacities which is done as follows. The measured input impedance Z_m at the antenna terminals equals to:

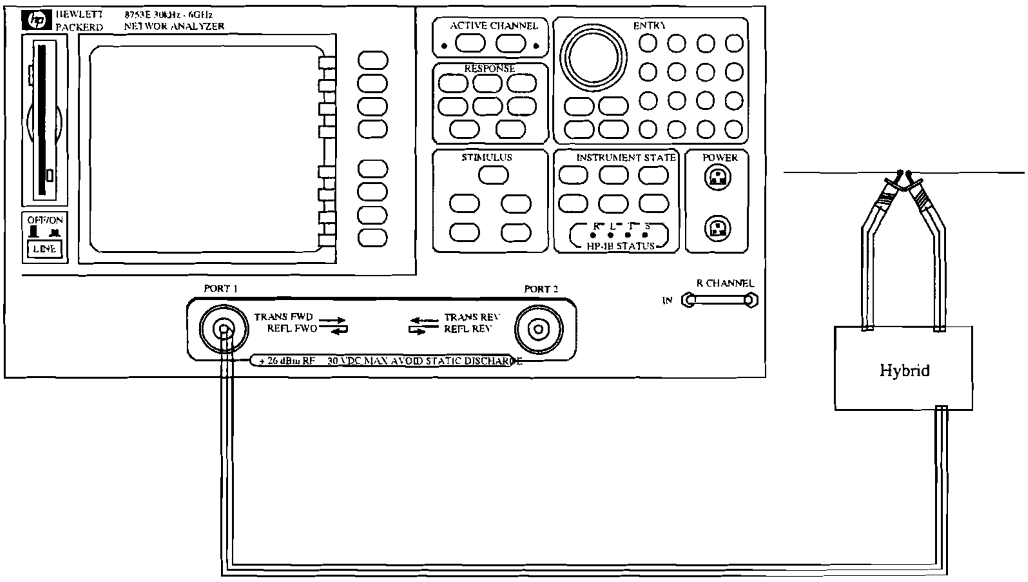

Figure 7.5: *Measurement set-up for the single dipole two-terminal antenna when the balanced method is used.*

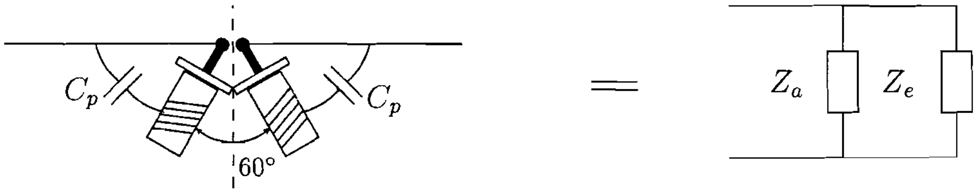

Figure 7.6: *Equivalent circuit for the single dipole two-terminal antenna (C_p denotes the parasitic capacitance) and Z_e denotes the equivalent impedance.*

$$\begin{aligned} Z_m &= R_m + jX_m \\ &= \frac{R_a}{1+\omega^2 R_a^2 C_e^2} - j\frac{\omega R_a^2 C_e}{1+\omega^2 R_a^2 C_e^2} \end{aligned} \tag{7.1}$$

where C_e is the equivalent capacitance. Equation (7.1) can be deduced by means of a parallel connection of the antenna impedance and the parasitic impedance z_e which equals to $\frac{Z_a \cdot Z_e}{Z_a + Z_e}$. Rearrange Equation (7.1) to obtain the radiation resistance R_a and the parasitic capacitance C_e which is:

$$R_a = R_m\left(1 + \left(\frac{X_m}{R_m}\right)^2\right) \tag{7.2}$$

$$C_e = -\frac{X_m}{\omega\left(R_m^2 + X_m^2\right)}. \tag{7.3}$$

The results of the measurement are:

$$\begin{aligned} Z_{na} &= 33.559 - 8.4632\jmath\ \Omega && (7.4)\\ Z_m &= 67.118 - 16.9264\jmath\ \Omega && (7.5)\\ R_a &= 71.3866\ \Omega && (7.6)\\ C_e &= 0.62472\ \text{pF} && (7.7)\\ C_p &= 1.24944\ \text{pF}. && (7.8) \end{aligned}$$

Compare $R_a = 71.3866\ \Omega$ to the simulated NEC resistance of 71.83 Ω and we will conclude that the measured resistance R_a is very close to the simulated resistance. Moreover the parasitic capacitance C_p of 1.24944 pF is relatively small but large enough to disturb the measurements. Apparently the balanced method gives us more accurate numbers and is less sensitive to fluctuations due to the environment. Therefore the balanced method will be used to verify the impedance of the dual antenna system.

When using the dual antenna system the input impedance of the dual antenna cannot be considered as purely real. Equation (7.1) has to be modified in order to incorporate the reactance X_a of the dual antenna system. Compensating for the equivalent parasitic capacitance is done as follows:

$$Z_a = \frac{Z_m \cdot Z_c'}{Z_m + Z_c'} \tag{7.9}$$

where Z_c' denotes the anti value of Z_c or $Z_c' = -Z_c$.
Substitute $R_m + \jmath X_m$ for Z_m and $\frac{-1}{\jmath\omega C_e}$ for Z_c in 7.9:

$$\begin{aligned} R_a &= \frac{R_m}{\left(1+\omega C_e X_m\right)^2 + \omega^2 C_e^2 R_m^2}\ \Omega \\ X_a &= \frac{X_m + \omega C_e\left(R_m^2 + X_m^2\right)}{\left(1+\omega C_e X_m\right)^2 + \omega^2 C_e^2 R_m^2}\ \Omega. \end{aligned} \tag{7.10}$$

Equation (7.10) will be used for further analysis. In the following section the input impedance of the dual antenna system will be measured and compared with the input impedance calculated with NEC.

7.4 Impedance measurements of the dual antenna system

In the preceding chapter a low correlation coefficient $\rho = 0.3885$ was found for the load impedances $Z_\ell = -100\jmath\ \Omega$ and $Z_\ell = -20\jmath\ \Omega$. NEC calculates the antenna input impedances as $Z_{a,NEC} = 82.2711 + 34.1240\jmath\ \Omega$ and $Z_{a,NEC} = 13.9515 + 44.7467\jmath\ \Omega$ respectively. The lengths of the dipole antennas are the effective lengths instead of a half lambda. Both load impedances are capacitances and at 900 MHz these capacitances are equal to 1.7684 pF and 8.8419 pF. These values are rounded up to the values mentioned in the E12 series and are 1.7 pF and 6.8 pF. Therefore the load impedances changes slightly and are $Z_\ell = -104.0228\jmath\ \Omega$ and $Z_\ell = -26.0057\jmath\ \Omega$ which changes the input impedance slightly. The results of the dual antenna input impedance measurements are shown in Table 7.1. The measured input impedances differ from the calculated input impedance with NEC. After further investigation it appears that the calibration procedure is not quite

	$Z_\ell = -104\jmath$	$Z_\ell = -26\jmath$
Z_{na}	$43.619 + 0.1666\jmath$	$11.135 + 10.427\jmath$
Z_m	$87.2380 + 3332\jmath$	$22.270 + 20.854\jmath$
Z_a	$79.4999 + 24.8048\jmath$	$19.2155 + 20.8311\jmath$
$Z_{a,NEC}$	$82.2711 + 34.1240\jmath$	$13.9515 + 44.7467\jmath$

Table 7.1: *Measured input impedance of dual antenna system (impedances shown in Ohms), where Z_{na} denotes the impedance measured at the input port of the network analyzer.*

as accurate as we had expected. The problem of the calibration procedure had not been solved before this report was written. Despite of this problem a performance analysis was carried out which will be discussed in the following section.

7.5 Performance analysis of prototype

In addition to the impedance measurement we want to know the performance of the dual antenna system. In this section the performance will be analyzed with the help of a coverage plot. Measurements are used in order to obtain a quantitative performance. In preceeding chapter it was shown that the return loss is worse over the entire GSM bandwidth. For this reason only one frequency component is used. In the analysis of the prototype a frequency of 900 MHz. Moreover for $Z_{var} = -26\jmath$ the RL is worse. A suitable matching circuit was not found before writing this report.

7.5.1 Definition of performance

The improvement in performance for diversity handhelds can be expressed in array gain (AG) and diversity gain (DG). The array gain is defined as the spatial average signal-to-noise ratio of the diversity receiver compared to the signal-to-noise ratio of a single antenna or

$$\text{AG} = (\nu_d)_{AV} - (\nu_s)_{AV} \qquad [\text{dB}]. \tag{7.11}$$

In our case the dual antenna system has a array gain of 1.8 dB and is obtained from measurements. In addition to the array gain, diversity gain is obtained because of the 'dead spots' are avoided by using multiple antennas at the handheld. The diversity gain is a measure for the reduction of the spatial variations in the received signals. The diversity gain is determined by the transmitted power differences for diversity and non-diversity receivers at a coverage of 99% or

$$\text{DG} = P_{ts}(99\%) - P_{td}(99\%) \qquad [\text{dB}]. \tag{7.12}$$

The diversity gain DG is obtained by the so called coverage plot. This implies that the entire xy-table is subdivided into M observation points, at each observation point the power will be measured. Furthermore define an average bit error rate (BER) at a certain modulation scheme and determine the noise power in the concerning bandwidth. Once the noise power and the modulation scheme are known the required signal power can be calculated at this BER. The coverage is defined as the percentage of the areas inside the indoor configuration with a probability of error better than a threshold value. The threshold Pe_{AV} denotes a space average user defined probability of error which determines the percentage of coverage in the multipath radio channel. This quantity is usually expressed in procents. So the formula for the coverage is $\frac{\# P_e(\underline{r})<P_{AV}}{\#\,\text{total points}}$. In this report the GMSK modulation (according to the GSM specification) scheme will be used to calculate the BER (readers who are not familiar with modulation techniques are referred to [1]). This means that the bit error probability Pe is given by

$$Pe = Q\left\{\sqrt{\frac{1.36E_b}{N_o}}\right\} \tag{7.13}$$

where the constant is related to BT product.

The concept mentioned in Chapter 6 contains a electronic switch which has to be synchronized with the network analyzer and the PC. The current software which controls the network analyzer and the xy-table is not compatible to incorporate the electronic switch. Another aspect is the measuring time in each state of the switch. We want that the environment remains absolute stationary in both states. If this is not the case, diversity gain is obtained due to the changes in the environment and we do not want that.

The switch can be avoided by means of a software switch. This means that two measurements have to be done, one with load impedance $Z = -100\jmath\ \Omega$ and one with load of $Z = -20\jmath\ \Omega$ and from these two measurements the maximum power at each observation point will be put into a new data sequence. Each measurement has a duration of approx. 2 hours. But when doing so the environment must not change during the measurement. The changes in the environment can be caused by turning on a GSM handheld which introduces additional energy in the GSM frequency band. The additional energy will cause a false diversity gain. In order to avoid these false diversity gains due to the environment the entire measurement set-up is placed in a cage of Faraday (see Appendix D pictures D.5 and D.6).

In order to obtain a smooth curve of the coverage plots the number observation points M equals to 5551, 61 in the x-direction and 61 in the y-direction both sides with a resolution of 1.0 cm at 1000 MHz. Moreover the number of frequency sweep points is reduced to three to avoid lengthy data sequence. These three frequency sweep points are 800 MHz, 900 MHz and 1000 MHz. The results will be discussed in the following sub-section.

7.5.2 Measurements in a cage of Faraday

In order to check the stationarity two measurements were done with a single dipole antenna. The result can be found in Figure 7.7 solid lines. It can be seen from this figure that there is hardy diversity gain due to the environment. Enlarging Figure 7.7 around 99% gives Figure 7.8. We can see that the solid lines do not coincide this might be due to the finite data points. We can conclude that the environment can be considered as stationair. Knowing this we can measure the performance of the prototype.

Two measurements were done and are denoted by M_1, M_2. After these two measurements a new data sequence is formed which obeys to $M_3 = \max\{M_1, M_2\}$. From the new formed data sequence a coverage plot will be made as well as from the data of a single antenna. This is done in order to obtain the diversity gain. Furthermore space diversity, as explained in chapter 2, is also applied to the data of the single antenna for different spacings which are 0.5λ and 0.25λ based on selection. The results of the coverage plots are shown in Figure 7.7.

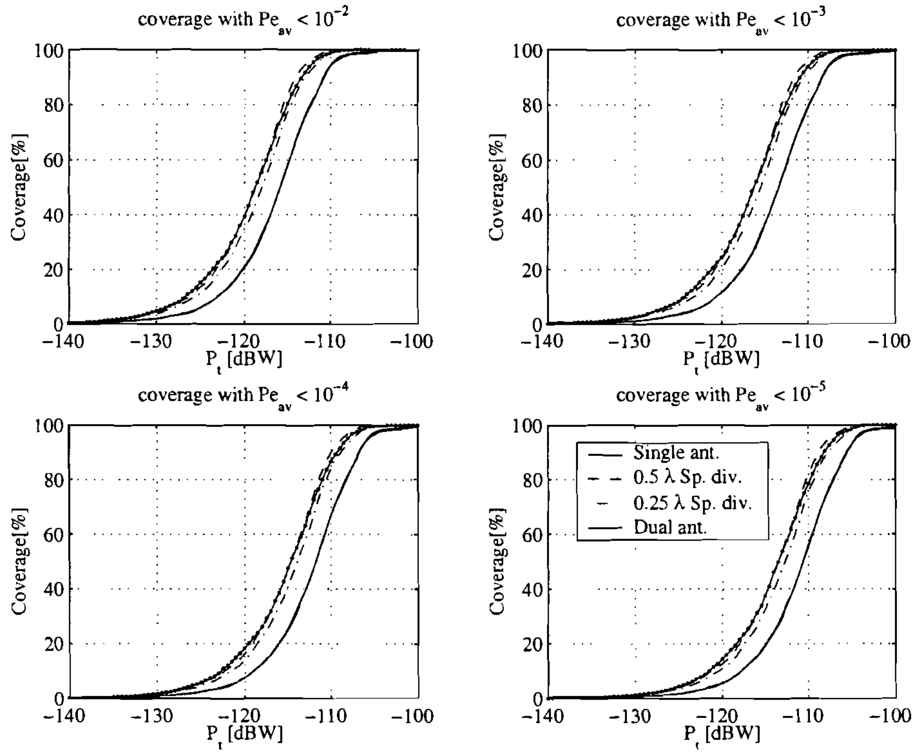

Figure 7.7: *Coverage for GMSK modulation scheme at different bit error rates BER over the xy-plane from the xy-table.*

In Figure 7.7 the coverage range from 0 to 100% but we are only interested in coverage near 98-100%. A coverage of 10% has no single meaning in practice and is only for the sake of completeness. Therefore the coverage plots are enlarged around 99% and are shown in Figure 7.8. The non-smoothing path of the coverage curves are due to finite data points. In studying Figure 7.8 the diversity gain is the difference between the curve of the single antenna and the dual antenna system at 99% and is approximately 6 dB at $Pe_{AV} < 10^{-3}$. This means that for coverage of 99% a diversity gain of 6 dB can be achieved using a dual antenna system based on switching between two different loads. But the question is how accurate is the diversity gain of 6 dB? First of all we have to realize that with the dual antenna system we have an array gain which is equal to 1.8 dB. Moreover the finite data points results in a deviation in the diversity gain. Dolmans[26] found that for space diversity with antenna spacings of 0.5λ and 0.25λ the diversity gains are equal to 9 and 8 dB at $Pe_{AV} < 10^{-3}$ (based on selection and a coverage of 99%). In our case the diversity gains are equal to 8 and 7 dB at $Pe_{AV} < 10^{-3}$. He uses 10,000 points in order to obtain these diversity gains while in this report 5551 points are used. So it might be that the diversity gain of 6 dB is obtained beyond the convergence abscis of the coverage plots. But if more data points are considered the more accurate the diversity gain will be. Finally we can conclude that the dual antenna system has a comparable performance to the selection diversity technique with an antenna interspacing of 0.25λ.

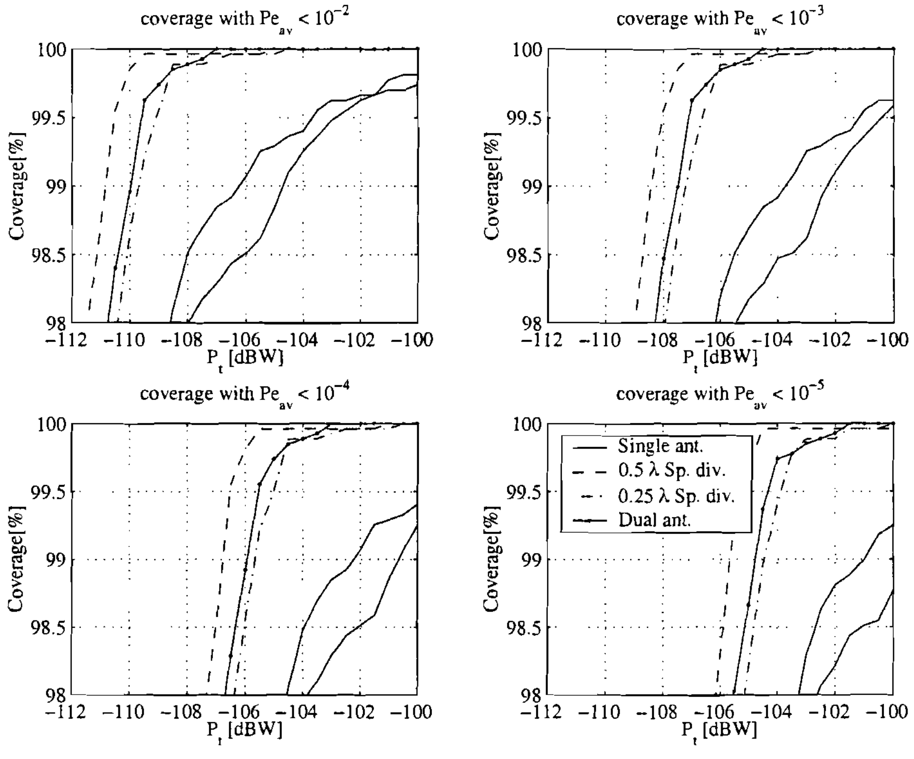

Figure 7.8: *Coverage for GMSK modulation scheme at different bit error rates BER over the xy-plane from the xy-table enlarge around 98%.*

7.6 Conclusions

In the balanced measure method the input impedance of the dual antenna system is better measured than the one compared to the unbalanced measure method. When using the balanced method the network analyzer must be calibrated in a different way in order to cancel out the systematic errors. The impedance measurements of the dual antenna system are not as accurate as we had expected.

The electronic switch was replaced by a software switch. Since we need three measurements each having a duration of approx. 2 hours the radio channel should be stationary. Therefore the measurements were done in the cage of Faraday. Another advantage of doing so is that interference is not integrated in the measurement. The performance of the dual antenna system is expressed in a diversity gain and are obtained from coverage plots.

It was shown that a diversity gain of 6 dB is achieved with this concept. Moreover the diversity gain of the dual antenna system is as close as the selective diversity technique using an antenna interspacing of 0.25λ. In addition to the diversity a array gain was defined which equals to 1.8 dB.

Chapter 8

Conclusions & Recommendations

8.1 Conclusions

In order to measure the radio channel characteristics a measurement set-up is available. This measurement set-up consists of a xy-table, xy-controller, PC and a network analyzer. When using the measurement set-up we must bear in mind that some errors may occur in the data. These errors are the antenna mismatches and the systematically errors introduced by the cables. For the former a manual correction method exists at the cost of the phase information. For the latter a correction method is also available by means of calibrating the network analyzer. For the case that the antennas are properly designed the antenna mismatch is negligible. After the correction has been performed the data phase information will be lost.
With the help of the xy-table the GSM radio channel was measured. Furthermore the principle of antenna pattern diversity was explained. In this situation the diversity parameters will be set during reception but will also be used during transmission (from handset to basestation). We showed that this implies that the radiation pattern of the mobile will change. By means of the radiation pattern it is possibility to mute several destructive interferences. In order to make the antenna pattern diversity a success it is preferable that the AOA is independent of the frequency. First a channel correlation was done to extract the AOA information. It appears that more information was obtained about frequency diversity and space diversity rather than information about AOA's. Therefore two AOA estimators were explored which will give the AOA information.

These two prominent algorithms to obtain these angles of arrival are the Fourier method and the MUSIC algorithm, both must meet the plane wave hypothesis. The former method is based on an integration over finite interval and the latter is based on the eigenstructure of a covariance matrix. When using the Fourier transform the spatial resolution is worse at an aperture length of 1 meter. For a high resolution the aperture length will become too large and is therefore impractical. In order to obtain a high resolution at a relative small aperture length an eigenstructure-based algorithm was used. Using MUSIC with an aperture length of 1 meter produces an acceptable spatial resolution. At an aperture length of 1 meter MUSIC has a spatial resolution that a factor 8 better is than compared with Fourier method. Furthermore MUSIC needs a preprocessing scheme in order to deal with highly correlated sources called spatial smoothing. When introducing the spatial smoothing scheme a new variable was introduced namely the sub-array size. The sub-array size is not an arbitrary number but is a trade-off between the spatial resolution on the one hand and the decorrelating of the highly correlated sources on the other hand. This preprocessing scheme reduces the total number of detectable plane waves. A draw-back of these algorithms is that only information about the elevation with respect to the synthetic array will be obtained.

The MUSIC algorithm was used to obtain the angle of arrival information using measured data. Three measurements were done two of them in the horizontal xy-plane and one of them in the vertical xz-plane. The latter measurement is needed to investigate if there are any plane waves travelling across the vertical plane. After MUSIC was applied to these data it appeared that the z-direction might consists of standing waves. In studying the two measurements in the xy-plane the angles of arrival are strongly correlated in the concerning bandwidth which matched with the theory. Since the z-direction consists of standing waves it is only indicative of the fact that there are waves travelling in the vertical plane. In order to draw a reliable conclusion a channel correlation was done based on the angle of arrival. These plot shows us that the correlation can be considered strongly correlated over the entire GSM bandwidth. This implies that the dominant angles of arrival in the transmit band are likewise dominant in the receive band. This all tells us that antenna pattern diversity can be applied.
Furthermore it also appears that these angles of arrival are not uniformly distributed in space. The angle of arrival distribution plays an important part in evaluating the antenna correlation function.

A new concept has been added to the existing diversity techniques which is called antenna pattern diversity using switched parasitic elements. First the far field patterns of two closely spaced dipoles are analytically derived. After that the same antenna system was put into a numerical tool and the far fields patterns are once again calculated. Comparing the analytical fields with the numerical fields shows us that the numerical tool is accurate and reliable. These far field patterns together with the angle of arrival distribution are substituted in the antenna correlation. Afterwards the load impedance of the parasitic elements was varied to obtain a low correlation coefficient. Unfortunately the return loss is worse at a low correlation coefficient. Therefore a (active) matching circuit is needed to improve the return loss.
A frequency sweep was done to investgate the frequency dependence of the correlation coefficient and the return loss. The correlation coefficient remains almost flat over the frequency bandwidth while the return loss remains worse. Apart from the worse return loss it was shown that this new concept worked quit well.

Finally the dual antenna system was built to compare the measured results with the simulated results. The radiation patterns are indirectly measured by means of measuring the antenna input impedance. Two measurement methods were discussed which are the unbalanced method and the balanced method. The latter gave the most accurate results apart from the calibration of the network analyzer. It was shown that a diversity gain of approximately 6 dB is achieved. This diversity gain is very close to the diversity gain obtained from selection diversity having an antenna interspacing of 0.25λ. We had to add critical observations to the number of 6 dB because the calibration of the network analyzer was not accurate and the number of points might be too small.

8.2 Recommendations

Future work which can be carried out to explore the AOA will be done, with the sophisticated 2D MUSIC algorithm to obtain the azimuth and elevation information directly. This can be done using data from the entire xy-table instead of a linear array. Bear in mind that the measurement time will increase, too. Consequently a snapshot cannot be considered a "shot" but takes a finite time duration. Moreover since the dimension of the xy-table is relatively large compared to the physical dimension of the handset the plane wave hypothesis might not be fulfilled across the xy-plane but might be fulfilled for the handset. So it is desirable for the measured set-up to be scaled to a smaller physical dimension. In doing so the spatial resolution should not become worse at these small aperture lengths.

Another option that can be taken is using different type of antennas instead of (whip) dipole antennas. E.g. microstrip antennas or planar inverted F antennas (PIFA's) of which the main feature is the extreme compactness. These different types should have a low correlation coefficient as well as a better return loss characteristic and should behave constant over the entire GSM bandwidth. For the far field pattern calculations a different numerical tool than NEC should be used.

The current measurement set-up should be modified in order to elaborate a more realistic environment such as a hardware electronic switcher and a dummy handheld. We must be aware of the fact that when measuring the radio channel (either a GSM system or the digital enhanced cordless telephone (DECT) system) may cause interference in the data due to the surrounding base stations.

In this graduation report two closely spaced dipole antennas were used. Another investigation item is the use of M antennas. In this case the mutual coupling between these antennas have to be considered which results in a $M \times M$ impedance matrix.

Furthermore an object close to the antenna system can be considered to emulate the "real world".

Chapter 9

Acknowledgements

I would like to thank Philips especially Philips research laboratory Eindhoven for giving me the opportunity to this graduation thesis. Furthermore I would like to express my deepest gratitude to Dr. M.H.A.J. Herben and Ir. L. Leyten who have always been available, interested and willing to help me during the course of the graduation thesis. Also many thanks to Ir. Y.L.C. de Jong, Dr. W.M.C. Dolmans, A. Kok and J.J.W. Siemons for their support and fruitful discussions.

Finally, I would like to thank all members and colleagues within the Integrated Transceivers Group and all my friends for their continuous support and their interest in my work.

P. Mattheijssen
Eindhoven, June 2000

Bibliography

[1] Rappaport, T.§. "Wireless communications", Prentice Hall,Communications eng. & emerging tech. series, ISBN 0-13-375536-3,1996.

[2] van den Enden A. W. M. and N. A. M. Verhoeckx, "Digitale signalbewerking", Delta press B. V. ISBN 90-6674-722-6,1987.

[3] Collin, R. E. "Antennas and radiowave propagation", McGraw-Hill series in electrical engineering, ISBN 0-07-118086,1985.

[4] Kraus, J. D. "Antennas", McGraw-Hill series in electrical engineering, Second edition, ISBN 0-07-100482-3,1988.

[5] Wolfram, S. "Mathematica", Addison Wesley,Second edition, ISBN 0-201-51502-4,1993.

[6] Jake, W. C. "Microwave mobile communications", IEEE communications society, ISBN 0-7803-1069-1,1993.

[7] Burke,G. J. and Poggio,A. J. "Numerical Eletromagnetics Code (NEC)-Method of Moments",
Part I : Program description-Theory,
Part II : Program description-Code,
Part III : Users guide,
Livermore, California: Lawrence Livermore National Laboratory, Springfield, Va. :National Technical Information Service, U. S. Department of Commerce, UCID-18834,1981.

[8] Vaccaro, R. J. "SVD and signal processing", Elsevier science publishers B. V. ISBN 0-444-88896-9,1991.

[9] Marple, S. L. Jr. "Digital spectral analysis with applications", Prentice Hall, signal processing series ISBN 0-13-214149-3,1987.

[10] Bucchianico, A. Di. "Statistical compendium" Eindhoven University technology.

[11] Leersum, van B. J. A. M. "Analysis of the interaction between a dipole antenna and a large object using the Method of Moments and the Finite Difference Time Domain technique", Nat. Lab. Report Nr. NL-UR 012/95, Department: Integrated Transceivers,1995.

[12] Leersum, van B. J. A. M. "Measurements of the interaction between a dipole antenna and a large abject", Nat. Lab. Report Nr. NL-UR 019/95, Department: Integrated Transceivers,1995.

[13] Massey, P. J. "Current based antenna radiation computation and its application to pager antennas", Philips Research Laboratories Redhill, Report No. 3465, July 1999.

[14] Massey, P. J. "Diversity antennas for a PCMCIA WLAN card", Philips Research Laboratories Redhill, Report No. 3835, 4/1999.

[15] Leather, P. S. H. and Massey, P. J. "Antenna diversity form two closely spaced dipoles", Philips Research Laboratories Redhill, Report No. RP3492, 1996.

[16] Beek, van W. H. M. and Kerkhof, van de A. E. M. "Radiokanaal modellering en karakterisering",
Automatisering van een radiokanaal meetopstelling en bewerking van de meetdata,
Philips Research Laboratories Eindhoven, Technical Note 813/98 Department: Integrated Transceivers,1998.

[17] Harris,F. J. ,"On the use of windows for harmonic analysis with the discrete Fourier transform", IEEE proceedings VOL. 66, NO. 1,pp51-83, January 1978.

[18] Schmidt, R. O. ,"Multiple emitter location and signal parameter estimation", IEEE Trans. on A&P, VOL. AP-47, NO. 3,pp276-280, March 1986.

[19] Serebryakov,G. V. , "Direction-of-arrival estimation of correlated sources by adaptive beamforming", IEEE Trans. on signal processing, VOL. 43,NO. 11,pp2782-2787,November 1995.

[20] Roy, R. and Kailath, T. , "ESPRIT-Estimation of signal parameters via rotationally invariant arrays" IEEE Trans. Acoust. , Speech, Signal Processing, VOL. 37, pp984-995,July 1989.

[21] Douglas, M. G. Okoniewski, M. and Stuchly, M. A. ,A. , "Planar diversity antenna for handheld PCS devices", IEEE Trans. Veh. Technol. ,VOL.47,NO. 3,pp747-754,August 1998.

[22] Taga, T, " Analysis for mean effective gain of mobile antennas in land mobile radio environments", IEEE Trans. Veh. Technol. ,VOL. 39,NO.2 ,pp117-131,May 1990.

[23] Taga, T, "Analysis of correlation characteristics of antenna diversity in land mobile radio environments", Electronics and Communications in Japan, Part 1,VOL. 74,NO. 8,pp101-115,1991.

[24] Colburn, J. S. , Rahmat-Samii,Y. ,Jensen, M. A. and Pottie G. J. , "Evaluation of personal communications dual-antenna handset diversity performance", IEEE Trans. Veh. Technol. ,VOL. 47,NO. 3,pp737-746,August 1998.

[25] Dolmans, W. M. C. and Leyten, L. , "Performance study of an adaptive dual antenna handset for indoor communications", IEE Proc. Microw. Ant. Propag. ,VOL. 146,NO. 2,pp138-144, April 1999.

[26] Dolmans, W. M. C. , "Effect of indoor fading on the performance of an adaptive antenna system", ISBN 90-386-0587-0.

[27] Scott, N. L. , Leonard-Taylor, M. O. and Vaughan, R. G. , "Diversity gain from a single-port adaptive antenna using switched parasitic elements illustrated with a wire and monopole prototype", IEEE Trans. on A&P,VOL. 47,No. 6,pp1066-1070,June 1999.

[28] Preston S. L. ,Thiel, D. V. ,Lu,J. W. ,O'Keefe, S. G. and Bird, T. S. , "Electronic beam steering using switched parasitic patch elements", Electronics Letters,Vol. 33,No. 1,pp7-8,January 1997.

[29] Thiel,D. V. ,O'Keefe,S. G. and Lu,J. W. , "Electronic beam steering in wire and patch antenna systems using switched parasitic elements", IEEE Trans. on A&P Soc. Int. Sym. Dig. ,pp534-537,1996.

[30] Vaughan, R. G. , "Switched parasitic elements for antenna diversity", IEEE Trans. on A&P,VOL. 47,No. 2,pp399-405,February 1999.

[31] Vaughan,R.G. and Andersen, J. B. , "Antenna diversity in mobile communications", IEEE Trans. Veh. Technol. VOL. VT-36,No. 4,pp149-172,November 1987.

[32] Zhang, Y. ,Hirasawa,K. and Fujimoto, K. , "Opened parasitic elements nearby a driven dipole", IEEE Trans. on A&P,VOL. AP-34,No. 5,pp711-713,May 1986.

[33] Adams, A. T. and Warren, D. E. , "Dipole plus parasitic element", IEEE Trans. on A&P,VOL. 6,pp536-537,July 1971.

[34] Yamada,Y. ,Ebine,Y. and Tsunekawa,K. , "Base and mobile station antennas for land mobile radio systems", IEICE Transactions,VOL. E74,No. 6,pp1547-1555,June 1991.

[35] Yamada,Y. ,Kagoshima,K. and Tsunekawa,K. , "Diversity antennas for base and mobilestations in land mobile communication systems", IEICE Transactions,VOL. E74,No. 10,pp3202-3209,October 1991.

*****

Appendix A

Figures: MUSIC spectra

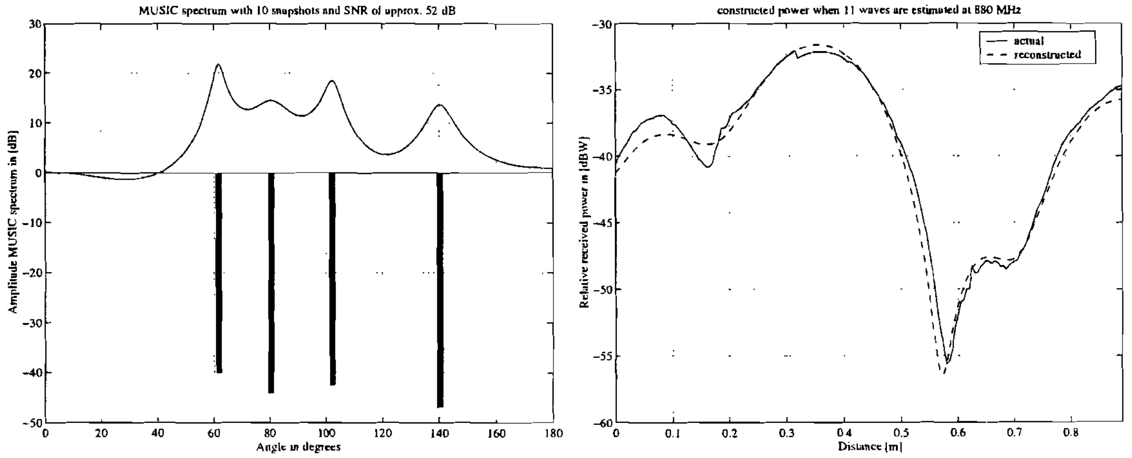

Figure A.1: *AOA in the x-direction at 880 MHz.*

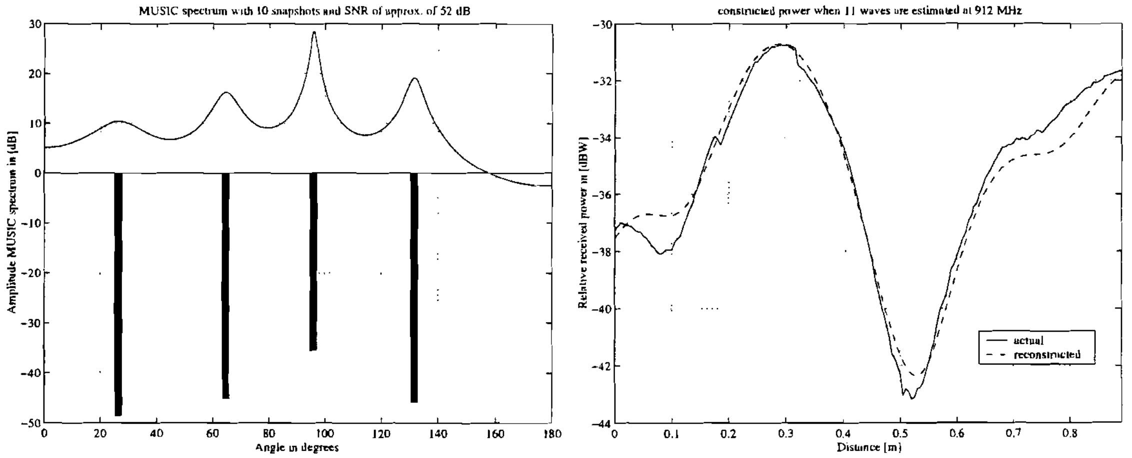

Figure A.2: *AOA in the x-direction at 912 MHz.*

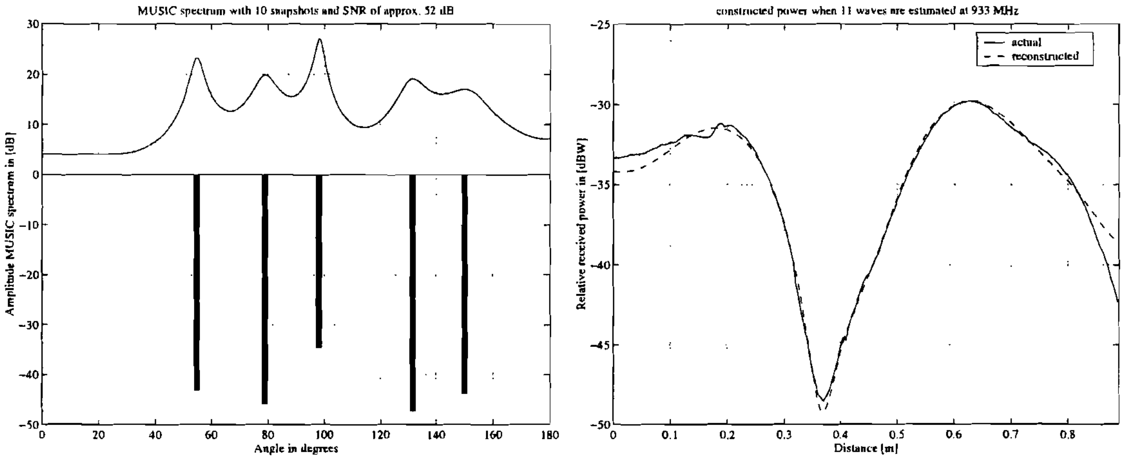

Figure A.3: *AOA in the x-direction at 933 MHz.*

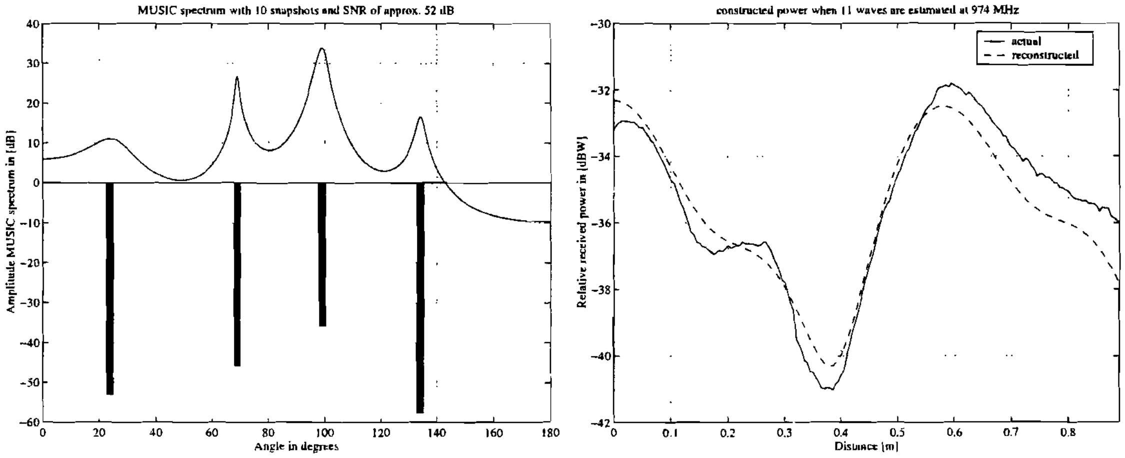

Figure A.4: *AOA in the x-direction at 975 MHz.*

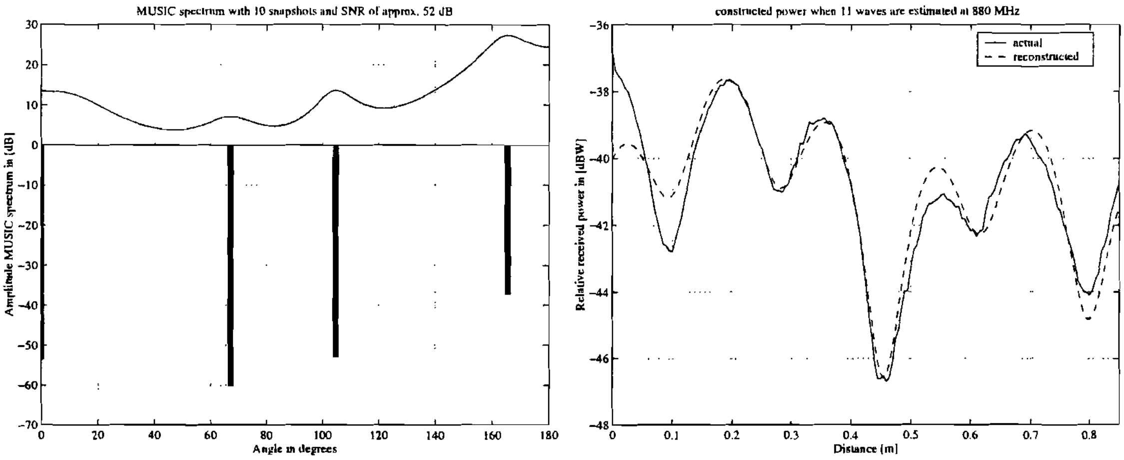

Figure A.5: *AOA in the y-direction at 880 MHz.*

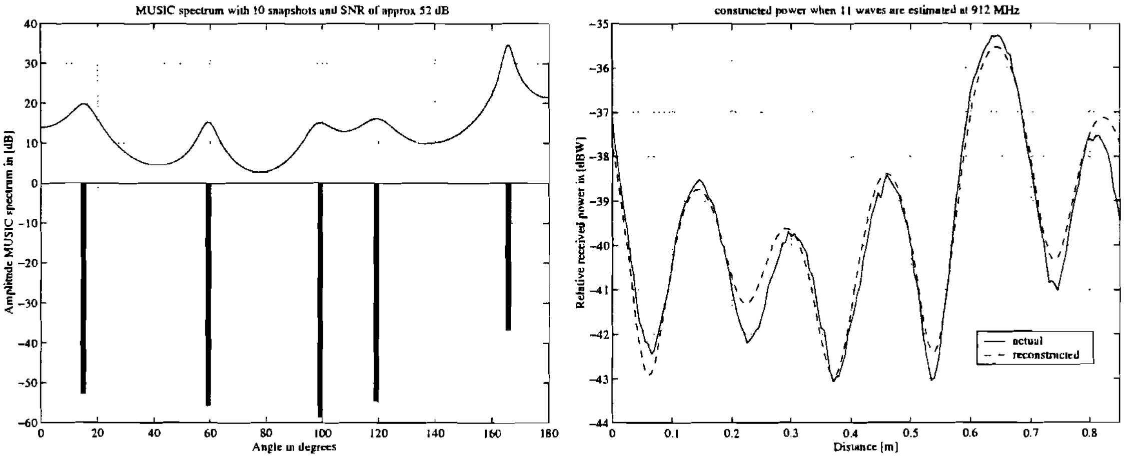

Figure A.6: *AOA in the y-direction at 913 MHz.*

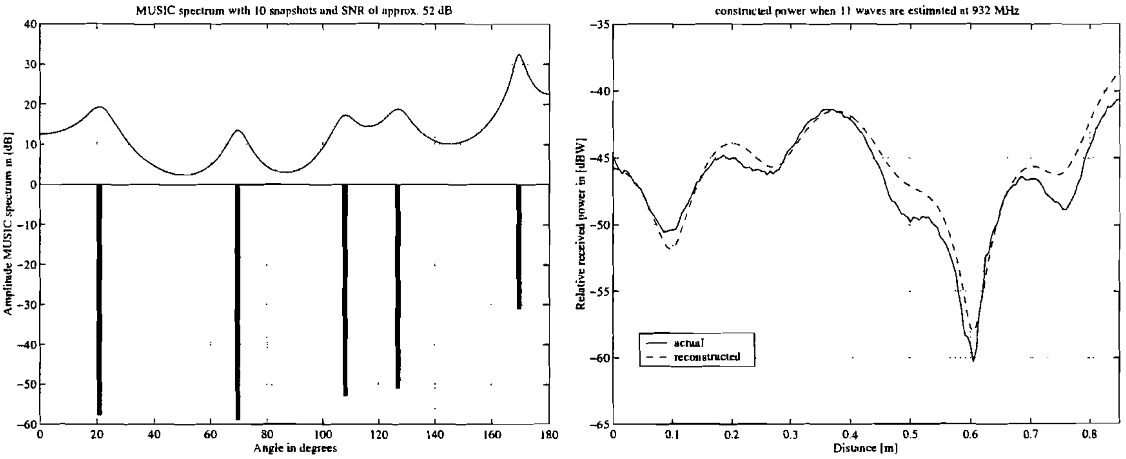

Figure A.7: *AOA in the y-direction at 934 MHz.*

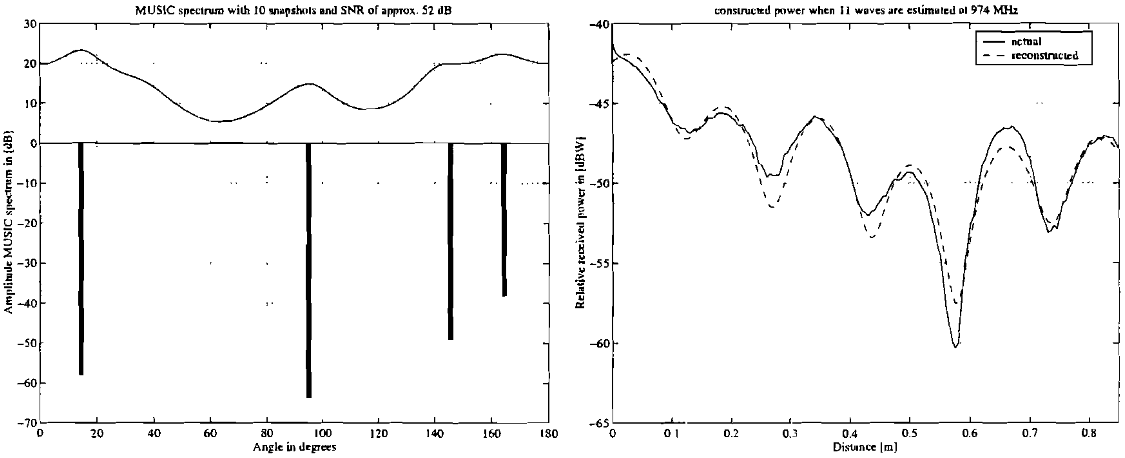

Figure A.8: *AOA in the y-direction at 978 MHz.*

Appendix B

Antenna correlation

Consider two continuous stochastic variables which are denoted by $\underline{E}_1(\theta,\phi)$ and $\underline{E}_2(\theta,\phi)$. We assume that these stochasts are stationary. This implies that $\mathrm{E}[\underline{E}_1] = \mathrm{E}[\underline{E}_2] = 0$. Where $\mathrm{E}[\bullet]$ stands for the ensamble average over all angles. We can define the correlation as follows [10]

$$\rho = \frac{\mathrm{cov}[\underline{E}_1(\theta,\phi), \underline{E}_2^*(\theta,\phi)]}{\sqrt{\mathrm{cov}[\underline{E}_1(\theta,\phi), \underline{E}_1^*(\theta,\phi)] \cdot \mathrm{cov}[\underline{E}_2(\theta,\phi), \underline{E}_2^*(\theta,\phi)]}} \tag{B.1}$$

where the mathematical function $\mathrm{cov}[\bullet]$ stands for the covariance operator. The correlation has been normalized. Since if two electrical fields E_1 and E_2 are identical the normalized correlation function should be equal to one. The covariance function can be expressed in terms of expectations. Equation (B.1) will become

$$\begin{aligned}\rho &= \frac{\mathrm{E}[(\underline{E}_1, \underline{E}_2^*)] - \mathrm{E}[\underline{E}_1]\mathrm{E}[\underline{E}_2^*]}{\sqrt{(\mathrm{E}[(\underline{E}_1, \underline{E}_1^*)] - \mathrm{E}[\underline{E}_1] \cdot \mathrm{E}[\underline{E}_1^*]) \cdot (\mathrm{E}[(\underline{E}_2, \underline{E}_2^*)] - \mathrm{E}[\underline{E}_2] \cdot \mathrm{E}[\underline{E}_2^*])}} \\ &= \frac{\mathrm{E}[(\underline{E}_1, \underline{E}_2^*)]}{\sqrt{\mathrm{E}[(\underline{E}_1, \underline{E}_1^*)] \cdot \mathrm{E}[(\underline{E}_2, \underline{E}_2^*)]}}\end{aligned} \tag{B.2}$$

where the independent variables θ, ϕ are omitted and $(\bullet, \bullet)$ stands for the dot product of two vectors. Now the correlation is expressed only in terms of expectations. Finally we have to elaborate the expectation functions. The expectation of two continue stochasts is defined as

$$\mathrm{E}[g(x,y)] = \int_{-\infty}^{\infty}\int_{-\infty}^{\infty} g(x,y) \cdot P_{x,y}(x,y)\ dxdy \tag{B.3}$$

where $g(x,y)$ is an arbitrary function of two variables and $P_{x,y}(x,y)$ is the probability density function (PDF). The integration interval is the entire space where the function $g(x,y)$ is defined. Applying this to equation (B.2) gives the following correlation expression:

$$\rho = \frac{\int_0^{2\pi}\int_0^{\pi}((\underline{E}_1, \underline{E}_2^*))P_{\theta,\phi}\ \sin(\theta)\ d\theta d\phi}{\sqrt{\int_0^{2\pi}\int_0^{\pi}((\underline{E}_1, \underline{E}_1^*))P_{\theta,\phi}\ \sin(\theta)\ d\theta d\phi \cdot \int_0^{2\pi}\int_0^{\pi}((\underline{E}_2, \underline{E}_2^*))P_{\theta,\phi}\ \sin(\theta)\ d\theta d\phi}} \tag{B.4}$$

The probability density function $P_{\theta,\phi}$ integrated over the entire space must be equal to one or expressed in a mathematical formula.

$$\int_0^{2\pi}\int_0^{\pi} P_{\theta,\phi}(\theta,\phi)\ \sin(\theta)\ d\theta d\phi = 1 \tag{B.5}$$

Elaborating the dot products in (B.4) give the correlation in terms of field components. To further reduce the lengthy expression the integration has been changed from θ and ϕ to the solid angle Ω.

$$\rho = \frac{\int \int_{\Omega} (E_{1\theta} E_{2\theta}^{*} + E_{1\phi} E_{2\phi}^{*}) P_{\theta,\phi} \, d\Omega}{\sqrt{\int \int_{\Omega} (E_{1\theta} E_{1\theta}^{*} + E_{1\phi} E_{1\phi}^{*}) P_{\theta,\phi} \, d\Omega \cdot \int \int_{\Omega} (E_{2\theta} E_{2\theta}^{*} + E_{2\phi} E_{2\phi}^{*}) P_{\theta,\phi} \, d\Omega}} \tag{B.6}$$

This quantity is a complex number. Therefore the antenna corelation is defined as

$$\begin{aligned} \rho_a &= |\rho| \\ &= \frac{\left| \int \int_{\Omega} (E_{1\theta} E_{2\theta}^{*} + E_{1\phi} E_{2\phi}^{*}) P_{\theta,\phi} \, d\Omega \right|}{\sqrt{\int \int_{\Omega} (E_{1\theta} E_{1\theta}^{*} + E_{1\phi} E_{1\phi}^{*}) P_{\theta,\phi} \, d\Omega \cdot \int \int_{\Omega} (E_{2\theta} E_{2\theta}^{*} + E_{2\phi} E_{2\phi}^{*}) P_{\theta,\phi} \, d\Omega}} \\ &= \frac{\left| \int \int_{\Omega} E_{1\theta} E_{2\theta}^{*} P_{\theta,\phi} + E_{1\phi} E_{2\phi}^{*} P_{\theta,\phi} \, d\Omega \right|}{\sqrt{\int \int_{\Omega} E_{1\theta} E_{1\theta}^{*} P_{\theta,\phi} + E_{1\phi} E_{1\phi}^{*} P_{\theta,\phi} \, d\Omega \cdot \int \int_{\Omega} (E_{2\theta} E_{2\theta}^{*} P_{\theta,\phi} + E_{2\phi} E_{2\phi}^{*} P_{\theta,\phi} \, d\Omega}} \end{aligned} \tag{B.7}$$

In this definition the radiation patterns are weighted all with the same AOA distribution functions. In practice the ϑ field components need not necessarily experience the same distribution as experienced by the φ field components. For instance, suppose a receiving antenna is positioned in an urban environment then it is more likelihood that the azimuth φ angles have been distributed more uniformly than the distribution for the elevation ϑ angles. Therefore the antenna correlation will be redefined to cope with component dependent AOA distributions.

$$\rho_a \doteq \frac{\left| \int \int_{\Omega} E_{1\theta} E_{2\theta}^{*} P_{\theta} + E_{1\phi} E_{2\phi}^{*} P_{\phi} \, d\Omega \right|}{\sqrt{\int \int_{\Omega} E_{1\theta} E_{1\theta}^{*} P_{\theta} + E_{1\phi} E_{1\phi}^{*} P_{\phi} \, d\Omega \cdot \int \int_{\Omega} (E_{2\theta} E_{2\theta}^{*} P_{\theta} + E_{2\phi} E_{2\phi}^{*} P_{\phi} \, d\Omega}} \tag{B.8}$$

Note that this antenna correlation is based on radiation patterns.

Appendix C

Figures: Correlation plots

Correlation plots where the steering impedance is varied as $Z = \jmath X$ where $X \in [-100, -50, 0, 50, 100, 10^6]$ and the variable impedance as $Z = R + \jmath X$ where $R \in [010, 20, \cdots, 200]$ and $X \in [-500, -460, \cdots, 500]$. On the left hand side the 3D correlation plot is drawn and on the right hand side an contour plot of the 3D correlation plot. Figure C shows the return loss as a function of Z_{var}.

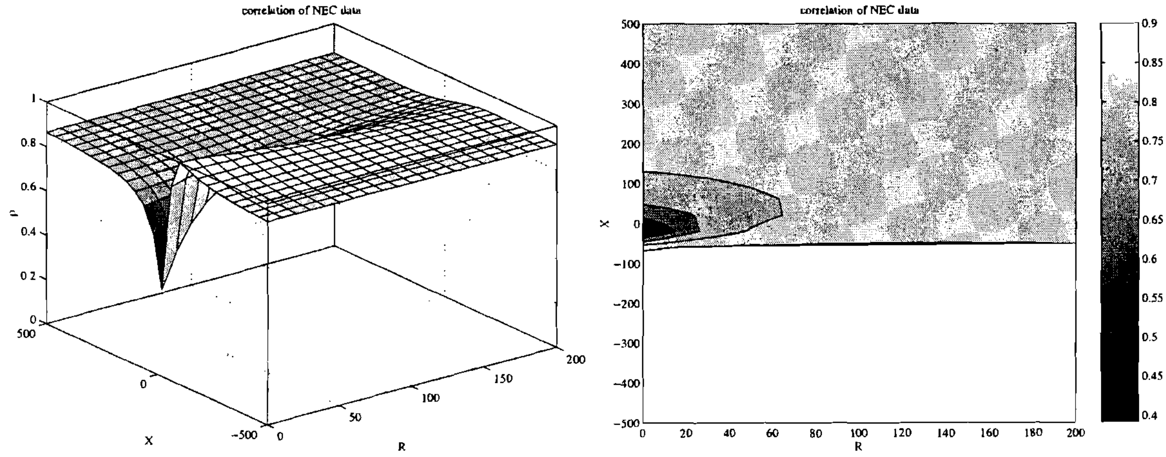

Figure C.1: *Correlation plot with steering impedance $Z = 0 - 100\jmath\ \Omega$.*

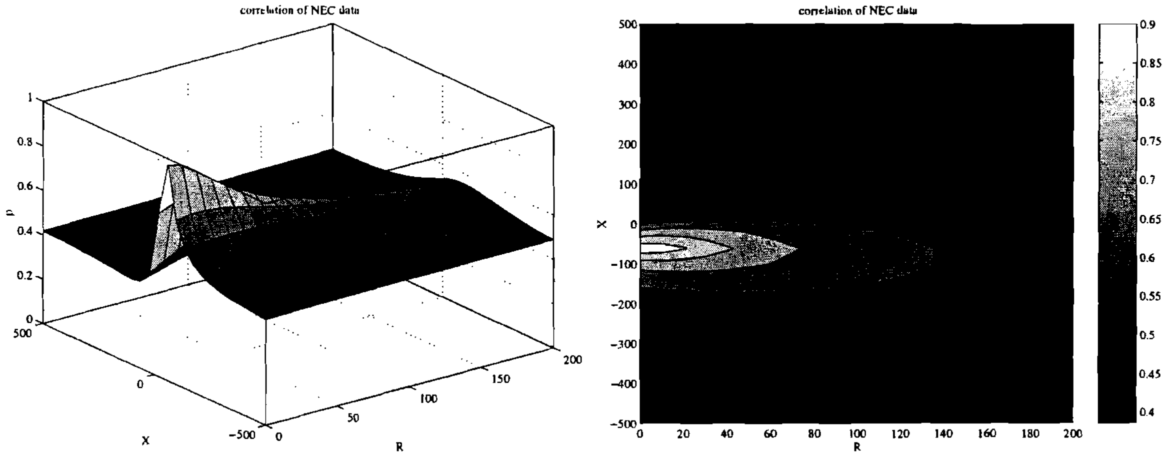

Figure C.2: *Correlation plot with steering impedance* $Z = 0 - 50j\ \Omega$.

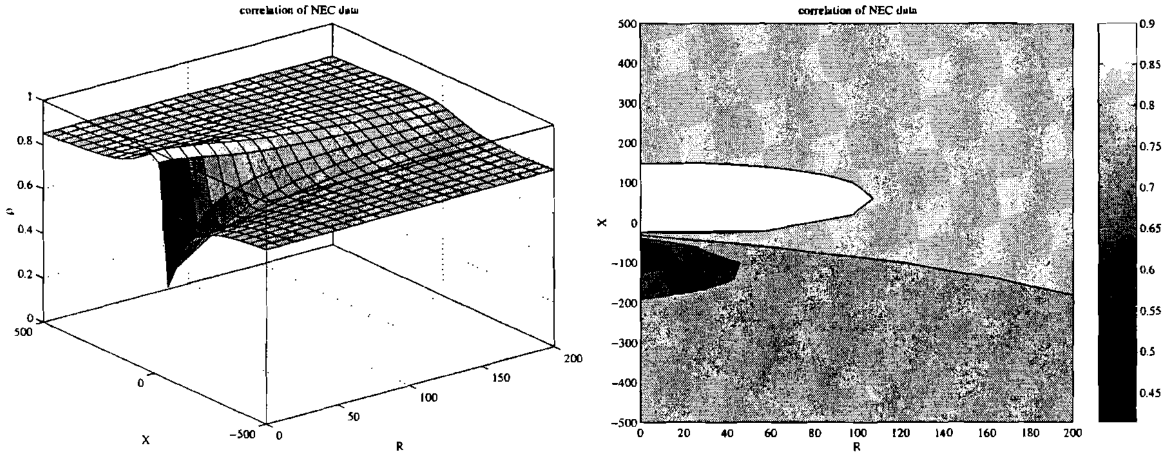

Figure C.3: *Correlation plot with steering impedance* $Z = 0\ \Omega$.

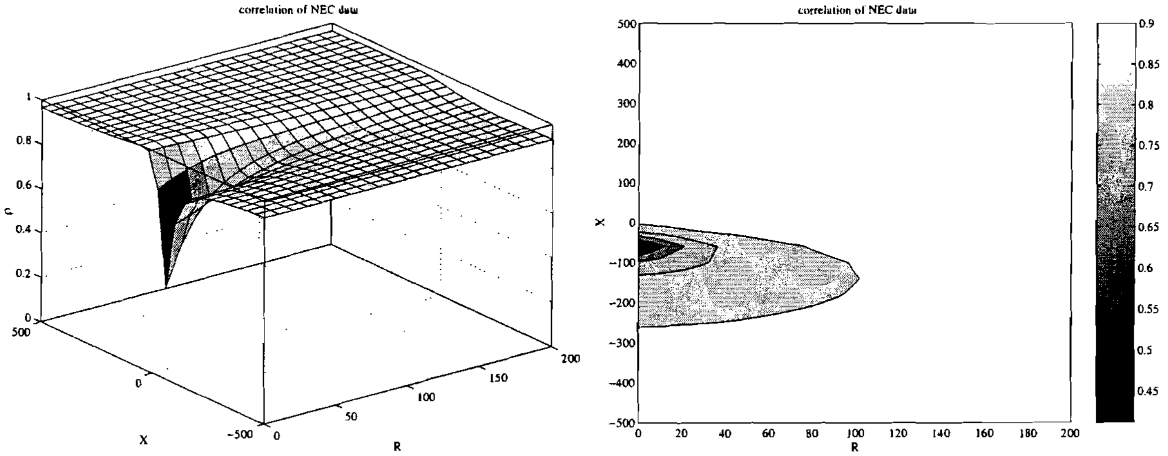

Figure C.4: *Correlation plot with steering impedance* $Z = 0 + 50j\ \Omega$.

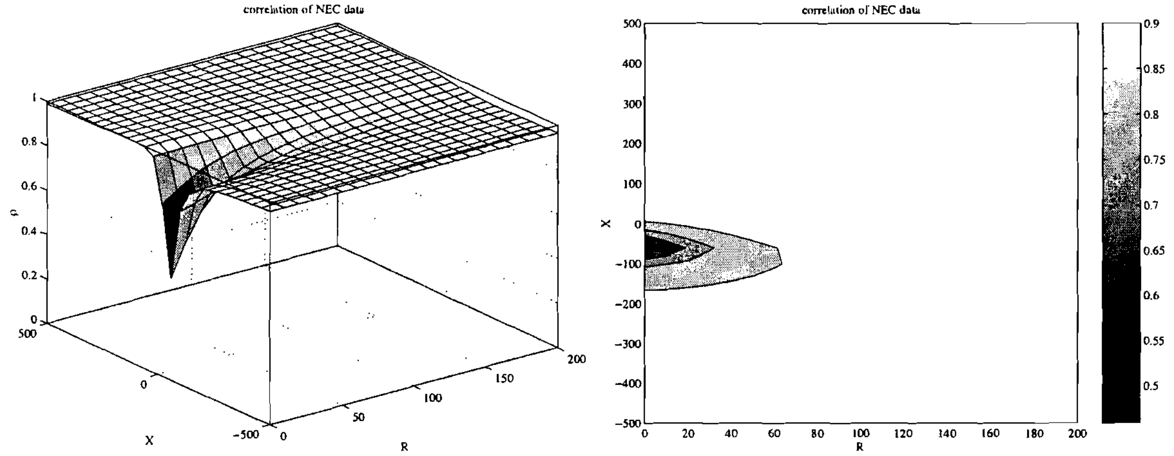

Figure C.5: *Correlation plot with steering impedance* $Z = 0 + 100j\ \Omega$.

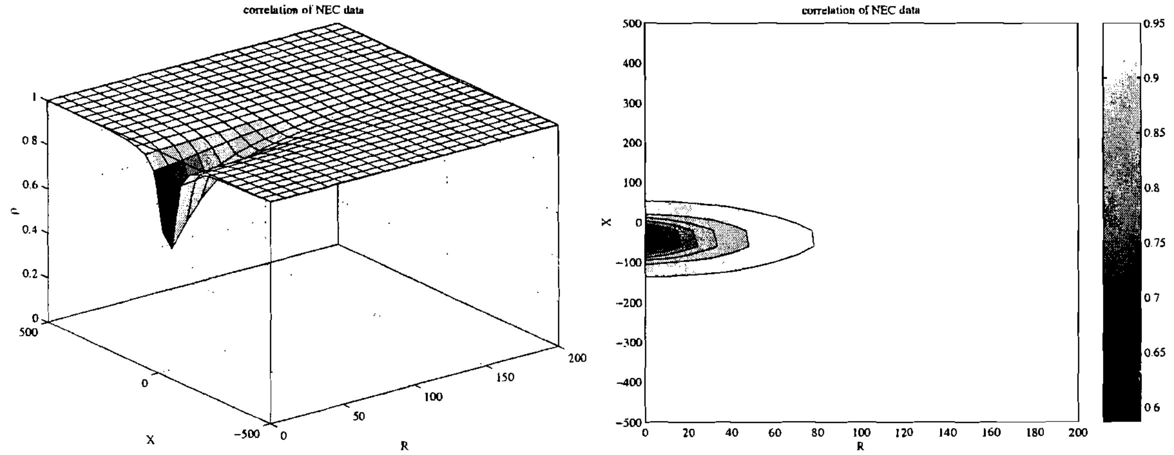

Figure C.6: *Correlation plot with steering impedance* $Z = 0 + 10^6 j\ \Omega$.

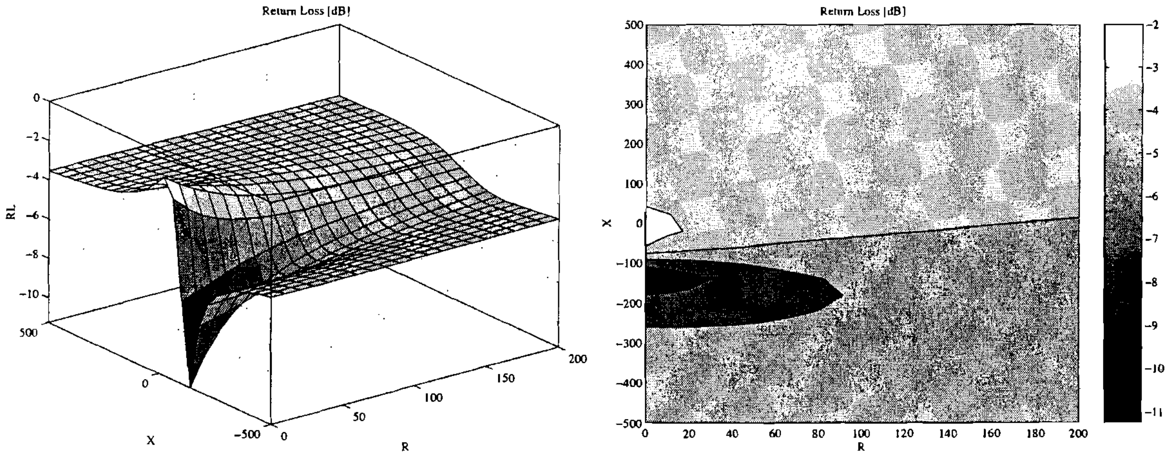

Figure C.7: *Return Loss (RL).*

Appendix D

Photos

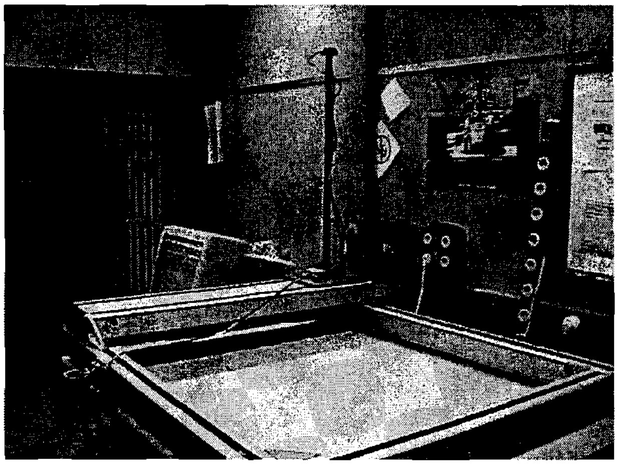

Figure D.1: *Measurement set-up following Figure 2.1.*

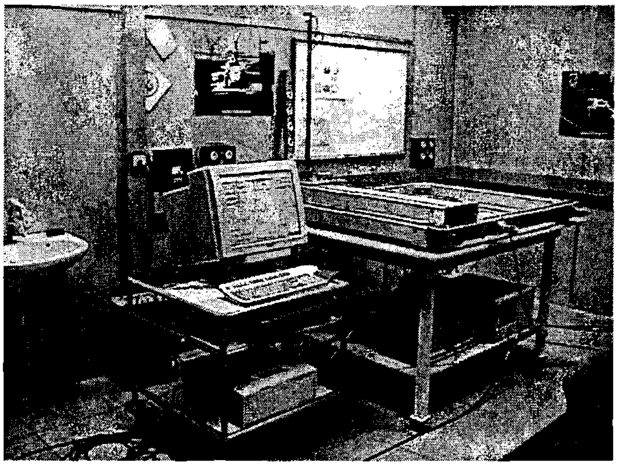

Figure D.2: *Measurement set-up from a different point of view.*

Figure D.3: *Interior of the restaurant of the building WAY.*

Figure D.4: *Interior of the restaurant of the building WAY from a different point of view.*

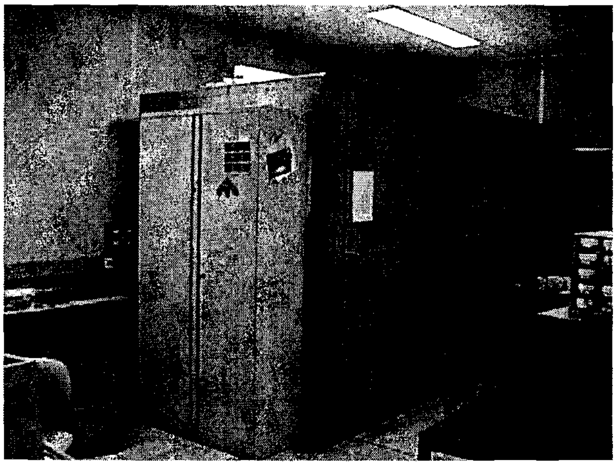

Figure D.5: *Environment of cage of Faraday (outside).*

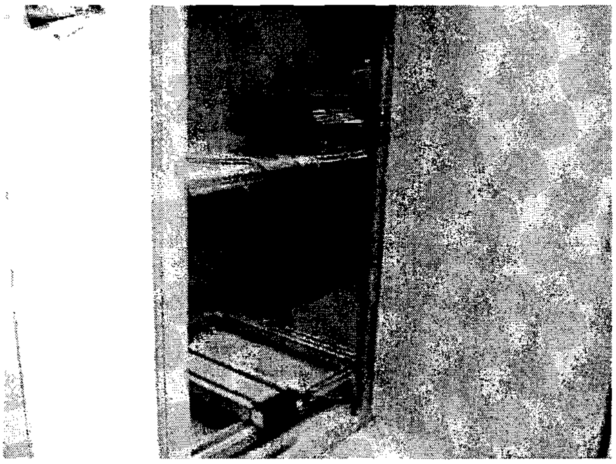

Figure D.6: *Environment of cage of Faraday (inside).*

Appendix E

Glossary

$\underline{a}(\cdot)$	Mode vector.
b	The voltage of the incident plane wave.
$\hat{b}$	Estimated voltage of the incident plane wave.
u_d	Spatial frequency in m^{-1} or in radm^{-1}.
$\Delta x, d$	Antenna interspacing in [m].
n	Received noise voltage at the antenna terminals.
p	Polarization loss.
r	Total received voltage including noise at the antenna terminals.
w	Number coherent sources.
D	Total number of incident plane waves.
$\underline{E}(\cdot)$	Electrical field.
E_n	Noise sub-space matrix.
F	Number of frequency components.
F_ℓ	A set channels in the lower frequency band (GSM900).
F_u	A set channels in the upper frequency band (GSM900).
G	Antenna gain function.
$\underline{H}(\cdot)$	Magnetic field.
J	Reverse permutation matrix.
L	Total aperture length of the array.
L_{bf}	Free-space basic transmission loss.
L_k	Total aperture length of the sub-array containing k elements.
M	Total number of antenna elements or dimension of the covariance matrix.
N	Total number of snapshots.
P	Signal covariance matrix.
P_{MUSIC}	MUSIC null spectrum.
P_r	Received power.
P_t	Transmitted power.
P_ϑ	Probability distribution function for the elevation angle.
P_φ	Probability distribution function for the azimuth angle.
R	Covariance matrix.
R_x	Receive side, at the x^{th} frequency component.
$\hat{R}$	Estimation of the covariance matrix.
$\tilde{R}$	An estimation of the estimated covariance matrix.
R_{fs}	Covariance matrix when forward smoothing is used.
$\hat{R}_{fs}$	Estimated covariance matrix when forward smoothing is used.

R_{fbs}	Covariance matrix when forward-backward smoothing is used.
$\hat{R}_{fbs}$	Estimated covariance matrix when forward-backward smoothing is used.
$S, S^{\perp}$	Defines a space made of a set independent vectors.
T_x	Transmit side, at the x^{th} frequency component.
α	Path loss exponent.
β	Wave number.
γ	Eigen value of the covariance matrix.
θ	Elevation angle with respect to the array axis.
λ	Wavelength in [m].
ν	Signal-to-noise ratio.
τ	τ^{th} snapshot and must lie between $[0, N]$.
ϕ	Azimuth angle with respect to the array axis.
Γ	Reflection coefficient.